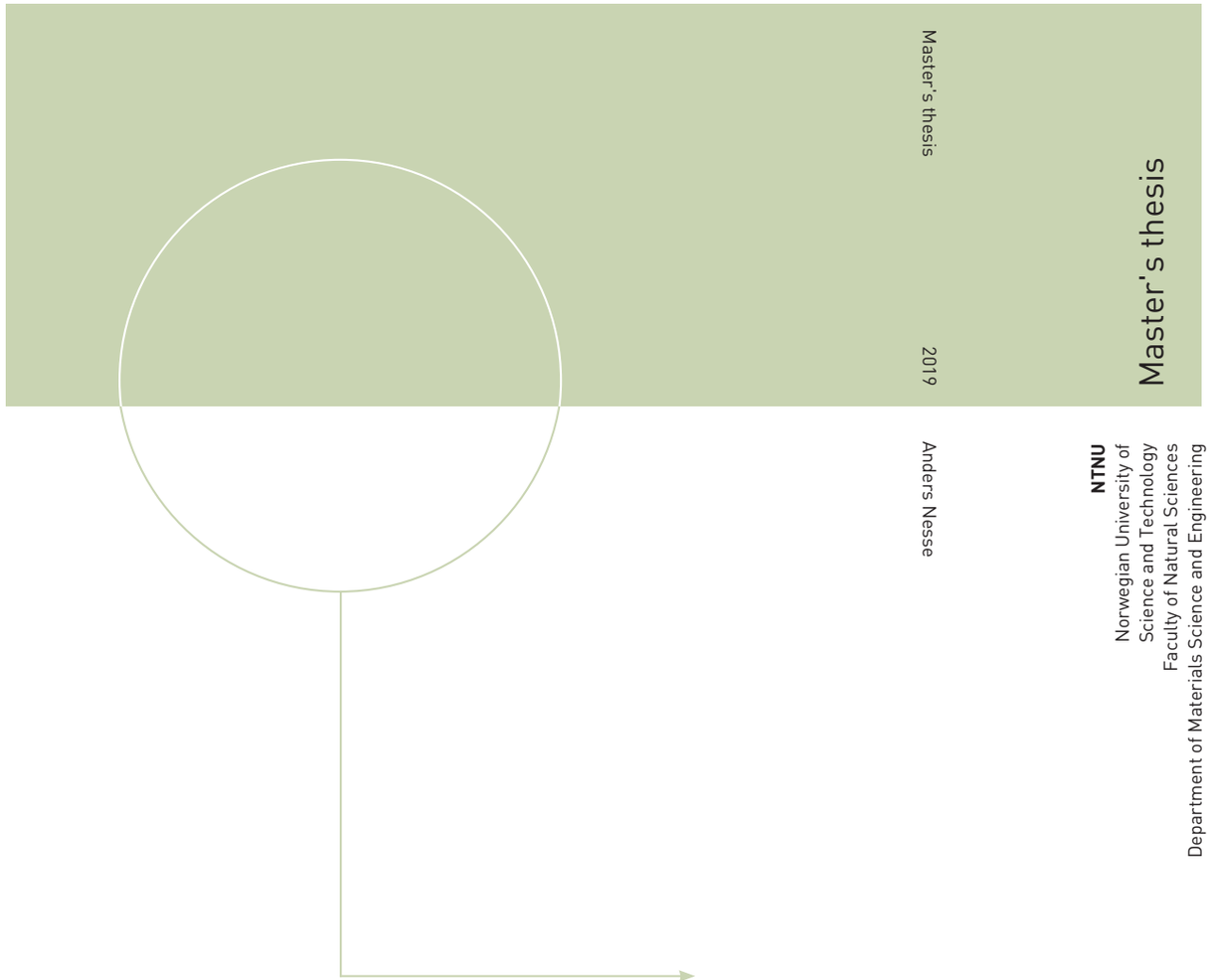

Master's thesis

2019

Anders Nesse

NTNU
Norwegian University of
Science and Technology
Faculty of Natural Sciences
Department of Materials Science and Engineering

Anders Nesse

Computational Alloy Design of AA6xxx Extrusions

June 2019

NTNU
Norwegian University of
Science and Technology

NTNU
Norwegian University of
Science and Technology

NTNU

Norwegian University of
Science and Technology

Computational Alloy Design of AA6xxx Extrusions

Anders Nesse

Industrial Chemistry and Biotechnology
Submission date: June 2019
Supervisor: Trond Furu
Co-supervisor: Ole Runar Myhr
Knut Marthinsen

Norwegian University of Science and Technology
Department of Materials Science and Engineering

Abstract

In this thesis, a series of computer models were utilized as a means to simulate the through process of aluminium during extrusion and subsequent artificial ageing. The objective is to optimize the mechanical properties while maintaining a fibrous microstructure. Different chemical composition within the AA6082 series were trialed, as well as different homogenization temperature, holding time, billet preheat temperature and extrusion ram speed.

Two parallels of four unique alloys with varying concentration of iron and chromium were cast, and the parallels were homogenized differently. The homogenized billets were then extruded with a flat rail profile at two different speeds, and with varying cooling rates. The alloys were examined for recrystallization, tearing, and dispersoids. Samples were artificially aged and tested for hardness throughout the ageing process. Electrical conductivity was measured.

A parameter study of the alloys was conducted in PRO^{3TM}, meaning that the experimental alloys were simulated in order to identify thresholds of recrystallization and tearing. These results have been compared to the experimental results.

The experiments yielded a wide selection of different microstructures, ranging from completely fibrous, to partly recrystallized, to fully recrystallized with small grains and fully recrystallized with large grains. It was found that chromium can help prevent recrystallization, and that slow cooling after extrusion promotes recrystallization. Results suggest that iron may have some favorable interaction with chromium in regards to dispersoid-forming, especially for longer homogenization times.

A wide range of number densities of dispersoids were measured, however these alloys were particularly difficult to examine accurately, as chromium containing dispersoids are darker and more difficult to separate from the aluminium matrix. These results should be judged critically.

The precipitation hardening resulted in very little to no difference in hardness when comparing as-extruded material and artificially aged material at regular intervals for up to 12 hours of artificial ageing at 180 °C. The reason as to why is not known.

Measurements showed that the longer homogenization treatment B, at 555 °C for 6 hours displayed a higher electrical conductivity than the shorter homogenization treatment A, at 585 °C for 1 hour.

Lastly, the thesis emphasized on the importance of digitalization in industry, and the use of partly or fully digital solutions for problems such as computational alloy design, process optimization, cost and environmental calculations. One key remark is that the PRO^{3TM} software can only be as good as the underlying models. It is therefore important that these models give an accurate description of the real work, while not being too computationally demanding.

Sammendrag

I denne oppgaven har en rekke beregningsmodeller blitt brukt for å simulere hele prosessen for ekstrudert aluminium og senere utherding. Den proprietære programvaren PRO^{3TM} knytter sammen flere modeller. I denne oppgaven er målet å optimere aluminiums mekaniske egenskaper imens en fibrig mikrostruktur blir ivaretatt. Forskjellig kjemiske sammensetning innenfor AA6082 legeringen har vært utprøvd, så vel som forskjellig homogeinseringstemperatur, holdetid, forvarmingstemperatur og ekstruderingshastighet. Programvaren ble brukt til å identifisere terskler hvor legeringen ville rekrystallisere eller riv vil forekomme.

To paralleller bestående av fire forskjellige legeringer med ulik konsentrasjon av jern og krom ble støpt. Parallellene ble homogenisert på to ulike måter, for så å bli ekstrudert med en flat skinneprofil ved. Legeringene ble deretter undersøkt for rekrystallisering, riv, og dispersoider. Prøvene ble utherdet og testet for hardhet under utherdingsprosessen. Elektrisk ledningsevne ble også målt.

En parameterstudie ble gjennomført i PRO^{3TM}, som betyr at de eksperimentelle legeringene ble modellert for å anslå terskler hvor rekrystallisering og riv vil forekomme. Disse resultatene har blitt sammenlignet med de eksperimentelle resultatene.

Eksperimentene gav et bredt spekter av forskjellige rekrystalliserte strukturer, Fra fullstendig fibrig, til delvis rekrystallisert, fullstendig rekrystallisert med små korn og fullstendig rekrystallisert med store korn. Effekten av homogenisering, kjemisk sammensetning og ekstruderingsparametre ble dokumentert.

En stor variasjon i antallstetthet av dispersoider ble observert, disse legeringene er imidlertid svært vanskelig å analysere nøyaktig med hensyn til dispersoider, ettersom kromholdige dispersoider er svært mørke og utfordrende å skille fra matriks i SEM.

Uthdering viste lite til ingen forskjell i hardhet mellom ekstrudert materiale og utherding ved regelmessige intervaller i opp til 12 timer ved en temperatur på 180 °C.

Det ble målt at den lengre homogeniseringsbehandlingen B, ved 555 °C i 6 timer gir høyere elektrisk ledningsevne enn den kortere homogeniseringsbehandlingen A, ved 585 °C i 1 time.

Avslutningsvis har oppgaven lagt vekt på viktigheten av digitalisering i industrien, og bruken av delvis eller fullstendig digitale løsninger for utfordringer slik som beregningsbasert legeringsdesign, prosessoptimering, kostnads og miljøberegninger. En sentral konklusjon er at rammeverket PRO^{3TM} bare kan være så god som de enkelte modellene. Det er derfor viktig at disse modellene gir en nøyaktig beskrivelse av virkeligheten, uten å gå på bekostning av beregningsintensiteten.

Preface

This Master's thesis has been a part of a collaboration between the Norwegian University of Science and Technology (NTNU), Norsk Hydro and SINTEF. It builds on a specialization project conducted during the fall of 2018 [1]. It has been facilitated by the Department of Materials Science and Technology during the 10^{th} and final semester of a five year Master's degree program in Industrial Chemistry and Biotechnology, with specialization in Materials Chemistry and Energy Technology. The thesis has been written during the spring of 2019. Some parts of the introduction, theoretical description, modelling procedure and data set is pulled directly from the foregoing project.

The study has been a part of a larger project within Norsk Hydro, in collaboration with Hydro Extruded Solutions (formerly SAPA) as well as SINTEF Manufacturing and NTNU, which aims to create a digital simulation software to predict and optimize the mechanical and structural properties of extruded aluminium through variations in chemical composition and thermomechanical treatment. This pilot project considers the AA6082 family of aluminium alloys with emphasis on its application in large constructions. The 6082-alloys are lighter than their steel counterparts, they have a high yield strength compared to other aluminium alloys, and exhibit excellent corrosion resistance and high recyclability. Components made from this alloy are typically formed by the process of extrusion. This type of alloy is used mainly as structural components in trusses and bridges, and in the automotive industry.

The main objective of this thesis is to map the accuracy of the computational simulations on which the design of the alloys were based. Four different alloys where cast and homogenized in two different ways, such as to produce eight unique samples. These samples were extruded at varying speeds, and were subjected to different cooling rates. Ideally, these experiments would yield a collection of different microstructures and failure mechanism patterns which would demonstrate the thresholds of each alloy.

Trondheim, June 11, 2019

Anders Nesse

Acknowledgements

This thesis was written under the guidance of many individuals at different institutions, without whom it would not be possible to facilitate and execute the work tied to this study.

First and foremost, supervisor Trond Furu[1] and this colleagues at Norsk Hydro must be thanked for providing me with this project, and for providing the necessary tools and network to conduct the study. He has shown an extensive intuition and knowledge of aluminium alloys, which in turn has been used to shape this project. Also a part of the Hydro team, co-supervisor Ole Runar Myhr[1] provided me with insightful knowledge of the underlying metallurgical phenomena and the computational models with great enthusiasm throughout the project.

Furthermore, Rune Østhus[2] and his tireless work and trust has been an invaluable resource in this project. Together with his guidance, the general structure of the report was formed, and the essential results were identified. He has also been very hospitable during my stay at SINTEF Manufacturing in Raufoss, where computation modelling results were discussed, and some experimental work was conducted.

I would also like to thank professor Knut Mathinsen[3] for introducing me to materials modelling during my 3^{rd} year, and for co-supervising this project. With his help, the model descriptions and general quality of the report has been elevated significantly.

Lastly, my gratitude is extended to the following: Dr. Kai Zhang and Dr. Freddy Leijon at Hydro Extruded Solutions for for collaborating with us on this project; Engineers Andreas Hjorth[3] and Berit Vinje[3] Kramer for supervising the experimental work and for the training in proper and safe use of laboratory equipment; Senior engineer Yinga Yu[3] for training and guidance on the SEM; PhD candidate Håkon Wiik Ånes[3] for general guidance in the metallographic lab, as well as providing me with the software for SEM image analysis; John Rasmus Leinum[1] for doing an independent dispersoid analysis in SEM. Regine Aagård, whose Master's thesis from 2015 provided me with a basis for my own thesis; and Helene Langeng for organizing the extrusion experiments.

[1] Norsk Hydro, Sunndalsøra
[2] SINTEF Manufacturing, Raufoss
[3] Norwegian University of Science and Technology (NTNU), Trondheim

Table of Contents

List of Tables

List of Figures

Abbreviations

ν_{ram}	=	Extrusion ram speed
β	=	Equilibrium phase (Mg_2Si)
β'	=	Hardening precipitate (semi-coherent needles/bonds)
β"	=	Hardening precipitate (semi-coherent needles)
σ_y	=	Yield strength
σ_i	=	Intrinsic strength of pure aluminium
σ_{ss}	=	Contribution from solid solution to the yield strength
σ_u	=	Ultimate tensile strength
σ_P	=	Contribution from precipitates and dispersoids to the yield strength
σ_R	=	Contribution from non-shearable particles to the solid solution hardening
P_D	=	Recrystallization driving force
P_Z	=	Zener drag
T6x	=	Artificial under-aged temper
T6	=	Artificial peak-aged temper
T7	=	Artificial over-aged temper
ML	=	Machine Learning
AI	=	Artificial Intelligence
IoT	=	Internet of Things
DOE	=	Design of Experiment
wt %	=	Weight percent
LCr	=	Low chromium content alloy
HCr	=	High chromium content alloy
LFe	=	Low iron content alloy
HFe	=	High iron content alloy
(Hom.) A	=	Homogenized at 585 °C for 1 hour
(Hom.) B	=	Homogenized at 555 °C for 6 hours
Alloy 1	=	Low Cr / Low Fe
Alloy 2	=	High Cr / Low Fe
Alloy 3	=	Low Cr / High Fe
Alloy 4	=	High Cr / High Fe
SEM	=	Scanning Electron Microscope
TEM	=	Transmission Electron Microscope

Chapter 1

Introduction

The new era of digitalization is pushing both the industry and tech sector to evolve. Introducing concepts like big data, AI (artificial intelligence), cloud computing and digital twins can enable industries to create more autonomous production lines, and defines the next industrial revolution. Interconnected devices and sensors can communicate with cloud computers to self-regulate, self-optimize and self-configure in a way which eliminates the need for human interference in order to increase productivity, reduce downtime and help human workers perform increasingly complex tasks. Such systems may however be vulnerable to cybersecurity threats.

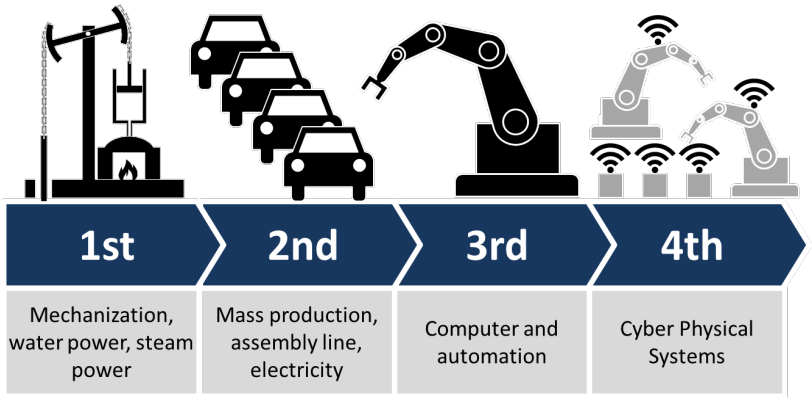

Figure 1.1: Graphic illustration of the four industrial revolutions [6].

Industry 4.0 and the digital revolution may provide game-changing advancements to the fields of natural sciences and engineering. The advancements of hardware, algorithms and increasingly intricate models describing the behaviors and properties of materials will enable the application of advanced computational methodology. Recent progress in scientific research has opened opportunities for computational alloy design, accurate prediction

of microstrucutral properties, deep learning methods related to manufacturing, and the use of neural networks applied to fields such as weld processing [7].

The Norwegian aluminium industry is under constant pressure to improve their products, efficiency and methodology to stay competitive with manufacturers from countries with cheap labor. R&D is both costly and time consuming, due to its complex nature. Recent studies indicates that the benefits of the digital revolution may reduce both cost and time of developing new solutions to the industry. However, new findings are still needed to enable significant advancements. Machine learning applied to the materials manufacturing industry is one such example. These findings depend on the fusion of expertise from a wide range of technical fields such as materials science, industrial, mechanical and civil engineering, as well as computer science fields such as big data, artificial intelligence, machine learning, data mining and high-performance computing. Utilizing these concepts to the full extent is a key part of the transition into Industry 4.0.

During the last 25 years, a collaboration between Norsk Hydro, the Norwegian University of Science and Technology (NTNU) and SINTEF has resulted in a series of numerical models, each describing a particular process in the through process of extruded aluminium. The models describe phenomena ranging from the uneven distribution of alloying elements during casting, to the diffusion of elements and formation of dispersoids during thermal heat treatment, the stretching and deformation of grains during extrusion, and the nano-scale precipitates which form during artificial ageing. These computational models have been coupled together in a workflow to simulate the through process of extruded aluminium, and artificial intelligence use the simulations to optimize selected properties, e.g. strength or corrosion resistance, while constraining other properties such as recrystallization or probability of tearing. The software can also be used to minimize production cost and environmental impact. This approach of digital R&D may revolutionize the process of aluminium product design. Experiments can be conducted faster, at a lower cost and with a lower risk for workplace injury.

The vast abundance of aluminium resources, it's ease of recyclability and corrosion resistance argues that its use should be expanded. By using the software discussed in this thesis, it is argued that the current aluminium products can be improved, while new products can be found where existing products are made from more polluting, scarce or non-renewable resources.

In this thesis, the computational models made by Norsk Hydro, SINTEF and NTNU, together with commercially available software, will be used to design a high strength AA6082 alloy. Experimental tests will challenge the accuracy of the models, and if needed, the models will be modified depending on the results. Furthermore, utilizing this approach for product design may help establish the use of these methodologies for future pilot projects.

Chapter 2

Theoretical Background

2.1 Digitalization

Historically, the field of engineering has been mostly a profession based on trial and error, where experiments were conducted systematically and measurements were made until an acceptable solution was reached. This approach of trial and error is both time and cost intensive, and finding an optimal solution is not guaranteed. The approach of digitalization takes the guesswork out of the equation [9].

The integration of concepts from the field of computer science such as machine learning (ML), neural networks, internet of things (IoT), digital twins, artificial intelligence (AI), aided by quick and dependable wireless data transfer creates many opportunities for optimization along a product's value chain [9]. Industries should exploit these innovations to create more efficient, autonomous and safe processes to produce improved products at a lower cost and with lower environmental impact. Tasks with a predefined, or deterministic outcomes, such as extracting key information from extensive documentation or perform a certain order of calculations, can be done by machines at incredible speed, whilst minimizing the error rate. Additionally, this frees human labor to focus on more diverse tasks, where general intelligence is needed.

Machine learning is the process where an algorithm is teaching itself to be better at a very specific task based on the large data set of previous outcomes for the same task. This statistical approach to learning negates the necessity to understand the concept in depth, and treats the task as a black box. In essence connection between inputs and outputs are known, the reasoning is not. This way, an algorithm can learn to handle a task without being explicitly programmed to do so [11], which is a great advantage for complex tasks which do not have a well understood solution. The streaming service Netflix famously issued a prize reward of $1,000,000 for anyone who could make a recommendation algorithm which was at least 10 % more accurate than existing algorithms. The prize was eventually claimed by a team of ML developers [10].

Internet of Things are items and devices fitted with electronics, internet connectivity and sensors. They can be monitored or controlled remotely, and they can communicate

with other devices in real time over the internet [12]. IoT can enable Industry 4.0 by equipping devices with sensing, processing, identification, communication, networking and actuation capabilities, such as to create a cyber physical space (CPS). By applying industrial big data analytics on the large data sets generated from the IoT, predictive asset maintenance can be implemented and the data collected can be turned into actionable information [13]. The implementation of IoT is estimated to generate $12 trillion globally by 2030 [14].

Digital twin is a central concept in the digitalization process. A digital twin is, in principle, a perfect replica of a real asset or process in a digital environment. This asset can be as small as a suspension unit in a car, or as large as an entire tanker ship. The model can be mimic the asset in real-time using data from sensors [15]. These digital copies can be subjected to digital testing such as fatigue wear, to estimate the remaining life time of a component. This knowledge can in turn be used to plan ahead for maintenance and furthermore reduce the total downtime. To facilitate the use of digital twins, numerical models must exist such that accurate experiments can be conducted in a digital environment [16].

2.2 Aluminium

Aluminium is the most abundant metal in the Earth's crust, making up about 8.1 % of the total mass. It exists in nature only as compounds such as aluminium oxide (Al_2O_3) and potassium aluminium sulphate ($KAL(SO_4)_2 \cdot 12\ H_2O$) [18]. On a global average, about 15 kWh of energy per kilogram is required to produce metallic aluminium [19]. Pure aluminium however, can be recycled over and over again without loss of properties, and at great reduction of energy cost compared to the production from raw materials.

Aluminium is made industrially from refined bauxite, alumina (Al_2O_3), in an electrolytic cell through the Bayer and Hall-Heroult process. The liquid aluminium may be cast into their finished product, or as ingots, billets and sheets to be further processed into different products.

Aluminium alloys have many desirable properties. At just one third the density of steel, aluminium is lightweight, and it also has good electrical- and heat conductivity as well as corrosion resistance. With the right alloying elements and proper mechanical or thermal treatment, aluminium can also have high strength. Aluminium is therefore suitable for structural components in buildings and constructions such as bridges, as well as in automotive industry and in aeroplanes. Aluminium is also used in short life-cycle items such as foil and soda cans due to its isolating properties and excellent recyclability. Different alloying elements such as silicon (Si), magnesium (Mg), iron (Fe), zinc (Zn) and copper (Cu) are typically found in different series of aluminium [26]. Elements are typically added to improve upon the properties of the metal, but other elements, such as iron and zinc are contaminants which are there just because they're hard to separate from the aluminium. Figure 2.1 illustrates the proposed life cycle of aluminium.

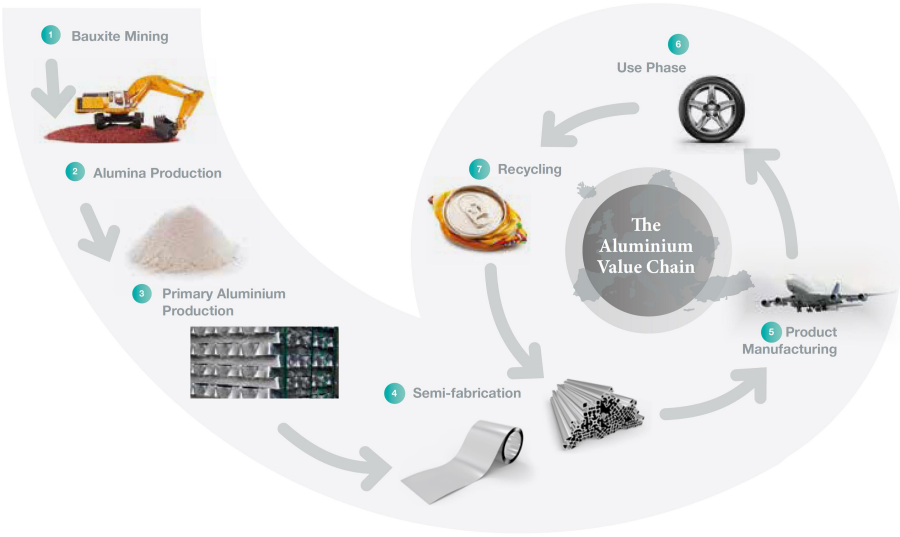

Figure 2.1: Proposed life cycle of aluminium [20].

2.2.1 Cast and Wrought Alloys

Cast alloys are aluminium alloys which can be cast into their finished products and are identified by a three digit number (1XX, 2XX, etc.). These alloys, especially the 300-series (Al-Si-Cu or Al-Si-Mg) are commonly used in the automotive industry. Car parts such as intake manifolds, engine blocks, cylinder heads, wheels and suspension arms are examples of consumer products made from cast alloys [21]. These alloys have a range of properties which give them good castability. This includes the high fluidity, low melting point, short casting cycles, low tendency for hot cracking, good as-cast surface appearance and chemical stability [22].

Wrought alloys are aluminium alloys which have been subjected to mechanical processing such as rolling, extrusion or forging and retain their mechanical properties at temperatures as high as the 520 to 590 °C range [23; 24]. Wrought alloys are identified by a four digit number as opposed to three (1XXX, 2XXX, etc.) and are processed thermomechanically into semi-finished products. Wrought alloys are separated into two categories, non age-hardenable and age-hardenable alloys.

Non Age-Hardenable

Non age-hardenable alloys cannot be hardened by precipitation as no precipitating alloying elements exits in solid solution. Thus, they retain their mechanical properties over time as no precipitation of particles occur in the metal. The non age-hardenable alloys are the AlMn (3XXX) and AlMg (5XXX) series alloys. The strength of these alloys come are derived from work-hardening and alloying elements in solid solution.

Age-Hardenable

Age-hardenable alloys are alloys which experience change of mechanical properties over time due to the precipitation of particles. This process is however very slow at room temperature, which is why the aluminium is kept at elevated temperatures to initiate the precipitation of meta-stable phases which contribute to the strengthening of the alloy. This process is referred to as artificial ageing. The age-hardenable alloys are the AlCu (2XXX), AlMgSi (6XXX) and AlZn (7XXX).

2.3 AlMgSi Alloys

AlMgSi alloys (AA6XXX or 6000- series) belongs to the age-hardenable alloys and are predominant in extrusions, where an estimated 90 % of extruded aluminium is made from AlMgSi alloys [25]. Extrusion is a method of mass producing intricate geometries which can easily be formed into finished products. The alloys' good mechanical properties, corrosion resistance, response to extrusion and high formability makes it ideal for this purpose. Appearance and response to surface treatment is also desirable. The main effects of each alloying element can be found in Table 2.1.

Table 2.1: The effects of different alloying elements in AA6xxx [26].

Element	Main effect
Si	Higher strength
Fe	Reduce corrosion resistance, contamination
Cu	Higher strength
Mn	Inhibit recrystallization, grain refiner
Mg	Higher strength, increased oxide layer stability
Cr	Inhibit recrystallization, grain refiner
Ni	Higher strength, lower ductility
Zn	Contamination

The AA6082 alloy is one of the most prevalent alloys within the 6xxx series [27] due to its high strength. Its chemical makeup can be seen in Table 2.2.

Table 2.2: Chemical composition of aluminium AA6082 [28].

Element	Si	Fe	Cu	Mn	Mg	Cr	Ni	Zn
Composition [wt%]	0.7-1.3	0.5	0.1	0.4-1.0	0.6-1.2	0.25	-	0.2

2.4 Aluminium Processing

In this section, the typical industrial production cycle of extruded aluminium will be discussed. The mathematical descriptions of these processes are found in Section 2.6, as they relate to the computational modelling.

The cycle starts when liquid aluminium from electrolytic cells solidify during casting. Thermal treatment is common to dissolve and distribute alloying elements evenly throughout the billet. This process forms dispersoids and changes the presence of primary and secondary phases throughout the material.

Prior to extrusion, the billet is preheated to make the metal softer, and thus easier to deform. Extrusion is a process where a hydraulic press forces the aluminium through a die with desired dimensions and geometry to produce a desired profile. The high force and temperature exerted onto the aluminium creates a high driving force for alterations in the microstructure. Recrystallization in generally not desired, and is counteracted by the presence of dispersoids and water quenching after extrusion. Processes such as extrusion rely on high forces and temperatures and are referred to as thermomechanical processes.

After extrusion, the profile may be stretched, cut or formed to fit final product specifications, and afterwards subjected to elevated temperatures of around 185 ± 15 °C to induce the artificial ageing process which increases strength in age-hardenable aluminium alloys. Any surface treatment such as anodizing or painting occurs after ageing, before the final product is shipped to the customer [29]. A proposed production cycle of extruded aluminium can be seen in Figure 2.2.

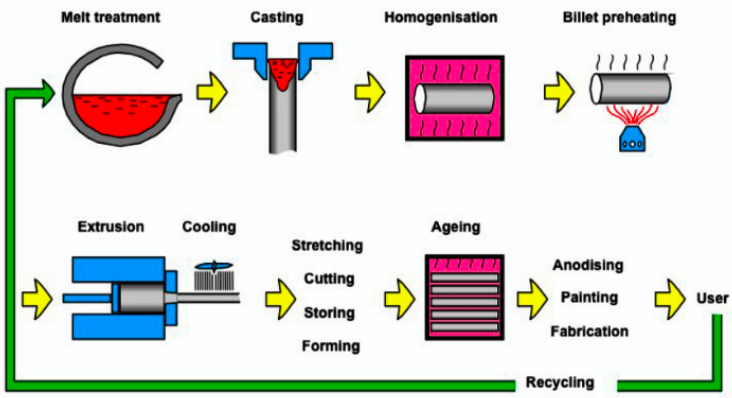

Figure 2.2: Proposed production cycle of extruded aluminium [29].

Figure 2.3 shows the time-temperature diagram of the proposed production cycle of extruded aluminium as seen in Figure 2.2.

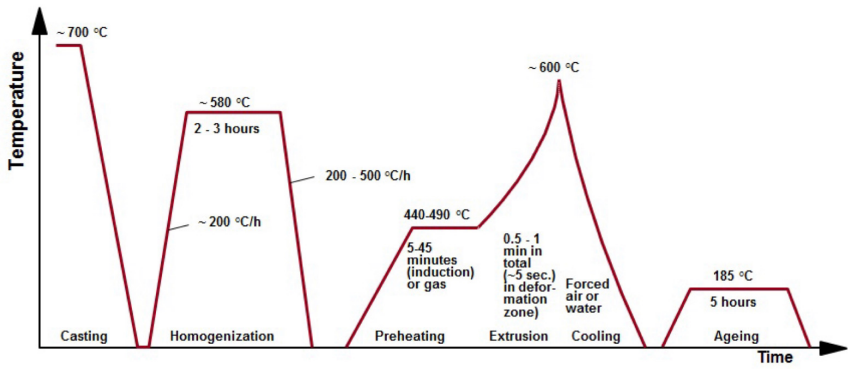

Figure 2.3: Time-temperature diagram throughout the proposed production cycle of extruded aluminium [25].

Casting

Wrought aluminium can be cast in several different ways. Sheets, ingots and billets are among the most common. Billets, which will be the basis of this thesis, can be cast vertically through a tube with intense external cooling (water quenching), which solidifies the surface, and causes the core to cool and solidify gradually. The diameter of the billet is dependent on the steel tubing, while the length is specified by the duration of the casting process before sawing the billet off. The rapid solidification of the billet will cause an uneven distribution of alloying elements within the billet. The properties of aluminium alloys are heavily dependent on the alloying elements, which is why a thermal process is required to remove undesirable phases such as β-AlFeSi and particles like Mg_2Si, while promoting non-detrimental phases such as α-AlFeSi and dispersoid particles.

Homogenization

The occurrence of phases and particles are controlled by the process of homogenization. As the name suggests, this thermal treatment aims to homogenize the aluminium, i.e. to equalize the uneven distribution of some alloying elements. During casting, iron bearing phases like β-AlFeSi form, and can deteriorate the mechanical properties of the metal. This phase should be eliminated or minimized [30]. During homogenization, this β-phase is transformed into α-AlFeSi, the desirable alternative out of the two [31]. Furthermore, AlMgSi alloys procure Mg_2Si primary and secondary particles during casting, both of which may cause local melting during the extrusion process, which in turn cause tearing of the profile [32]. These particles may also be dissolved during homogenization. Primary particles made from iron, silicon, magnesium, etc. may absorb important alloying elements, which removes them from solid solution [34]. This negates the positive effects of the alloying elements. Proper homogenization treatment can dissolve these particles as well.

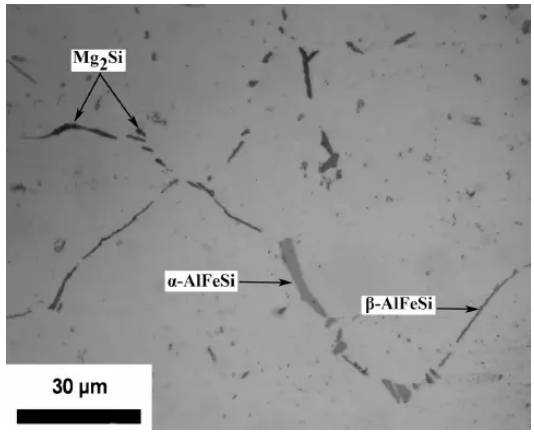

Figure 2.4: Mg_2Si particles and AlFeSi phases in AA6082. Seen in SEM [39].

Additions of manganese (Mn) has been shown to enhance the β- to α-AlFeSi transformation, as well as causing a more uniform Mg_2Si distribution [31]. The α- phase holds less silicon compared to the β- phase, and must be promoted, as silicon enhances the strength of the alloy. Manganese, zirconium (Zr) and chromium (Cr) also form so-called dispersoids. Small particles ranging from a few nano meters up to one μm [36]. Dispersoids form because these transition elements have low solubility in α-aluminium, and the particles can prevent or retard recrystallization and increase stability of the microstructure at high temperatures, as the elements have a low diffusivity and solubility in the metal [37]. Manganese dispersoids form an incoherent structural relationship with the FCC aluminium matrix as Al_6Mn. Dispersoid particles form during homogenization and may vary in shape, size and density depending on the conditions of the thermal treatment and concentrations of alloying elements. For instance, needle-like dispersoids are formed during rapid heating and are much more effective for grain refinement during recrystallization than fine spherical dispersoids, which form during slow heating [37]. Moreover,

dispersoids grow larger during longer thermal treatments, which in turn may decrease the number density [45]. This process is known as coarsening. Finding the balance between a high number of dispersoids to prevent or retard recrystallization, elements in solid solution to achieve a high strength alloy, dissolving Mg_2Si particles and transform β-AlFeSi phases are some objective of the homogenization process [34]. The key parameters during homogenization is the holding time and holding temperature, as well as both heating and cooling rate. A consensus of two hours minimum is accepted in the industry, however, larger billets may require longer holding times. As the process is diffusion controlled, longer holding times may be needed to remove micro-segregation [30].

Figure 2.5 shows a SEM image of an aluminum alloy where different grains are highlighted and dispersoids can be found at the interface between different grains. After thermomechanical processing, recrystallization is prevented by dispersoids as they reduce the available nucleation sites and inhibit growth through the phenomena known as Zener pinning [38].

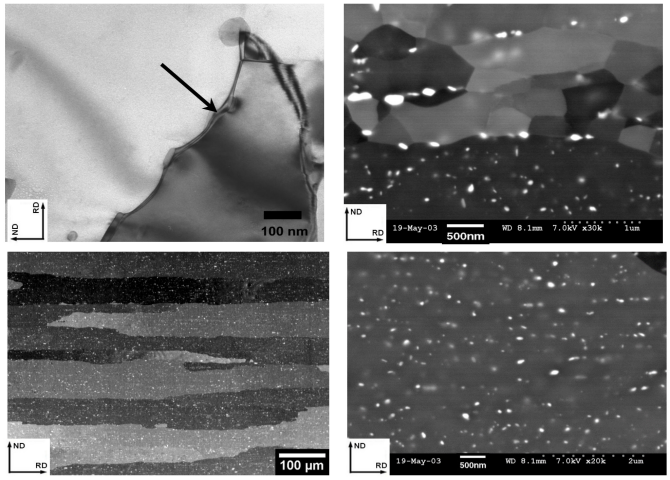

Figure 2.5: Dispersoids (white) in aluminium inhibit nucleation and growth of recrystallized grains [34].

Extrusion

During this thermomechanical process, the aluminium billet is formed into a profile with fixed cross-sectional shape. During extrusion, the material is only subjected to compressive and shear stresses, which allows it to be formed into complex cross-sections at industrial efficiency [33]. Prior to extrusion of aluminium, the billet is preheated to around 450-550 °C to soften the metal. A hydraulic press forces the solid aluminium billet through the die, and the extruded profile may be air cooled or quenched in water. The grain structure is fundamentally changed, as grains are stretched and pressed into a fiber-like structure, where the fibers run along the direction of extrusion. The cross-sectional area of the billet is reduced often by a factor of 15 or higher. This causes a large amount of stored energy in the deformed grains, which acts as a driving force for recrystallization (P_D). Grains at the surface of the billet will be exposed to higher strain rates, and as such, the surface of the profile is more likely to have a recrystallized layer, as indicted by the edges of the profile in Figure 2.6 (b). The aforementioned dispersoids is the cause for the counteracting force known as Zener drag (P_Z), through Zener pinning and by preventing nucleation. Whether or not the aluminium experiences recrystallization is dependent on the balance between P_D and P_Z. As will be described numerically later, Zener drag correlates positively with the volume fraction, and is inversely proportional to the mean radius of the dispersoids [58]. Many small dispersoids makes the inter-particle spacing smaller, such that the number of available nucleation sites and space for growth is limited. As such, the re-arrangement of subgrains is difficult. In Figure 2.6, both a fully recrystallized structure (a) and a mostly fibrous structure (b) is shown. These micrographs represent two different aluminium alloys with varying content of manganese, where (a) has a low content and thus the number density of dispersoids low, leading to recrystallization. (b) has a high content, where the number density of dispersoids is high thus maintaining a fibrous structure after extrusion.

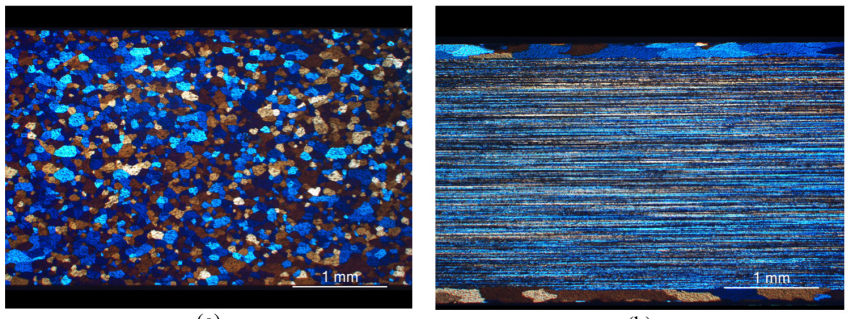

(a) (b)

Figure 2.6: Micrographs of a recrystallized (a) and a fibrous (b) aluminium structure [42].

Artificial Ageing

Aluminium is a relatively soft metal, and depends heavily on alloying elements to increase strength and hardness. Artificial ageing is the process where age-hardenable alloys

like AlMgSi is kept at an elevated temperature for typically a few hours, as opposed to natural ageing where the aluminium is kept at room temperature over the course of several weeks or months [43]. Ageing temperatures of typically 170-200 °C accelerate the precipitation process which enhances the mechanical properties. Hardness arises from several sources in the matrix, as can be seen in Equation 2.1.

$$\sigma_y = \sigma_i + \sigma_{ss} + \sigma_p \tag{2.1}$$

where σ_i describe the intrinsic strength of aluminium. σ_{ss} and σ_p are the solid solution and precipitation strength contributions respectively. Solid solution hardening is a measure of the different alloying elements' ability to increase hardness as they create elastic stress fields around dissolved atoms, while precipitates interact with dislocations which in turn also increases the hardness.

During artificial ageing, metastable and stable MgSi particles form. The particles which develop during this process is described in sequence by Figure 2.7 and Table 2.3. The equilibrium MgSi particle (Mg_2) is, as mentioned, detrimental to the quality of the aluminium. However, other stoichiometries promote positive properties such as strength. Peak hardness (T6) is reached when β" and β' both exist together as metastable phases. The pure β phase is referred to as over-aged (T7) and is the stable MgSi phase.

Table 2.3: The geometry, crystal structure and chemical composition of phases that develop during precipitation hardening in AlMgSi-alloys [26].

Phase	Geometry	Crystalline Form	Chemical Comp.
GP-zones	Semi-coherent needles	Monocline	$Mg_{2+x}Al_{7-z}Si_{2+y}$
β''	Semi-coherent needles	Monocline	Mg_5Si_6
β'	Semi-coherent bonds/needles	Hexagonal	Mg_5Si_3
β	Incoherent plates	Cubic	Mg_2Si

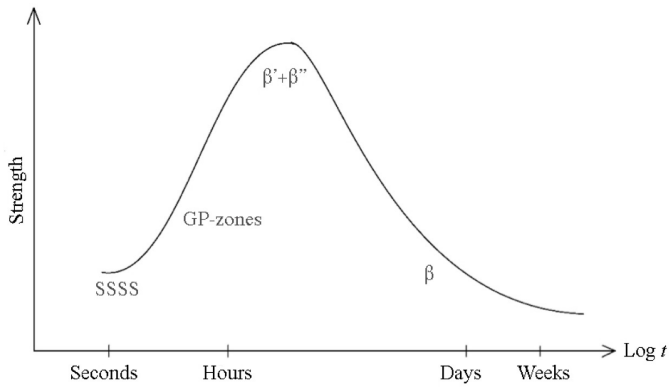

Figure 2.7: Strength evolution of AlMgSi alloys during artificial ageing with appropriate labels which denotes the presence of different phases [44].

Figures 2.8 and 2.9 show TEM images of an artificially aged AlMgSi alloy. The aforementioned shows the nanostructure of both a T6 (right) and T7 (left) aged AlMgSi alloy, while the latter shows the presence of β" phase.

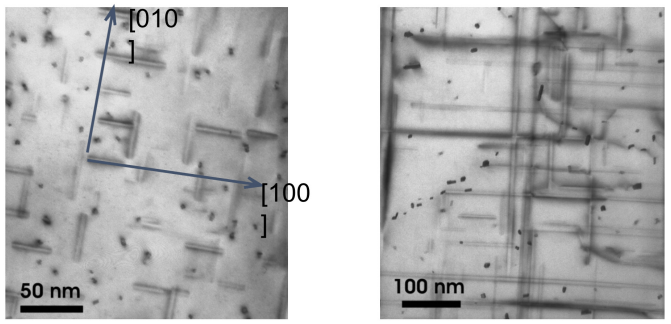

Figure 2.8: Needle shaped precipitates in peak-aged (left) and over-aged (right) AlMgSi alloy [34].

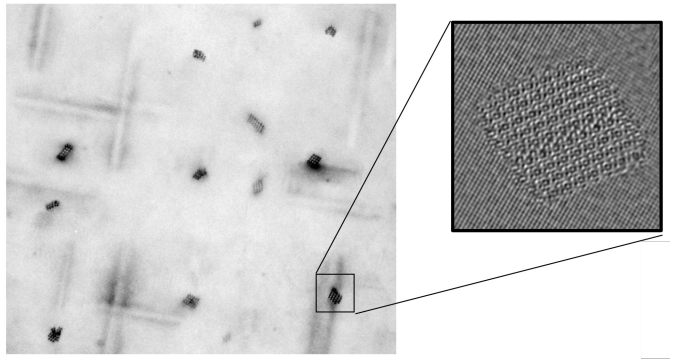

Figure 2.9: Presence of β" particles in AlMgSi alloy. The highlighted precipitate is approximately 4x4x50 nm in dimensions [34].

2.5 Computer Modelling

Computer simulations, rather than real world experiments are becoming increasingly more common, as the understanding of the underlying principles of processes are better researched, software become more sophisticated and computers become faster. Computer simulations offer a cheaper and faster way to replicate real phenomena with acceptable margins of error. In this section, the principles of programming and computer modelling laid out by Ashby will be discussed.

Physical based modelling is the principle of describing a phenomena with the fundamental principles and governing equations. Developing a model, according to Ashby, may require up to nine steps, as illustrated in Figure 2.10. Not all models require all steps, but the application of each step should be considered [48].

1: Identifying the problem may sound simple, but it often consists of several underlying subproblems with varying degree of precedence. Modelling each sub problem separately, and combine or compare thereafter is the recommended approach. Coupling of subproblems may however prove challenging. When identifying problems, it is important to make efforts towards finding describing data, experience and dependencies which can help create and verify the models.

2: In- and outputs is an essential part of the simplification process. What are the parameters the model should describe? Which dependencies do they have? It is important to eliminate factors which have a low impact on the results. These can be incorporated at a later stage.

3: Direct observation of the physical mechanisms at work is essential to modelling. If no such data is available, look for other problems which resembles the problem at hand. But be careful, assumptions without evidence can be dangerous, which is why direct experimental observation is the best option.

4: Precision is at the heart of modelling. When simplifying a problem, inaccuracies are bound to occur. The key approach is to first find a model which is within one order of magnitude, and narrowing it down by refining the model and implementing the lesser important components. Do not, however, needlessly implement factors for the sake of an incremental increase in accuracy. Simplicity is a virtue.

5: The model is the transformation from input to output. It may take an algebraic, differential or integral form, or a discretized form thereof. As fundamentally new principles are unlikely to arise, standard techniques and tools can be used.

6: Dimensions is a part of modelling, but with a particular significance. Dimensional analysis is therefore its own stage.

7: Implementing the model with readable and efficient code makes it more widely available. Existing software can help implementation of models which rely on, for instance, Monte Carlo methods or finite element approaches with high efficiency.

8: Interrogation is about verifying or rejecting the model. Does it stack up against known data, and how does it respond to extreme input? Can it be expressed in simpler terms? Can inputs be replaced by constants if they have low impact on final results?

9: The final component is about visualization. Visualization helps transfer of information between human and model when raw outputs otherwise are too complex or overwhelming to grasp in itself.

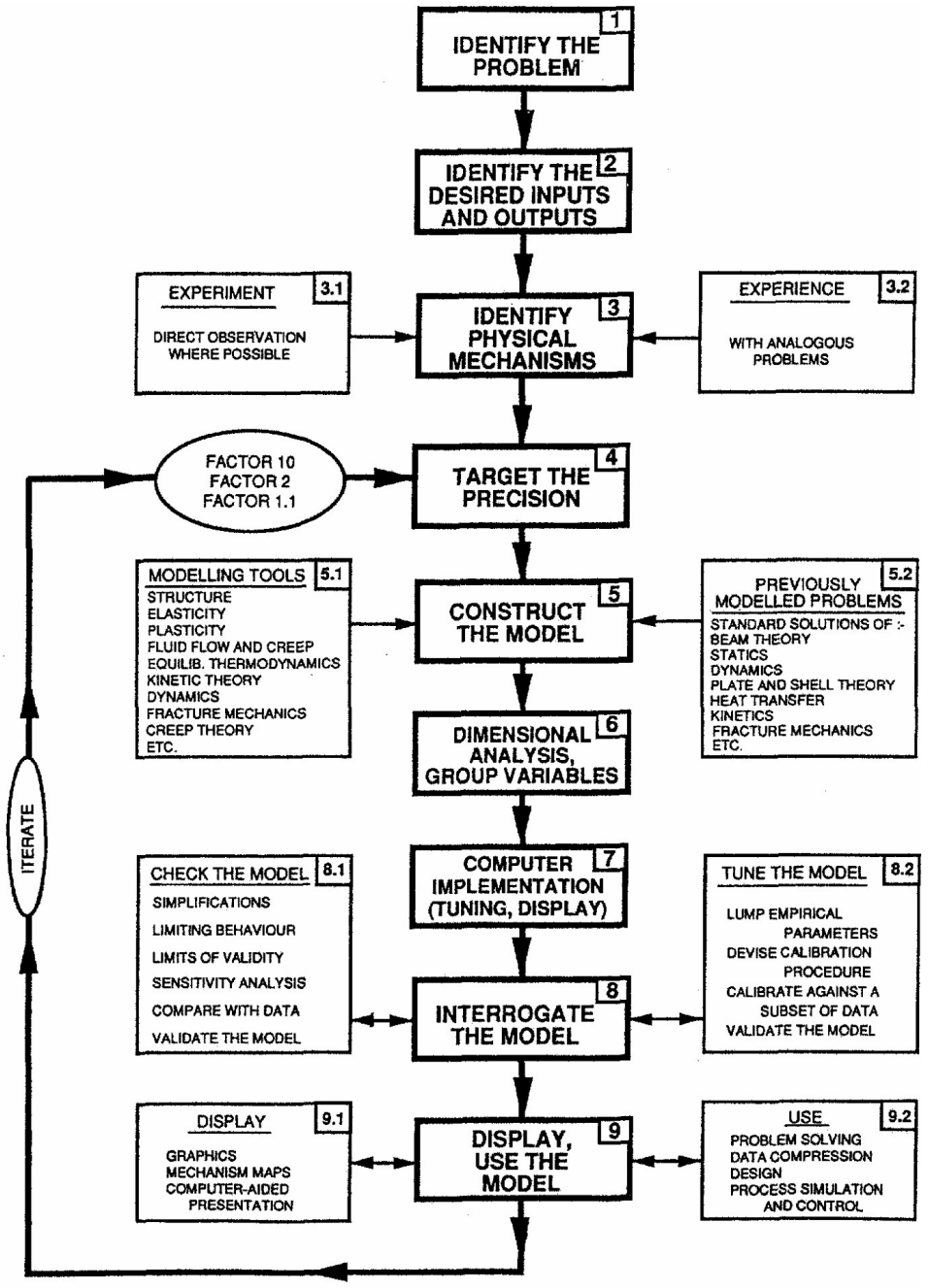

Figure 2.10: Ashby's nine stages in developing a physical model [48].

Empirical modelling is modelling which is purely based on experimental results, where the model have little to no understanding of the observed phenomena incorporated. These models may grossly oversimplify the problem, or may only be valid in a narrow range of conditions, depending on the extensiveness of the experiments on which it is built. Empirical modelling can be a simpler, or more straightforward methodology compared to physical modelling, and algorithms are explicitly defined in simple terms, which makes them easy to understand. On the other hand, machine learning, which is also a form of empirical modelling, is complex to the point where its methods are difficult, if not impossible, to understand. This limits the transfer value to humans compared to a physical model.

Optimization is the methods and approaches to finding an optimal solution(s) to a system. Although not limited to just computer science, the processing power of computers are of great help in multi-variable systems with multiple constrains and objectives. In a system, there's typically one objective which must be either minimized or maximized, while several constrains are held true. For example, the goal of a system may be to minimize the cost of production (objective), while setting the risk of failure to 0.05 or below (constraint). Objectives and constrains are often conflicting. In essence, positively affecting the objective will often negatively affect the constraints [49].

There are many methodologies in optimization, each with different strengths and weaknesses. Some methodologies might be very complex, while others are slow to converge and demands much computational power. The **MOGA** (Multi-Objective Genetic Algorithm), sometimes referred to as Pareto optimization, is an approach which will yield the Pareto curve, i.e. the curve illustrating the expected trade-off between two variables. For instance, the Pareto curve may illustrate the highest achievable yield strength as a function of production cost, a helpful tool when pricing products. The MOGA approach will not prematurely converge to a local maxima, but on the other hand may require longer computational time. The **PilOpt** approach is a quicker algorithm which aims to find optimal solutions as quickly as possible. The optimal solution exists as edge cases defined by the objectives and constrains, also known as the Pareto front. The approach is based on the combination of random input variables and machine learning. An overseeing ML algorithm will make connections between inputs and outputs, such as to discard the poor solutions and tweak the good solutions. The PilOpt approach may however converge untimely towards a local maxima as opposed to the global maxima [50].

Metamodels, or RSM (Response Surface Models), are models which describe other models, and the method of metamodelling is the generation of such metamodels. Fundamentally, metamodelling is the investigation of the behavior of in- and outputs, and an approximation of this relationship. The margin of error of these metamodels depend heavily on the Design of Experiment (DOE), as well as the complexity of the model. As metamodels build on empirical modelling, the range of tried inputs and observed outputs are essential. The DOE should trial inputs at regular intervals, and make sure that the bounds of inputs are representative of the real world. The complexity of the solution and the choice of algorithm also affects the accuracy. These discrepancies between Metamodel and the model on which it builds must be taken into account [50].

The need for, and application of metamodels come from computationally demanding and complex models where the dependencies of in- and outputs may be trivial, but depen-

dant on an unknown variable. The DOE creates the statistical basis to establish the values any hidden variables, such that the metamodel can be constructed. Metamodelling considers the model as a black box, which means that the model is unknown and unknowable, and only the direct relationship between inputs and outputs matter. A mathematical model may be fitted to the data, while the underlying mathematical process remains unknown.

2.6 Computer Models

Each segment of the through process of extruded aluminium is described by its own respective model. The casting and homogenization in this thesis is described by Alstruc Solidification and Alstruc Homogenization respectively [54]. The extrusion process is described by a metamodel which builds on HyperXtrude® [55], and the recrystallization process immediately after extrusion is described by the Alsoft model [51]. NaMo considers the precipitation during artificial ageing and how it affects the strength of the alloy [52]. Figure 2.11 sketches the workflow of the computational modelling as it compares to the through process. A brief mathematical description of each model follows in this chapter. However, due to the complexity, only core functionalities are highlighted.

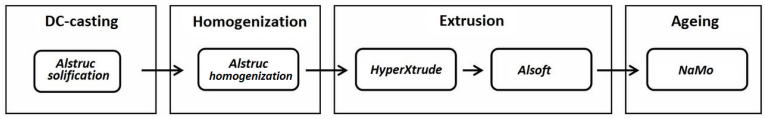

Figure 2.11: The coupling of different models [53].

Alstruc

The Alstruc program considers the solidification and homogenization process of industrial aluminium production. The solidification module predicts phase distribution and solid solution levels of an aluminium alloy which have been gradually solidified. The calculations are based on phase diagrams, and chemical composition, as well as grain size and dendrite spacing are inputs in the model. The latter two may have empirical values or they may be predicted from other software. The outputs of the module are primary and secondary phase volume fractions as well as solid solution concentrations in dendrite arms. These outputs are the inputs of the homogenization module, which, together with the inputs temperature and holding time, predicts how aluminium alloys will behave when exposed to thermal treatment. The module focuses on particle structure during phase transformation and diffusion of elements. The module also predicts dispersoid formation which are tiny particles made from elements in excess of the equilibrium concentration of the solid solution. These parameters will be used when predicting behavior during extrusion [54].

HyperXtrude®

HyperXtrude® is a proprietary software program made by Altair Engineering Inc., and can be used to model complex fluid flow and heat transfer. It is, in this case, used to

simulate the extrusion process by solving the Eulerian/ Lagrangian-Eulerian form of the governing equations in a finite element approach (FEM). Different die geometry, chemical composition, microstructure, previous thermal treatment and ram speed are the most important input parameters. The most important output parameters for the purpose of aluminium extrusion, are ram force, strain rate across the profile and deformation temperature [55].

Empirical models of the extrusion process are available, most notably the Sellars-Tegart equation, as shown in equation 2.2 (or modified in equation 2.4), which describes the strain rate as a function of steady state flow stress [8; 58].

$$\sigma_{ss} = \sigma_{_R} \operatorname{arcsinh}\left(\frac{ZH}{C}\right)^{1/n} + \sigma_{_P} \tag{2.2}$$

where $\sigma_{_R}$ and $\sigma_{_P}$ describe the deformation resistance which stems from atoms in solid solution and non-shearable particles, respectively, and are based outputs from the Alstruc module. C and n are material specific constants. The ZH expression is the Zener-Hollomon parameter, and is defined by the following equation.

$$ZH = \dot{\varepsilon} \exp\left(\frac{Q_{app}}{RT}\right) \tag{2.3}$$

where R and T are the universal gas constant and absolute temperature respectively. Q_{app} is a material specific constant, and $\dot{\varepsilon}$ is the strain rate. The Zener Hollomon parameter combines the effect of strain rate and deformation temperature and is often used in FEM via equation 2.2. Equation 2.4 offers a slightly modified version of the Sellars-Tegart relationship.

$$\dot{\varepsilon} = A\left(\sinh\left(\frac{\sigma - \sigma_P}{\sigma_R}\right)\right)^n \exp\left(\frac{Q_{app}}{RT}\right) \tag{2.4}$$

where A is a material specific constant. The remaining parameters are the same as previously explained. This strain rate expression can be approximated linearly, as shown in equation 2.5.

$$\dot{\varepsilon} = k_r \nu_{ram} \tag{2.5}$$

where k is a constant depending on die design and reduction ratio. Combining equations 2.4 and 2.5 results in the expression shown in equation 2.6.

$$\nu_{ram} = k_1\left(\sinh\left(\frac{\sigma - \sigma_P}{\sigma_R}\right)\right)^n \exp\left(\frac{Q_{app}}{RT}\right) \tag{2.6}$$

where k_1 is a constant equal to A/k_r. These equations show that both strain and ν_{ram} are dependant on deformation temperature and applied strain rate, and that the material's microstructure will affect the extrudability. The defect mechanism known as tearing is an issue which HyperXtrude® considers, these simplified expressions however, do not.

Alsoft

During extrusion, the metal is subjected to high strain rates and temperatures, and the material becomes highly deformed, which in turn may cause recrystallization. The model estimates the driving pressure for recrystallization as well as the deformation substructure. It considers the temperature, strain rate and the dispersoid number density from Alstruc. From this, the program predicts the fraction of recrystallized material as well as the average size of recrystallized grains. The simulation starts at the extrusion outlet and ends when the material is completely cooled. Instantaneous recrystallization rate is calculated once for each time step and is proportional to P_D-P_Z, where P_D represents the driving pressure for recrystallization, and P_Z represents the Zener drag pressure, which counteracts recrystallization. The total driving force for recrystallization is described in equation 2.7.

$$P = P_D - P_Z \tag{2.7}$$

The driving force for recrystallization can be described by the expression in equation 2.8.

$$P_D = \alpha \frac{\gamma_{SB}}{\delta} + \frac{1}{2} G b^2 \rho_i \tag{2.8}$$

where α is a geometry constant, γ_{SB} is the subgrain boundary energy and δ is the average subgrain size. In the last term, G describe the shear modulus and b is the Burgers vector. ρ_i is the statistical density of dislocations. This term is typically approximated to zero. The γ_{SB} can be expressed using the Read-Shockley relation, as stated in equation 2.9.

$$\gamma_{SB} = \frac{G b \Theta}{4\pi(1-\nu)} \ln\left(\frac{\Theta_c}{\Theta} e\right) \tag{2.9}$$

where ν is the Poisson ratio, Θ is the mean subgrain misorientation, and Θ_c is the critical value where a sub-boundary becomes a high-angle boundary. Furthermore, δ can be calculated iteratively using the Zener-Hollomon parameter (Z), and the temperature is calculated by the empirical relationship described by equation 2.10.

$$\frac{1}{\delta} = \frac{RT}{A^*} \ln\left(\frac{ZH\delta^2}{B^*}\right) \tag{2.10}$$

where the Zener-Hollomon parameter is the same as in equation 2.3. For equations 2.10, R is the universal gas constant and T is absolute temperature, while A^* and B^* are specific material constants. Both deformation temperature and strain rate are outputs from HyperXtrude®.

The Zener drag pressure (P_Z) is given by equation 2.11.

$$P_Z = \frac{3}{4} \frac{f \gamma_{GB}}{r_d} \tag{2.11}$$

where f is the volume fraction and r is the radius of dispersoids which forms during recrystallzation. Both are outputs from the *Alstruc* module. γ_{GB} describes the grain boundary interface energy.

When driving forces are calculated, nucleation and growth kinetics can be derived. The recrystallization kinetics model is an extension of the classical Johnson-Mehl-Kolmogorov-Arvrami (JMAK) approach, treating recrystallization as a nucleation and growth process [57]. The recrystallization reaction in Alsoft is a result of oriented nucleation, and three types of nucleation sites are considered.

- nucleation from deformation zones, around large particles (PSN).
- nucleation from old grain boundaries.
- nucleation from retained cube bands.

Moreover, the recrystallization calculations are based on the standard assumptions of site saturation nucleation kinetics and a random distribution of nucleation sites. Fraction recrystallized material is calculated by equation 2.12.

$$X(t) = 1 - \exp(-N_{tot}(Gt)^3) \tag{2.12}$$

where t is the elapsed time. N_tot is the total number of nuclei, and G is the growth rate. When the fraction recrystallized (X(t)) is calculated, the grain size of the recrystallized regions can be calculated with the expression in equation 2.13.

$$D = \left(\frac{1}{N_{tot}}\right)^3 \tag{2.13}$$

Where N_{tot} (= N_{PSN} + N_{Gb} + N_{cube}) is the number of nuclei , which can be calculated by the initial material chemistry, grain size and texture, and deformation conditions [57]. G the growth rate of recrystallized grains defined by equation 2.14.

$$G = M(P_D - P_Z) \tag{2.14}$$

where M is the grain boundary mobility, being inversely proportional to the concentration of elements in solid solution [57], and P_D and P_Z are the driving force for recrystallization and Zener drag, as previously denoted. Using these equations, recrystallization can be described after thermomechanical deformation.

NaMo

The ageing process is described by the NaMo model, which considers the nano structure during heat treatment in terms of precipitation and associated strength. The model predicts evolution of particles in the nanometer range (10^{-9}) and the outputs are yield strength (σ_y) and ultimate tensile strength (σ_m) as well as elongation to necking (e_u). Ageing temperature, holding times as well as the rate of heating and cooling are inputs.

The NaMo model is a physical based model, and is based on classical theories for nucleation, growth and coarsening of particles. Nucleation rate is dictated by equation 2.15.

$$j = j_o \exp\left(-\frac{\Delta G^*_{het}}{RT}\right) \exp\left(-\frac{Q_d}{RT}\right) \tag{2.15}$$

where the Gibbs energy term is defined by equation 2.16.

$$\Delta G^*_{het} = \frac{A_0^3}{RT^2[\ln \bar{C}/C_e]^2} \tag{2.16}$$

where R and T are the universal gas constant and absolute temperature respectively, j_0 is a reference rate of nucleation which depends on the material. The Gibbs energy term (ΔG^*_{het}) is the heterogeneous nucleation barrier, and Q_d is the activation energy for diffusion. The growth rates of precipitates is given by the equation 2.17.

$$\nu = \frac{dr}{dt} = \frac{\bar{C} - C_i}{C_P - C_i}\frac{D}{r} \tag{2.17}$$

Where C_i is given by equation 2.18.

$$C_i = C_e \exp\left(\frac{2\gamma V_m}{rRT}\right) \tag{2.18}$$

Here, r and D are the radius of particles and the diffusion constant respectively. $\bar{C}$ is the mean solute concentration, C_i is the concentration at the particle-matrix interface, and C_p is the concentration of the element in the particle. With these combinations of equations, the NaMo model accounts for the combined effects of nucleation, growth and coarsening of precipitates.

How the dislocations interact with the precipitates is highly influential on the strength contribution. From Figure 2.12, (a) illustrates how elements in solid solution create an elastic stress field in the aluminium matrix. When considering precipitation hardening and coherency, two types of particle-dislocations interactions take place, based on the particle size. Bypassing (b), or Orowan looping, happens with large particles, where the radius is larger than the critical radius (r_c), while shearing (c) happens when a radius is lower than the critical radius, and particles are coherent. Equations 2.19 and 2.20 describe the interaction forces between Orowan looping (b) and shearing (c) and precipitates in the two respective cases.

$$F_i = 2\beta G b^2 \tag{2.19}$$

$$F_i = 2\beta G b^2 \left(\frac{r_i}{r_c}\right) \tag{2.20}$$

The average contribution of all these interactions result in $\bar{F}$ as seen in equation 2.21.

$$\bar{F} = \frac{\sum_i N_i F_i}{\sum_i N_i} \tag{2.21}$$

where N_i is the number density of each type of dislocation, and F_i is the mean interaction force between each type of dislocation and precipitates. This mean interaction force is further used to calculate the precipitate hardening contribution as shown in equation 2.22.

$$\sigma_{_P} = \frac{M_r}{b^2\sqrt{G}}\sqrt{\frac{N_v r}{\beta}}F^{3/2} \tag{2.22}$$

where M_r is the Taylor factor, b is the Burgers vector and G is the shear modulus. β is a constant with approximate value of 0.5, N_v and r are the number density and mean radius of the precipitates respectively. F is, as mentioned, the average interaction force between dislocation and precipitates. The solid solution contribution is given by equation 2.23.

$$\sigma_{ss} = \sum_j k_j C_j^{-2/3} \tag{2.23}$$

The extended version of the NaMo-model calculations produce the full stress-strain curve. From this, ultimate tensile strength and elongation to necking is easily derived [56].

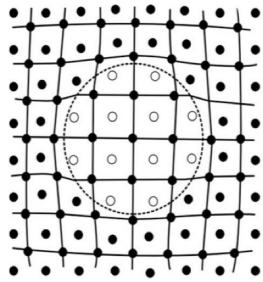

(a) Solid solution hardening

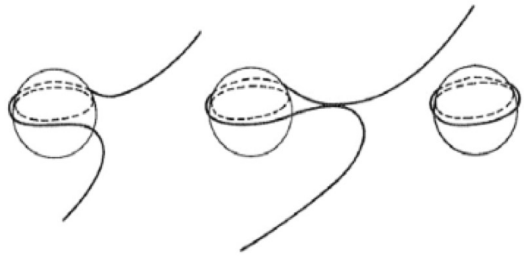

(b) Bypassing

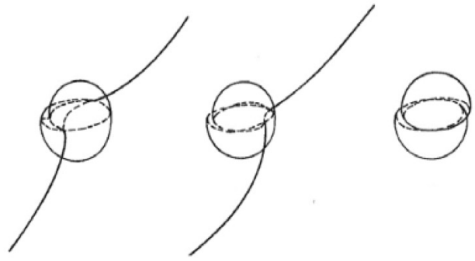

(c) Shearing

Figure 2.12: (a): Elastic stress field in solid solution. (b): Bypassing dislocation moving around large precipitate particle. (c): Shearing dislocation moving through a small precipitate particle [46].

modeFRONTIER™ is an optimization platform developed by ESTECO SpA [50]. It's a workflow based environment and applied multi-objective optimization algorithms are used for streamlining the engineering process in a manner which reduces time and cost while obtaining improved results, according to ESTECO. modeFRONTIER™ has three different environments, which each serve an essential purpose.

The first environment is the Workflow Editor. The workflow is a graphical representation of the problem and describes how the simulations are conducted, and in which order. A workflow requires an explicit description of in- and outputs and one or more objectives for optimization. The second environment is the Run Analysis, which runs the workflow, analyses the input and output and makes changes based on the results with the use of optimization algorithms. The third environment is the Design Space. This environment visualizes the results, and contains many tools which can be used to extract data in a comprehensible way such that the user can make informed decisions.

This tool have been used to tie the different computational models together in a workflow that represents the through process of extruded aluminium, as described in Section 2.4. The optimization tools will attempt to identify values of the controllable input parameters such that manufacturers can adjust their process and produce alloys with better properties.

Chapter 3

Methodology and Process

3.1 Alloys

In this study, the goal is to identify an extruded aluminium alloy with superior structural properties to existing products in the market. The PRO^{3TM} framework will be used to predict mechanical and structural properties of the finished product based on the controllable inputs such as chemical composition, homogenization treatment and extrusion treatment. The product would ideally be of similar chemical composition as existing alloys. The production route will follow the process described in Section 2.4, i.e. cast, homogenized, extruded and artificially aged. The results from this thesis will also be used to polish and calibrate the different computer models in PRO^{3TM}.

During the specialization project in the autumn semester of 2018, four different alloys and two different homogenization treatments were chosen as suitable candidates for this pilot project. This Master's thesis will build on the foundations of the specialization project. All four alloys have the same base composition, varying only in levels of iron (Fe) and chromium (Cr). The base composition can be found in Table 3.1, while the alloy specific composition can be found in Table 3.2.

Two different homogenization treatments were chosen. Both variants are described in Table 3.3.

3.2 Metallurgical Processing

In this section, the process starting from molten aluminium to finished product will be discussed. As previously discussed, the aluminium was cast, homogenized, extruded and artificially aged. Each of the following subsections will discuss how each step was conducted experimentally for this thesis.

3.2.1 Casting

Each alloy was cast and cut into a billet with dimensions 300mm length and 95mm diameter. The billets were cast at the foundry at Hydro Sunndalsøra with chemical composition as specified by Table 3.1 and 3.2.

Table 3.1: Base chemical composition for all selected alloys.

Element	Si	Cu	Mn	Mg	Ti	Zn
Composition [wt%]	1.0	0.01	0.4	0.61	0.01	0.0

Table 3.2: The levels of chromium and iron in the different alloys.

Alloy	**Chromium [wt%]**	**Iron [wt%]**
1	0.1	0.2
2	0.2	0.2
3	0.1	0.4
4	0.2	0.4

3.2.2 Homogenization

The billets were homogenized in industrial ovens at Hydro Sunndalsøra, as specified by Table 3.3. Both variants were heated from room temperature to holding temperature at a rate of 200 °C/hr and cooled from holding temperature to room temperature at a rate of 350 °C/hr.

Table 3.3: Homogenization variations for selected alloys. Variation A is short at high temperature. Variation B is longer but at lower temperature.

Variant	**Temperature [°C]**	**Time [hours]**
A	585	1
B	555	6

3.2.3 Extrusion

The billets were transported from Sunndalsøra to Trondheim, where they would be extruded in the hydraulic press owned by SINTEF at Gløshaugen. Figure 3.1 illustrates the geometry and dimensions of the extruded profile.

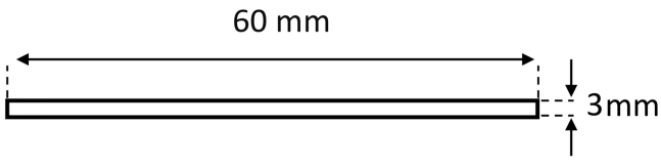

Figure 3.1: Cross section of the flat rail extrusion profile.

Test billets with similar chemical composition were first extruded such that the threshold for tearing could be found prior to extruding the experimental samples. All runs in the hydraulic press used two different ram speeds, which means that the ram speeds would, ideally, have to be on both sides of the threshold between tearing and no tearing. Likewise with recrystallization. For each press, the billet was preheated to 460 °C. Each billet is 300 mm long. With a reduction factor of 35, the total maximum length of the extruded rail will span 10.5 meters. From the exit of the extrusion press, there's a 3.5 meter long tube leading into a water quench box. Each press would yield a full profile with three different sections. Section 1 would be lower speed and water quenching. Section 2 would be higher speed and water quenching, while Section 3 would be higher speed and air cooling, as it could not reach the quench box. The deformation temperature of the extruded billets could not be measured accurately. After the profile had reached room temperature, they were put into a freezer to avoid natural ageing. Table 3.4 and Figure 3.2 summarize the parameters of the extrusion experiment.

Table 3.4: Extrusion parameters for all samples. Temperature in °C, extrusion speed are in mm/s and ram force in kN.

Sample	**Preheat Temp**	$\nu_{ram,1}$	$\nu_{ram,2}$	$\mathbf{F}_{min}$	$\mathbf{F}_{max}$
1A	460	20	26	2719	3951
1B	460	20	26	2826	3989
2A	460	20	26	2777	4084
2B	460	20	26	2760	4019
3A	460	20	26	2781	4093
3B	460	20	26	2745	4078
4A	460	26	30	2889	4326
4B	460	26	30	2863	4214

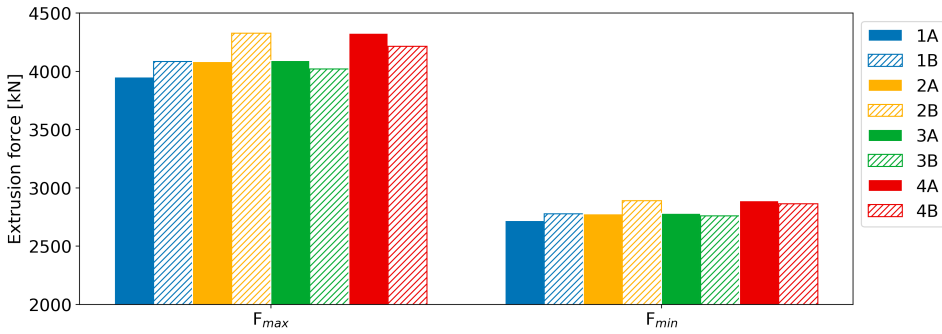

Figure 3.2: Maximum and minimum extrusion force for all samples.

Two billets were preheated to 540 °C before extrusion. Both of these samples experienced devestating tearing, and caused a jam in the hydraulic press which lead to longer breaks in the experiment. Figures 3.3 and 3.4 are pictures taken of the extruded profiles which were preheated to 540 °C.

Figure 3.3: Full view of the torn profile.

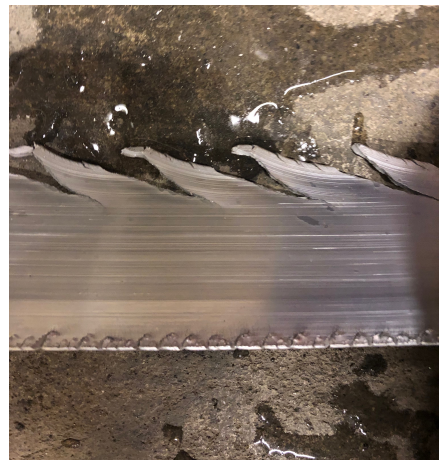

Figure 3.4: Close up of the torn profile.

3.2.4 Artificial Ageing

Samples from each profile were extracted, and cut into pieces of approximately 1cm x 1cm. Hardness would be measured at five different periods during artificial ageing. As such, one parallel for each of the five ageing time as well as one as-extruded parallel of all three sections in all eight samples gave 144 samples of extruded aluminium. The samples were held in room temperature for approximately 3 days before ageing. An air circulating oven (Naberterm N17/HR) was used to treat all samples. The oven was preheated to 180 °C before inserting the samples, and after the given ageing time had passed, the samples were immediately quenched in water. Samples were artificially aged according to Table 3.5.

Table 3.5: Ageing time and temperature for the extruded aluminium samples.

Temperature [°C]	**Ageing time [min]**				
180	2	10	100	300	1000

3.3 Metallographic Testing

The main focus of this section will be the preparation and metallographic testing of the alloys. This includes optical microscopy for microstructure imaging, and SEM BSE (back-scatter electron) imaging for dispersoids, as well as testing for hardness and electrical conductivity. For both microstructure and dispersoids, the samples were prepared in the following way.

Samples from the extruded aluminium were cut into pieces as illustrated by Figure 3.5 and molded with EpoFix resin.

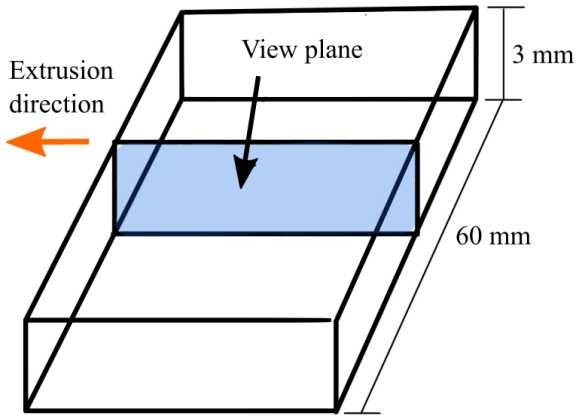

Figure 3.5: Illustration of sample size and dimension.

The molded samples were cut as to expose the aluminium on both sides of the epoxy housing, then grinding was done with the STRUERS TegraPol-31 with increasingly finer silicon carbide paper (P320, P800, P1200, P2000). Here, water was used as a lubricant and as a means to transport away loose particles, and to keep the specimen cooled. All samples were rinsed with water and alcohol between each grinding step.

When a satisfactory surface evenness had been achieved, the samples were polished in the same STRUERS TegraPol-31 machine, using 9 μm Largo, 6 μm Mol, 3 μm Mol and 1 μm Nap polishing discs. Samples were cleaned in an ultrasonic bath between each step, and rinsed with alcohol. An additional step of vibration polishing at 50 nm was considered, but dropped due to low availability of the Buehler VibroMet^{TM} vibratory polisher.

3.3.1 Microstructure

Using the prepared samples, each epoxy housing was encased in aluminium foil such that electrical contact could be made between the anodizing solution and the STRUERS LectroPol-5 machine. The software of the anodizing process was limited to 20 volt and 1 ampere. The anodizing liquid was a solution of 5 % HBF_4 and 95 % water. Samples were anodized for 120 seconds. Samples were immediately rinsed with ethanol and dried afterwards.

The microstructure was observed using optical microscope and polarized light with a sub-parallel lambda plate. Images were captured using ProgRes Capture v2.8.8. Samples were viewed in the plane parallel to the extrusion direction, as illustrated by the *View plane* in Figure 3.5. Due to the small viewing area of the microscope, each image in Section 4 is stitched together from three images.

3.3.2 Dispersiods

Using the molded samples, each epoxy housing was encased in aluminium foil, together with conductive copper tape to ensure electrical contact between the exposed aluminium sample and SEM housing unit. Samples were left in an oven at 65 °C overnight,

and cleaned using a Fischione Instruments Model 1020 Plasma Cleaner. A FESEM, Zeiss Ultra, 55 Limited Edition was used with a BSE filter to see secondary phases in the samples. Images were taken at x500, x1k and x5k magnification, at approximately 10 mm working distance at 15 kV voltage. An assumption was made that the dispersoids were not affected by the thermomechanical deformation during extrusion. The air-cooled section of the extruded profile might have been used during SEM analysis under the aforementioned assumption that it wouldn't exhibit a measurable difference. Figure 3.6 shows a processed image from SEM. The software GIMP 2.10 (GNU Image Manipulation Program) was used to enhance the contrast of the image. The image analysis was done with in-house software developed by PhD candidate Håkon Wiik Ånes at NTNU. A brief description of the software can be found in Section 3.4.3 and Appendix B.2.

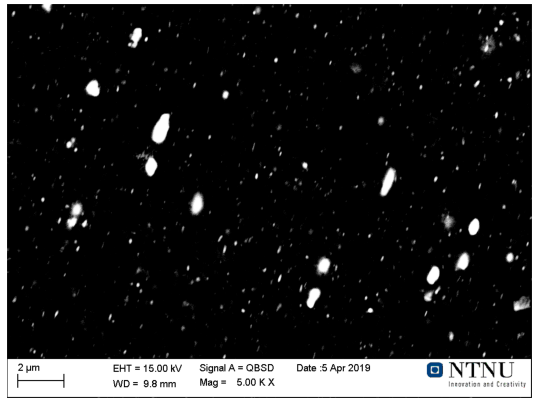

Figure 3.6: Post processed image from SEM. Dark areas are aluminium, while white areas are dispersoid particles.

3.3.3 Hardness

The hardness of each alloy was measured using a Zwick/Roell ZHV30 Vickers hardness testing machine and Zwick/Roell ZHμ HD software. The software was programmed to make a total of five imprints with consistent spacing, using 1 kg force and 10 seconds dwell time. The hardness of the alloy is was calculated using the average of all five imprints. For all 144 samples, 720 imprints were made.

3.3.4 Electrical Conductivity

The electrical conductivity was measured using the Foerester Sigmatest 2.069 equipment. The tool was calibrated first at air point, then at 58.5 MS/m and lastly at 4.415 MS/m. The frequency was set to 60 kHz, and probe diameter was 7 mm. All samples were artificially aged for 5 hours prior to testing, believed to be peak aging (T6), and conductivity was measured in the extrusion plane, i.e. the surface of the extruded profile. The result is the average of three measurements in different parts of the profile. Room temperature was 25 °C at the time of measurement.

3.4 Modelling Procedure

In this section, the modelling procedure will be described. This includes modelling in both HyperXtrude® and modeFRONTIER™, as well as some routines in Python, version 3.7. When setting up a new system, input and output variables must be declared. Input variables must have reasonable lower and upper bounds, and the explicit relationship between inputs and outputs must be coded. A metamodel had to be constructed to replace HyperXtrude® in the PRO$^{3\text{TM}}$ workflow. The metamodel is integrated in the modeFRONTIER™ environment, and simulations were initiated. Then, post-processing of data were conducted both natively in modeFRONTIER™, and in Python 3.7 with the use of an Excel spreadsheet. Different tools were created to automate and simplify the procedure, these are presented last. Figure 3.7 schematically describes the PRO$^{3\text{TM}}$ workflow.

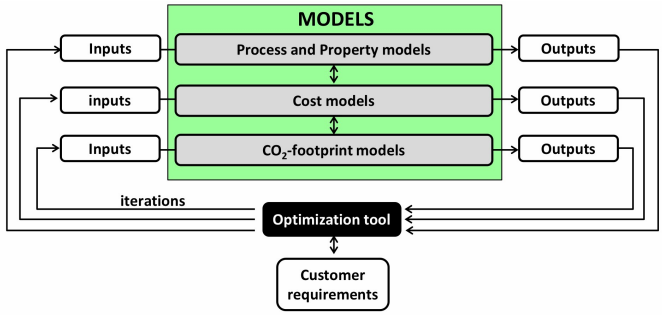

Figure 3.7: Outline of the PRO$^{3\text{TM}}$ concept [8].

3.4.1 HyperXtrude®

A metamodel of the extrusion process was necessary due to the enormous processing power demanded by HyperXtrude®. By creating a metamodel, each alloy simulation could be completed in only six minutes, compared to one to two hours for each iteration in HyperXtrude®. To create a metamodel, a DOE (Design of Experiment) was created in modeFRONTIER™. Lower and upper limits for each variable was set according to Table 3.6, and step length was defined such as to make four to six different step lengths for each variable, which yields between 30 and 40 unique combinations. The complete DOE is enclosed in Appendix E. $\sigma_{_P}$, $\sigma_{_R}$ are both outputs from Alstruc and are dependent on microstructure, while ν_{ram} is an independent input.

Table 3.6: Bounds for input variables in HyperXtrude®.

Input variable	Min	Max
ν_{ram} [mm/s]	4	20
σ_p [MPa]	0.8	2.6
σ_r [MPa]	16.6	17.9

The outputs of interest, which were used in constructing this metamodel, are strain rate ($\dot{\varepsilon}$), deformation temperature and ram force. From equation 2.5 in Section 2.6, it can be seen that the strain rate is linearly dependent on the ν_{ram}. The deformation temperature and the ram force are both dependent on all three input variables, ν_{ram}, σ_P and σ_R.

When simulations in HyperXtrude® were completed, post-processing of results was conducted. The maximum temperature of the profile and strain rates throughout the profile thickness (one in the surface (95 %), one in an intermediate position (75 %) and one in the middle of the profile (50 %)), were documented. The data set were tabulated into the DOE file, and exported to modeFRONTIER™, where RSMs were created for each of the outputs.

RSM, or Response Surface Model, is the metamodel function in modeFRONTIER™ where outputs and their dependencies are specified, and a curve-fitting algorithm can be chosen. The SSANOVA algorithm was chosen for both deformation temperature and ram force, while a linear approach was chosen for strain rate. The margins of error of the metamodel were deemed acceptable as they were lower than what can be controlled in an experimental trial, and much less so than in an industrial process.

Figures 3.8 and 3.9 shows the temperature gradient and strain rate gradient in the rail profile respectively.

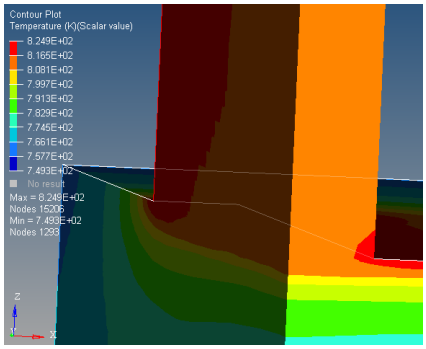

Figure 3.8: Temperature gradient through profile in HyperXtrude®.

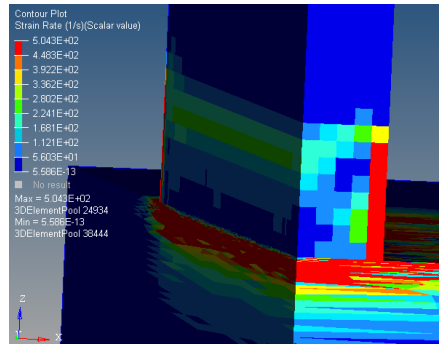

Figure 3.9: Strain rate gradient through profile in HyperXtrude®.

3.4.2 modeFRONTIER™

In this section, the workflow, as outlined in Figures 2.10 and 3.7 will be discussed. For the purpose of this thesis, only the most important metallurgical aspects will be highlighted. Cost and environmental models, as well as surface appearance, electrical and thermal properties will be neglected. The section aims to explain, in detail, the transfer of information between different models, as well as general procedure in modeFRONTIER™ optimization. In Appendix D, the real work-flow from modeFRONTIER™ is illustrated. The only variables during this procedure have been the chemical composition, homogenization temperature and holding time, and ν_{ram}, the other parameters, which could be considers inputs, are held constant and are representative of experimental or industrial conditions. The objectives of the optimization are listed in Table 3.7.

Table 3.7: Objectives of the optimization in the PRO^{3TM} workflow.

Property	Objective
Extrusion speed	Maximize
Recrystallization grain size	Minimize
Recrystallization fraction	Minimize
Probability of tearing	Minimize
Yield strength	Maximize

First and foremost, chemical composition is chosen, this *can* be used to calculate the cost of production in the HalOpt module, which was not considered in this thesis.

Alloy chemistry is imported to Alstruc Casting, which uses these parameters to calculate the solid solution, iron-bearing phases and Mg_2Si primary and secondary particles during gradual solidification.

These outputs are inputs together with variable input values for holding temperature and holding time and are transferred to Alstruc Homogenization. The homogenization module calculates changes in particles, formation and changes to dispersoids and elements in solid solution, which in turn results in the σ_P and σ_R. Chromium is suspected to be poorly handled by the Alstruc Homogenization module, and an empirical model is used to adjust accordingly.

ν_{ram} is, as mentioned, an independent input, and together with σ_P and σ_R, deformation temperature, strain rates and ram force are calculated in the RSM module.

Together with cooling parameters, these outputs are iterated three times in Alsoft, once for each position along the cross-section of the profile. This allows the module to calculate the fraction recrystallized (eq. 2.12), as well as the average size of grains throughout the profile (eq. 2.13).

NaMo calculates the precipitation behavior during aging and the associated stress-strain behavior, from which the yield strength is calculated.

This concludes one iteration of the model. Outputs, objectives and constraints are analyzed by the optimization tool, inputs are adjusted, and the optimizer tool will attempt to converge towards optimal solutions.

When a few good solutions had been identified, the chemical composition and homogenization was locked to reflect alloys 1 through 4 and Hom. A and B. Then, only extrusion ram speed was variable, as to see how extrudable these alloys are. Also, this would make it easier to keep track of the material properties as a function of ram speed.

3.4.3 Developed Tools

Working with the PRO^{3TM} software generates large amounts of data, and only a skilled engineer, with intimate knowledge of physical metallurgy and software is able to process data and make informed decisions. To lessen the workload, reduce error rate and lower the threshold for required computer skills, a few scripts have been developed. All scripts have been developed in Python 3.7.

Metamodel pre-processing tool

This script reads the DOE Excel file and creates all the necessary files and directories such that HyperXtrude® simulations can be run with all different input variables as specified by the DOE. This process would otherwise be a very tedious task to perform manually, and may be very prone to error. Errors in this process would be very detrimental to the accuracy of the metamodel.

Metamodel post-processing tool

This script reads the output files from HyperXtrude® and exports them into an Excel sheet which can be directly imported in the RSM module in modeFRONTIER™. This task would also be very daunting for a human operator, as well as time consuming.

In the long term, a universal metamodel which will supersede HyperXtrude® is desirable. However, more data is required. The application of these two scripts greatly reduce the human labor required to initiate simulations in HyperXtrude®, which may bring this goal closer.

modeFRONTIER™ post-processing tool

Over 220,000 data points was generated by modeFRONTIER™ during this trial, and there is an urgent need for a tool to extract relevant data and visualize them in a purposeful manner. The script imports data from the relevant Excel spreadsheet, and processes the results, in a way which generates plots for predetermined relationships, and organizes them into descriptive folders. To give an example, one can request all the different chemical components and see how they affect the yield strength. The graphs will be put in a folder named 'Chemistry'. Using this program eliminates the need for skills related to modeFRONTIER™, Excel or any programming language when processing results. It also eliminates some of the guess-work that an inexperienced engineer might experience when looking for important relationships. It takes approximately one minute to generate 20 graphs. Currently, it only processes 2 dimensional scatter plots, i.e. x and y-axis. However, there is no reason why this couldn't be expanded to include more types of plots. Even still, only and experienced metallurgical engineer can make good use of the results. At this point, it should be emphasized how powerful the visualizer from modeFRONTIER™ is. The presented script will only serve as a way to quickly generate many plots and skim through the results.

Dispersoid processing tool

The dispersoid processing tool was developed by PhD candidate Håkon Wiik Ånes, using open source software. The software as the following procedure [61]. A more elaborate explanation with images is found in Appendix B.2.

1. Import and inspect data.
2. Detect particles based on image intensity using region-based segmentation.
    - Create an elevation map.

- Find markers of each particle.
- Perform a watershed transformation by flooding elevation map.

3. Segment image into particles and analyse properties.
    - Segment image from binary image.
    - Get particle properties.
    - Remove wrongly segmented particles.
4. Plot results.

Building on the software from Ånes, a script was developed such as to process all stored images from all samples. The routine merges images, analyzes the particles and exports properties to a .csv file according to the workflow listed above. These files are imported into a plotting tool, which calculates, compares and plots the data from the dispersoid processing tool, as well as curve fitting. The results can be found in Section 4.3 and in Appendix B.1. This script is somewhat computationally demanding, but is in return completely automated.

Chapter 4

Results

In this chapter, the thesis' results will be presented. This includes the alloy design results from PRO^{3TM}, the microstructure, dispersoid analysis, tearing tendencies, material hardness and electrical conductivity. Comparisons to software simulations will be made.

4.1 Alloy Design

In this section, the results from the PRO^{3TM} simulations which laid the foundation for the alloy design, will be presented. The key properties of the desired alloy is high yield strength, little recrystallization, low probability of tearing and ability to be extruded at high speed. Figure 4.1 shows the trade-offs between yield strength and extrusion speed for all simulated alloys.

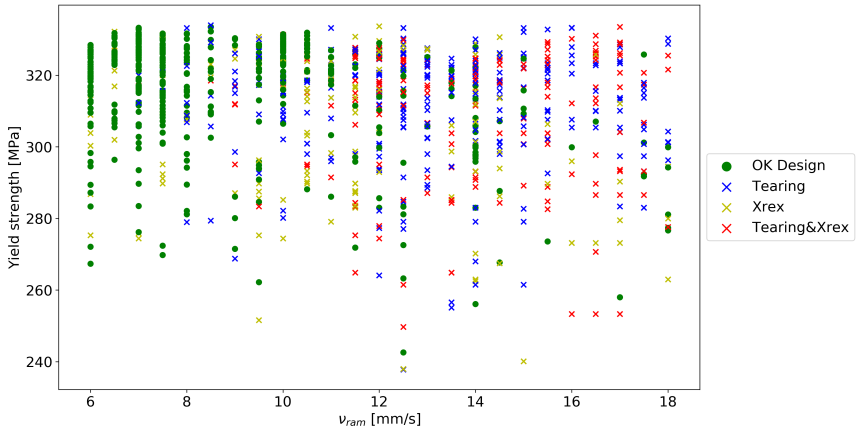

Figure 4.1: PRO^{3TM} simulation of ram speed vs yield strength.

When filtering away the non-viable results, i.e. the alloys with tearing and recrystallization, Figure 4.2 emerges, and a Pareto curve can be suggested.

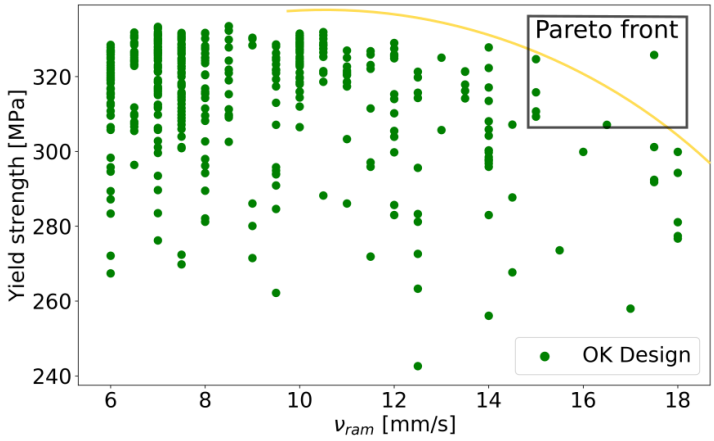

Figure 4.2: PRO^{3TM} simulated viable Pareto curve.

Let's consider only the Pareto front. Figure 4.3 shows each of these alloys with corresponding ID. Table 4.1 underlines how each ID a result of different input parameters.

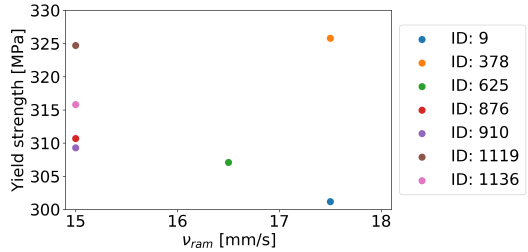

Figure 4.3: PRO^{3TM} simulated alloys within the Pareto front.

Table 4.1: The chemical composition, homogenization and extrusion parameters for each alloy in the Pareto front. Units in wt%, °C, hours and mm/s.

ID	Cr	Cu	Fe	Mg	Mn	Si	T_{hom}	t_{hom}	T_{billet}	ν_{ram}
9	0.18	0.05	0.059	0.62	0.52	0.82	490	3	440	17.5
378	0.22	0.06	0.255	0.94	0.6	1.1	480	3	440	17.5
625	0.25	0.09	0.353	0.64	0.52	0.9	550	4	440	16.5
876	0.25	0.1	0.353	0.66	0.54	0.92	550	4	440	15
910	0.25	0.08	0.353	0.66	0.54	0.92	550	4	440	15
1119	0.24	0.01	0.157	1.14	0.7	1.1	500	8	445	15
1136	0.25	0	0.059	0.92	0.64	0.98	510	6	440	15

The design of the alloy has to take into account the different failure mechanisms. This concerns mainly the probability of tearing and the fraction of recrystallization. The design matrix can be seen in Figure 4.4. The lower left quadrant represents alloys with no failure. The lower right and upper left represent recrystallization and tearing respectively, while the upper right represents both tearing and recrystallization.

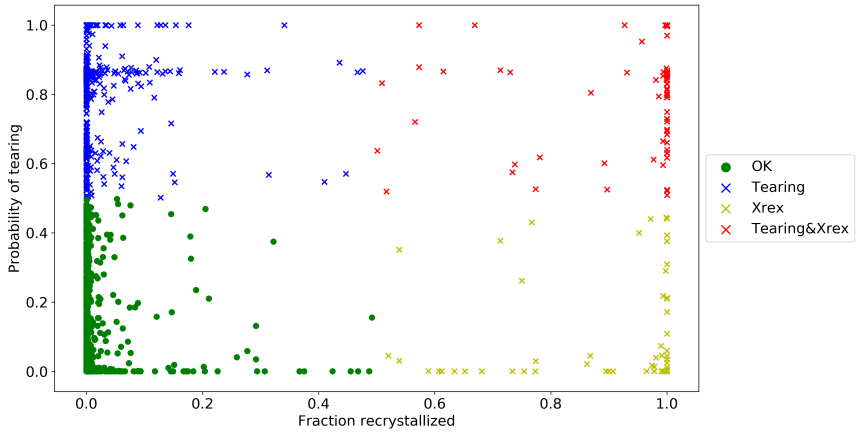

Figure 4.4: Failure mechanism matrix.

Recrystallization

The recrystallization depends on the balance between driving forces for recrystallization, P_D and Zener drag, P_Z. Figure 4.5 shows how the Zener drag affects the recrystallization of each alloy.

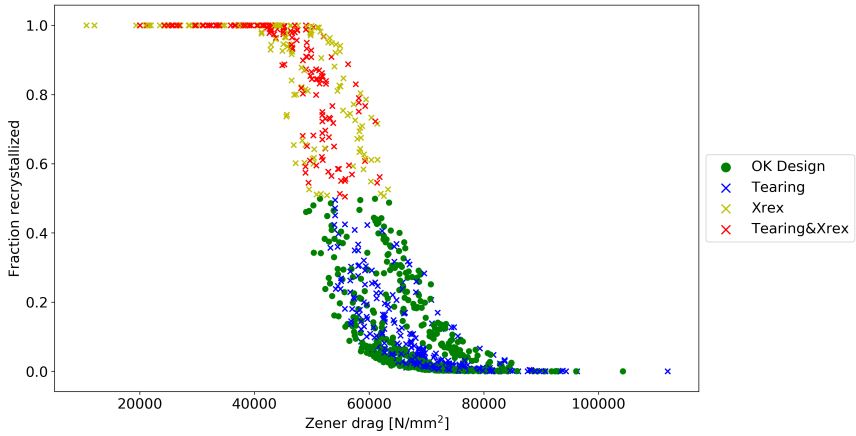

Figure 4.5: PRO^{3TM} simulated recrystallization as a function of Zener drag.

As shown in Figure 4.6, the Zener drag increases with increasing dispersoid number density. The number density of dispersoid particles increases with increasing manganese content, as seen in Figure 4.7, and manganese can be traded off against chromium to maintain the fibrous structure as seen in Figure 4.8.

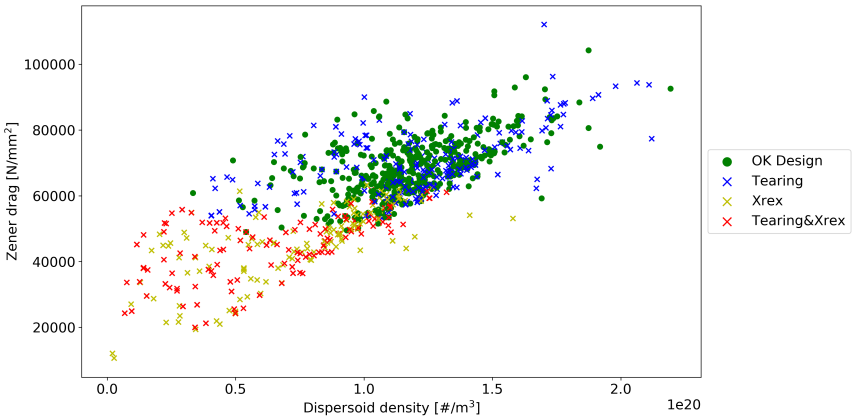

Figure 4.6: PRO^{3TM} simulated dispersoid density's effect on Zener drag.

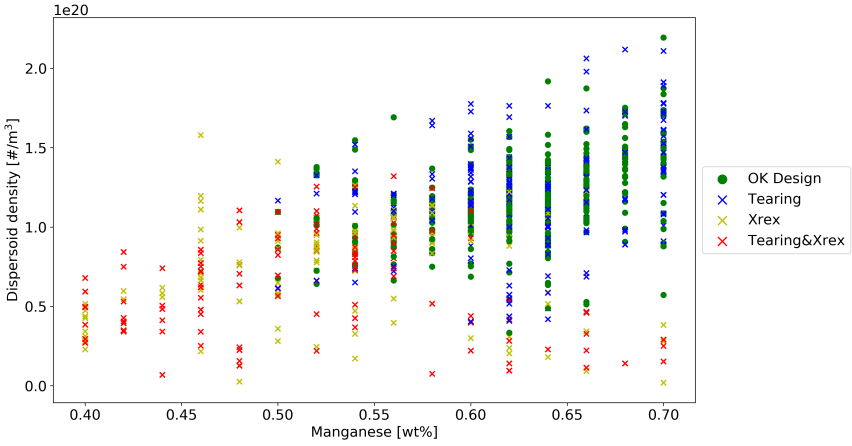

Figure 4.7: PRO^{3TM} simulated dispersoid density with increasing manganese content.

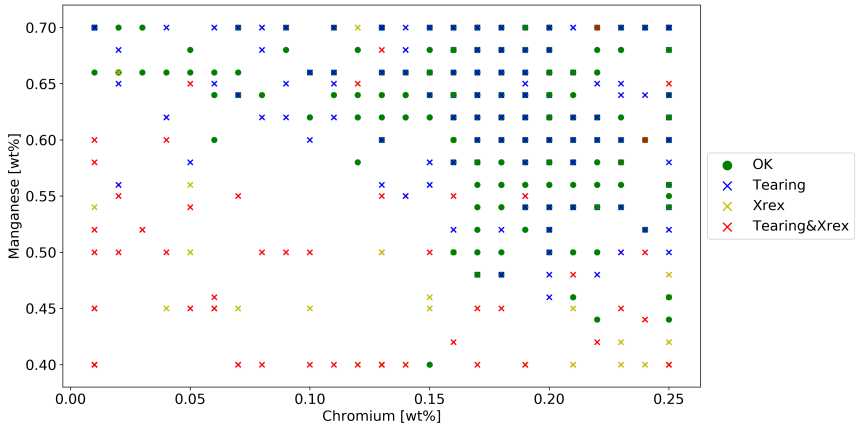

Figure 4.8: PRO^{3TM} simulated trade-off between manganese and chromium.

Tearing

The tearing mechanism is initiated by local melting in the metal during extrusion. Typically, the presence of Mg_2Si primary and secondary particles will increase the likelihood of tearing, as seen in Figures 4.9 and 4.10.

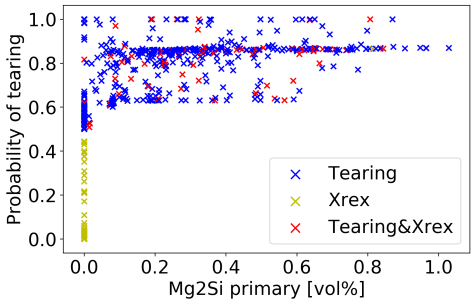

Figure 4.9: Effects of primary Mg_2Si particles on tearing.

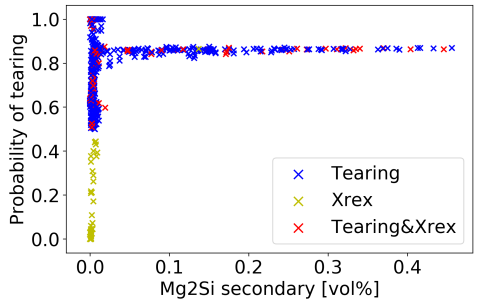

Figure 4.10: Effects of secondary Mg_2Si particles on tearing.

4.2 Grain Structure

This section will examine the PRO^{3TM} simulations that predict the microstructure as well as the experimental results from optical microscopy.

Simulation

The simulated recrystallization fraction as a function of the extrusion ram speed can be seen in Figures 4.11 to 4.14 for Hom. A samples. All Hom. B samples were completely recrystallized for all extrusion speeds according to simulations. As can be seen, the recrystallization fraction increases with ram speed, but the model collapses as the exit temperature approaches the melting temperature of the alloy. The figures are based on recrystallization fraction in the center of the profile, but the same trend in observed for the intermediate position and surface position as well. A complementary table of Alstruc results are found in Appendix A.

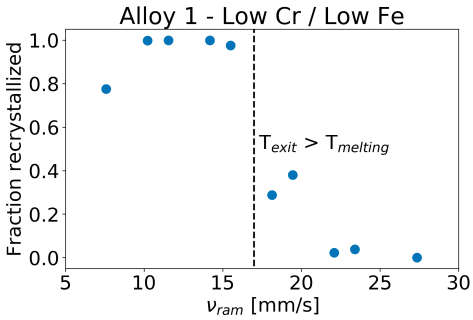

Figure 4.11: Recrystallization as a function of ram speed for sample 1A.

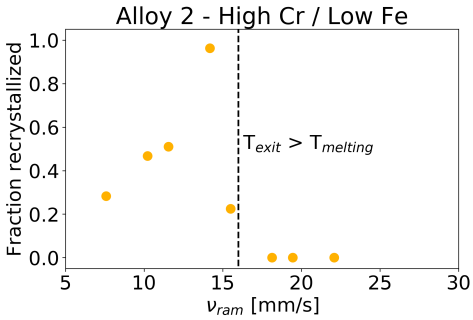

Figure 4.12: Recrystallization as a function of ram speed for sample 2A.

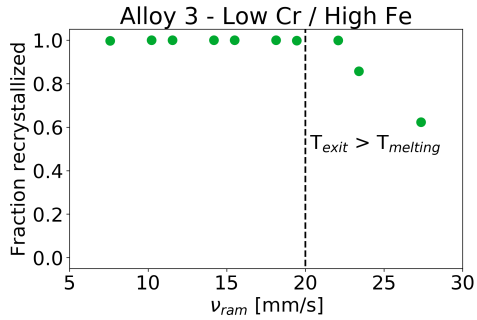

Figure 4.13: Recrystallization as a function of ram speed for sample 3A.

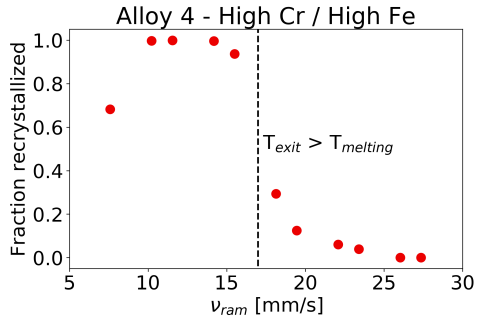

Figure 4.14: Recrystallization as a function of ram speed for sample 4A.

The simulated mean size of grains after recrystallization as a function of extrusion ram speed is plotted in Figures 4.15 and 4.16.

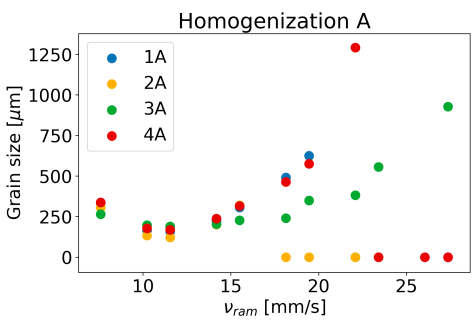

Figure 4.15: Grain size as a function of ram speed for Hom. A samples.

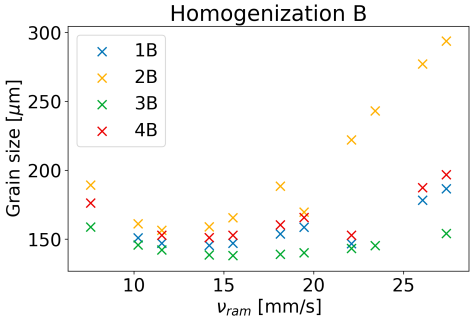

Figure 4.16: Grain size as a function of ram speed for Hom. B samples.

Experimental

Each extruded profile can be separated into three different samples. Table 4.2 assigns each number to its respective section of the profile. A conscious effort was made to extract samples representative of steady state extrusion.

Table 4.2: Section number corresponding to section of the extruded profile.

Number	Section
(1)	Lower Speed - Water Quenching
(2)	Higher Speed - Water Quenching
(3)	Higher Speed - Air Cooling

Figures 4.17 to 4.24 on the following page shows the microstructure as seen in optical microscope of the three sections of each alloy and homogenization type.

Alloy 1 (LCr/LFe): This alloy is low on chromium and iron. From Figures 4.17 and 4.21, it can be see that all sections are fully or mostly recrystallized, perhaps except for some areas in 1B at low speed and water quenching. Variation A exhibits smaller grains than B.

Alloy 2 (HCr/LFe): This alloy has high levels of chromium and a low iron concentration. From the figures 4.18 and 4.22 I can be see that the water quenched sections are mostly or fully fibrous. The air cooled section has very large grains. Also here, it is indicated that variation A has smaller grains than B.

Alloy 3 (LCr/HFe): This alloy has a low iron concentration and high levels of iron. Yet we still see fibrous segments of the water quenched section of 3B. The grain sizes are in the intermediate range.

Alloy 4 (HCr/HFe): This alloy has both high levels of chromium and iron. The water quenched sections are mostly or fully fibrous, while only segments of 4B is fibrous. Very large grains exist in the recrystallized segments.

Low Cr/Low Fe 585/1

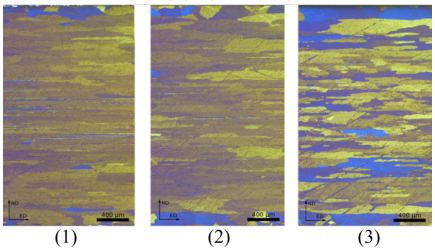

(1) (2) (3)

Figure 4.17: Extruded alloy 1A.

Low Cr/Low Fe 555/6

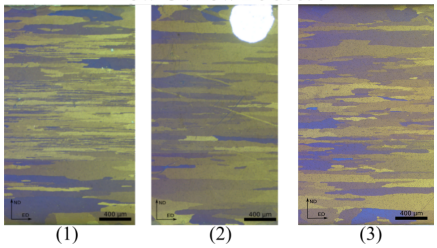

(1) (2) (3)

Figure 4.21: Extruded alloy 1B.

High Cr/Low Fe 585/1

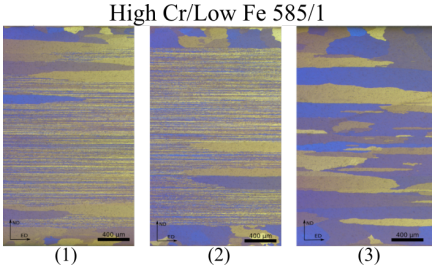

(1) (2) (3)

Figure 4.18: Extruded alloy 2A.

High Cr/Low Fe 555/6

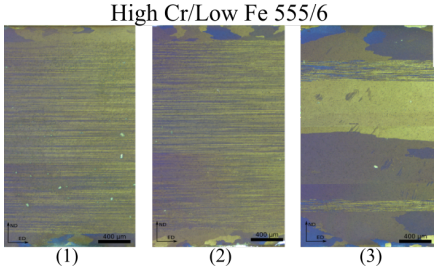

(1) (2) (3)

Figure 4.22: Extruded alloy 2B.

Low Cr/High Fe 585/1

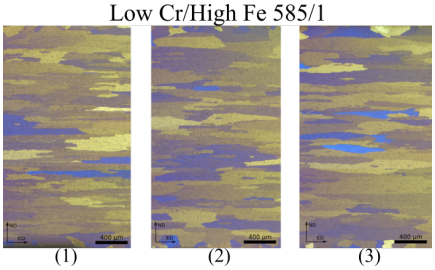

(1) (2) (3)

Figure 4.19: Extruded alloy 3A.

Low Cr/High Fe 555/6

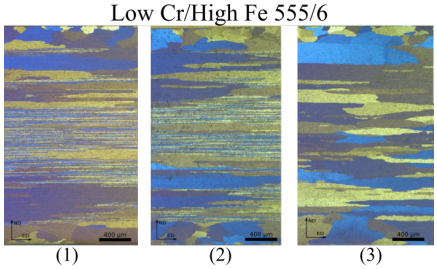

(1) (2) (3)

Figure 4.23: Extruded alloy 3B.

High Cr/High Fe 585/1

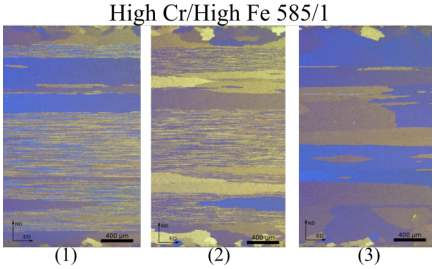

(1) (2) (3)

Figure 4.20: Extruded alloy 4A.

High Cr/High Fe 555/6

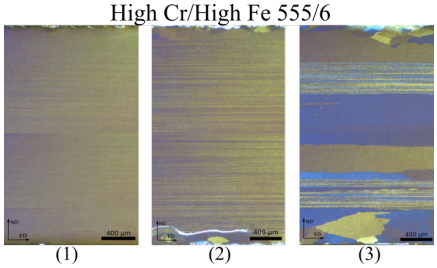

(1) (2) (3)

Figure 4.24: Extruded alloy 4B.

Comparison

Table 4.3 shows the viability matrix of each alloy when accounting for recrystallization, both from experimental and simulated results. The green check marks (✓) are fibrous microstructures, the red crosses represent (✗) represent recrystallized alloys, while the yellow question marks (?) are partly recrystallized. Alloys which have exceeded the solidus temperature during extrusion are assigned ”liq.” for partly melted.

Table 4.3: Microstructure viability matrix comparing experimental and simulated results.

Sample	**(1)**		**(2)**	
	Expr.	Sim.	Expr.	Sim.
1A	✗	liq.	✗	liq.
2A	✓	liq.	✓	liq.
3A	✗	?	✗	liq.
4A	✓	liq.	✓	liq.
1B	✗	✗	✗	?
2B	✓	✗	✓	liq.
3B	?	✗	?	✗
4B	✓	?	✓	liq.

Due to an overestimation in deformation temperature, PRO^{3TM} suggests that almost all experimental alloys are subjected to melting during extrusion. This makes the comparison difficult. Out of the non-melted alloys, only 1B is correctly predicted as recrystallized (12.5 %). Four out of eight of the predictions are undecided (50 %), while three out of eight are wrong (37.5 %).

The grain size was not measured experimentally, but qualitatively, it can be seen that the grain size increases towards the middle of the profile. This trend is also seen in PRO^{3TM}. Furthermore, fibrous alloys were predicted to have the largest grains at the surface. Qualitatively this also appears to be true. Anecdotally, alloy 3A has larger grains than 3B, which is the only result which can be compared between experimental and simulations.

4.3 Dispersoids

This section will examine the results from the parameter study in PRO^{3TM}, as well as the results from Scanning Electron Microscopy (SEM), concerning the presence of dispersoids in each sample. This section will present the calculated size distributions, number densities and volume fractions. The experimental results will be compared to the PRO^{3TM} results.

Simulation

Figures 4.25 and 4.26 show the effects of chromium and iron on the dispersoid number density respectively, as simulated by PRO^{3TM}. Evidently, the number density increases with increasing chromium conent, and decreases with increasing iron conent.

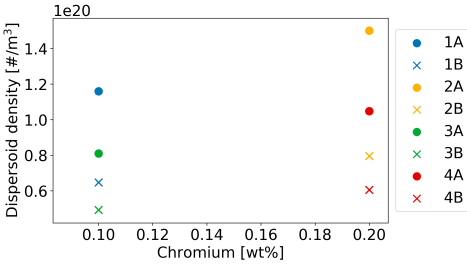

Figure 4.25: Chromium's effect on dispersoid density.

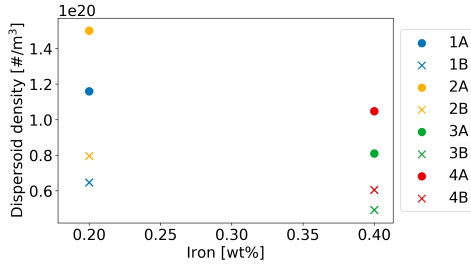

Figure 4.26: Iron's effect on dispersoid density.

From Figures 4.27 and 4.28 the effects of homogenization treatment and extrusion ram speed on the dispersoid number density respectively, as simulated by PRO^{3TM}. Evidently, the number density of dispersoids is higher after Hom. A compared to Hom. B, and is unaffected by the extrusion ram speed.

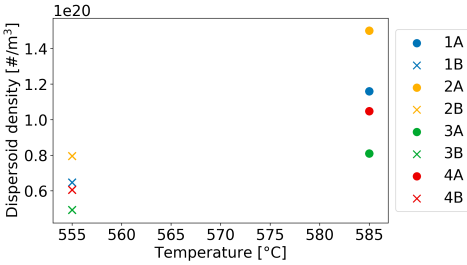

Figure 4.27: Homogenizaiton's effect on dispersoid density.

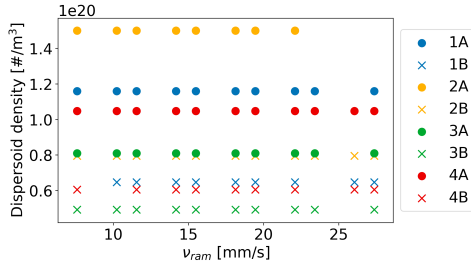

Figure 4.28: Ram speed's effect on dispersoid density.

Experimental

Figures 4.29 and 4.30 show the particle size distribution of dispersoids in the range from 50 to 350 nanometers for Hom. A and Hom. B samples respectively. More illustrations of the experimental dispersoid measurements can be found in Appendix B.1.

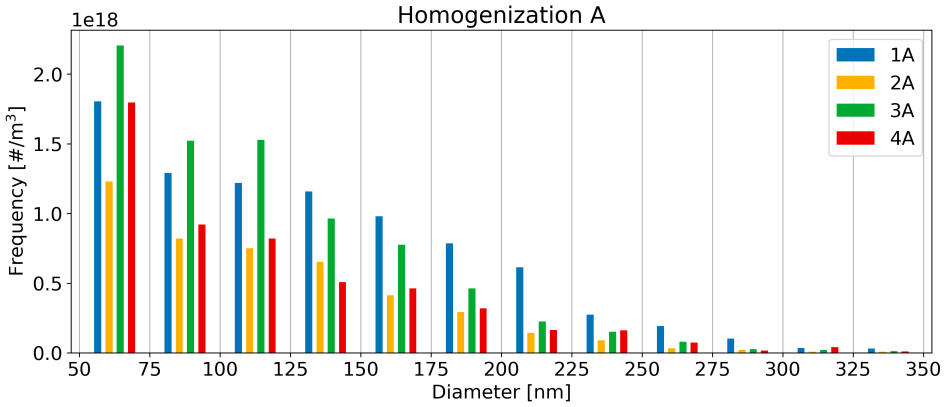

Figure 4.29: Particle size distribution in Hom. A samples.

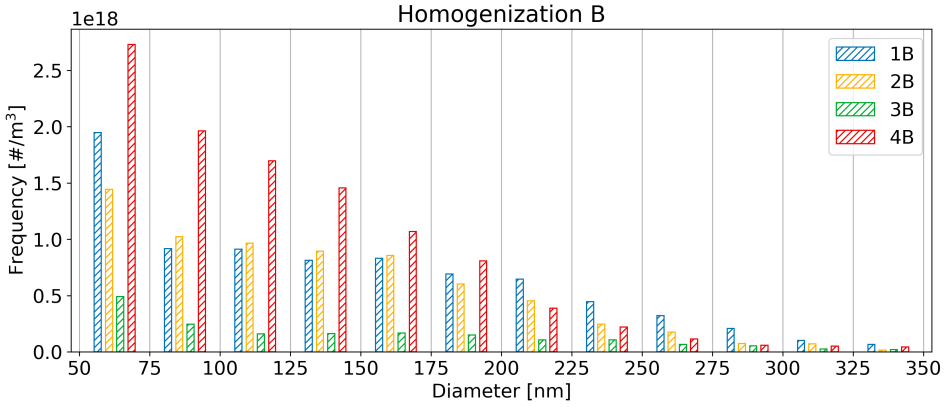

Figure 4.30: Particle size distribution in Hom. B samples.

Comparison

In Figures 4.31 and 4.32, the number density and volume fraction of dispersoids is compared between simulation and measurements. The full-bodied bars represent the Hom. A alloys as measured experimentally, while the diagonally lined bars represent the Hom. B alloys as measured. The dotted full-bodied bars represent Hom. A as simulated by Alstruc, and the dotted blank bars represent Hom. B as simulated. As can be seen in the aforementioned graph, there is a factor of 10 in difference between measurements and simulation in this case.

An independent dispersoid particle analysis was performed at Hydro Sunndalsøra and can be found in Appendix B.3. These measurements differ significantly from the results in this thesis. However, the independent measurements are more closely related to the experimental results compared to Alstruc results.

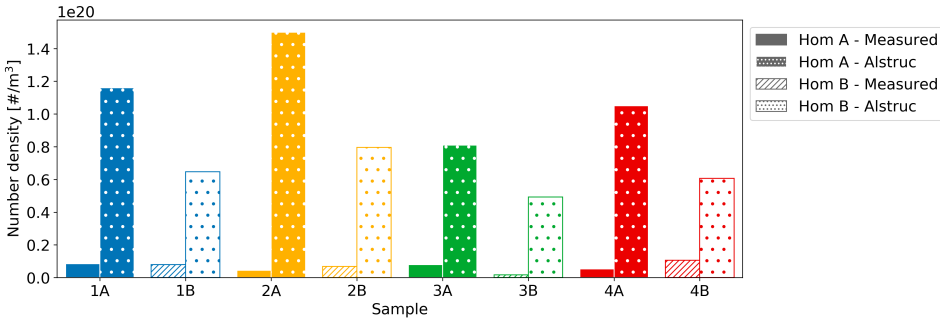

Figure 4.31: Comparison of measured and simulated number density of dispersoids in each sample.

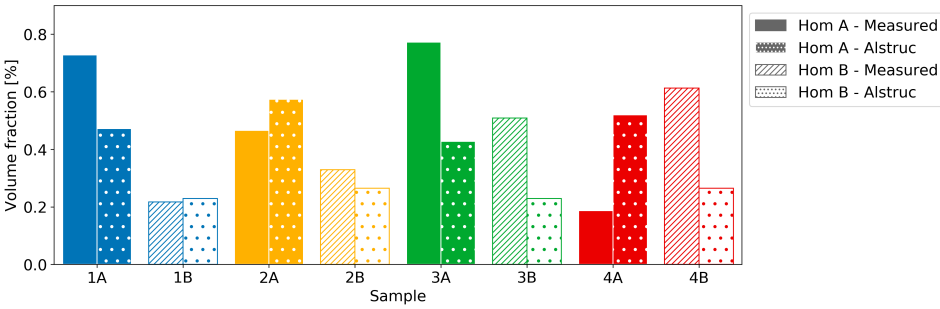

Figure 4.32: Comparison of measured and simulated volume fraction of dispersoids in each sample.

Figure 4.33 shows the comparison between mean particle radius from measurements and Alstruc. Figure 4.34 shows the comparison between simulated Zener drag and calculated Zener drag. Calculations are based on eq. 2.11 and measured dispersoid data. Note that the Zener drag is dependent on the mean radius.

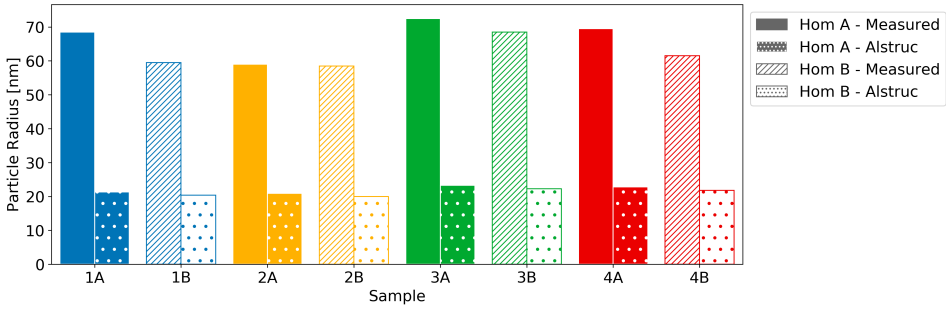

Figure 4.33: Comparisons of mean radius of dispersoids in each sample.

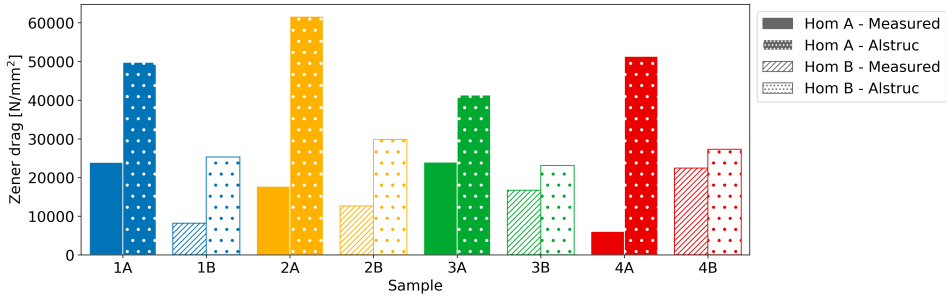

Figure 4.34: Comparison of Zener drag of each sample.

4.4 Tearing

In this section, the failure mechanism known as tearing will be discussed. First, the PRO^{3TM} simulation results will be presented, followed by the discovery of tearing in the experimentally tested alloys.

Simulation: The tearing as a function of deformation temperature can be seen in Figure 4.35. It appears that the tearing is only dependent on deformation temperature in these alloys.

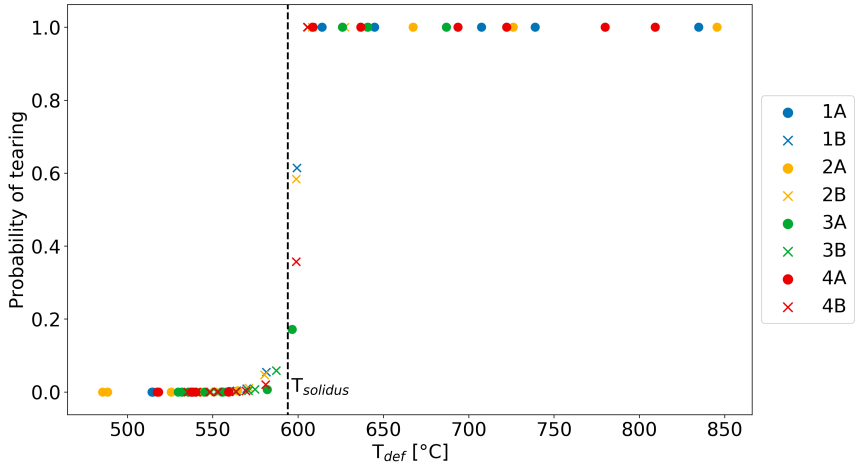

Figure 4.35: Tearing as a function of deformation temperature.

As can be seen in Figures 4.36 and 4.37, the deformation temperature depends on the extrusion ram speed as well as the deformation resistance.

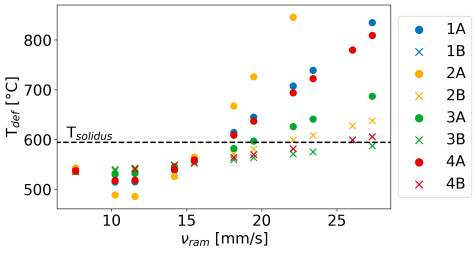

Figure 4.36: Extrusion ram speed's effect on deformation temperature.

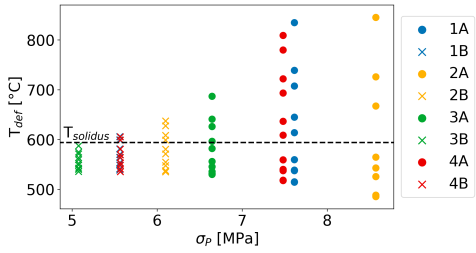

Figure 4.37: Deformation resistance's effect on deformation temperature.

Figures 4.38 to 4.45 on the next page show each alloy's susceptibility towards tearing with increasing extrusion ram speed as predicted by PRO^{3TM}.

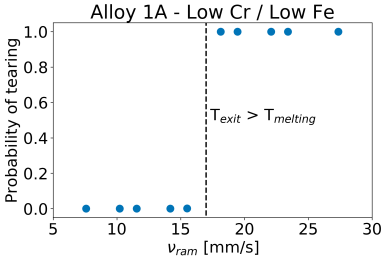

Figure 4.38: Tearing in alloy 1A.

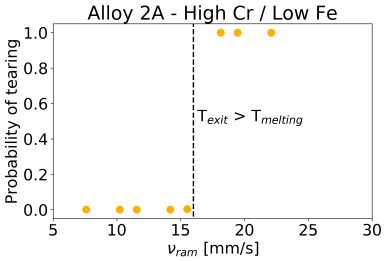

Figure 4.39: Tearing in alloy 2A.

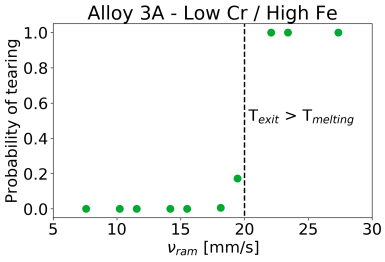

Figure 4.40: Tearing in alloy 3A.

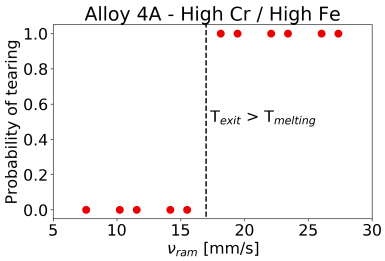

Figure 4.41: Tearing in alloy 4A.

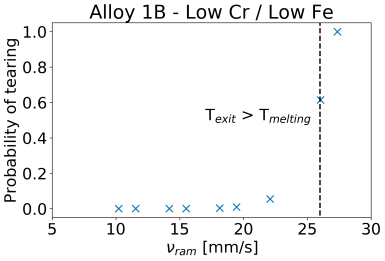

Figure 4.42: Tearing in alloy 1B.

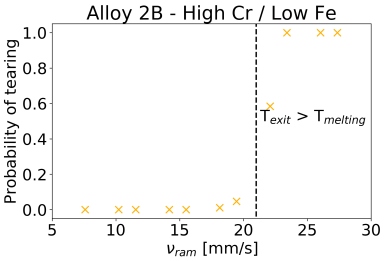

Figure 4.43: Tearing in alloy 2B.

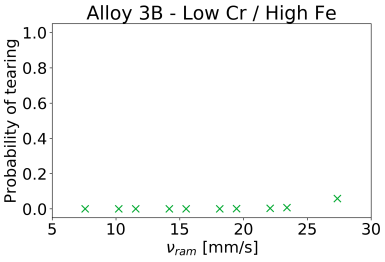

Figure 4.44: Tearing in alloy 3B.

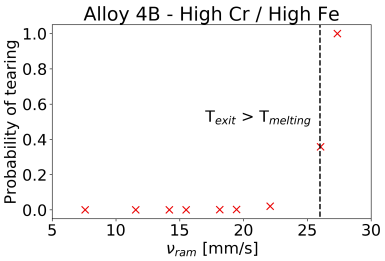

Figure 4.45: Tearing in alloy 4B.

Experimental: It was initially thought that tearing was observed in most, if not all of the extruded profiles. However, upon closer inspection it may appear that these imperfections were caused by a worn extrusion die. The appearance of the surface defects were consistent across all profiles, and during inspection in optical microscopy, no tearing was found in the view plane except for alloys 4A and 4B, in section 1 and 2 for both samples as can be seen from Figure 4.46. Some indication of smaller tearing may have been present in alloy 3A section 2 as suggested in Figure 4.47. It is important to note that Alloy 4 was extruded at higher speeds than Alloys 1, 2 and 3. The black spots in the images are pores which stem from anodization.

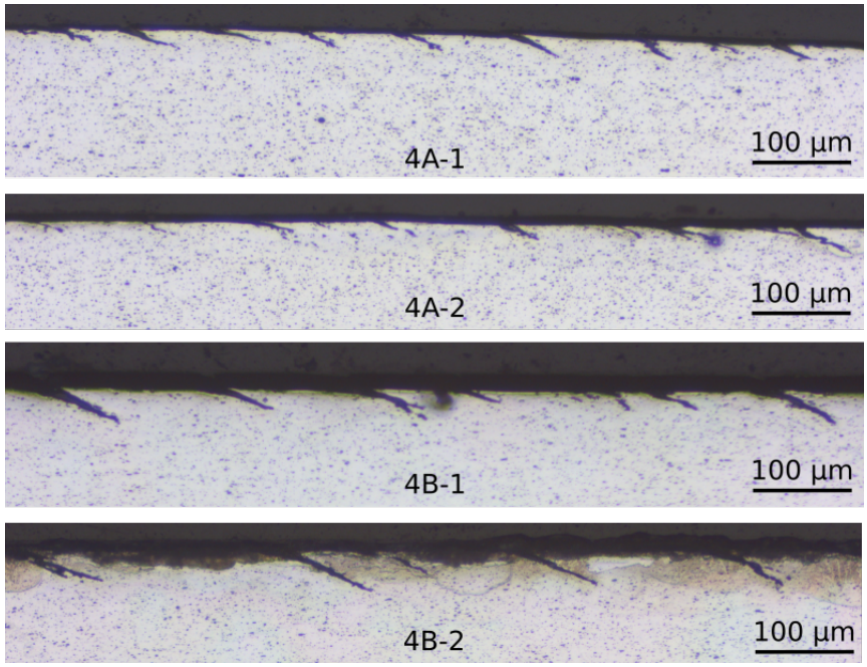

Figure 4.46: Tearing observed in alloy 4 using optical microscopy.

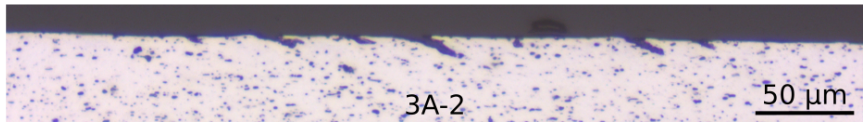

Figure 4.47: Indication of smaller tearing in sample 3A, section 2.

A phenomena known as spooling was thought to be observed in the profile, however, due to the consistency of the imprints on the profile throughout all parallels, it was decided that the defects came from a worn extrusion die.

Comparison

Table 4.4 shows the viability matrix of each alloy when accounting for tearing, both from experimental and simulated results. The green check marks (✓) are low probability of tearing, the red crosses represent (✗) represent high probability, while the yellow question marks (?) are considered some risk of tearing.

Table 4.4: Tearing viability matrix comparing experimental and simulated results.

Sample	**(1)**		**(2)**	
	Expr.	Sim.	Expr.	Sim.
1A	✓	✗	✓	✗
2A	✓	✗	✓	✗
3A	✓	✓	?	✗
4A	✗	✗	✗	✗
1B	✓	✓	✓	?
2B	✓	✓	✓	✗
3B	?	✓	✓	✓
4B	✗	?	✗	✗

The information in the table above suggests that PRO$^{3\text{TM}}$ correctly predicts the presence of tearing in each alloy in 7 out of 16 cases (44 %). 4 of 16 cases are undecided (25 %), while 5 out of 16 cases are incorrect (31 %).

4.5 Hardness Testing

Figures 4.48 to 4.55 show the Vicker hardness for each extruded section of all samples.

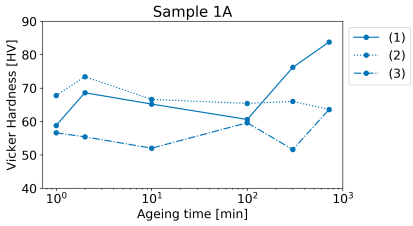

Figure 4.48: Vickers hardness for sample 1A.

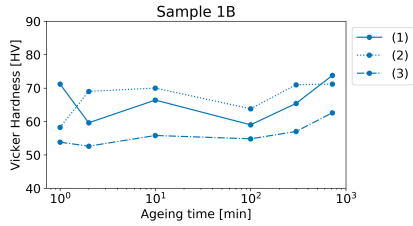

Figure 4.52: Vickers hardness for sample 1B.

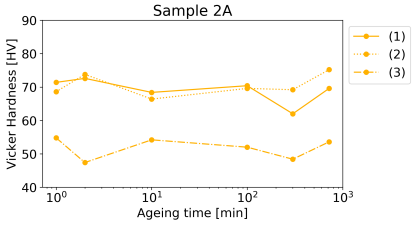

Figure 4.49: Vickers hardness for sample 2A.

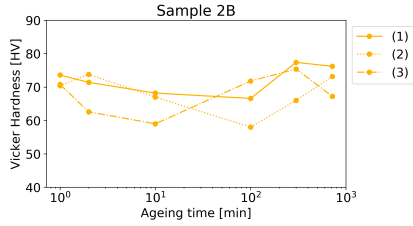

Figure 4.53: Vickers hardness for sample 2B.

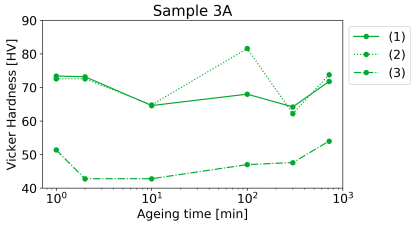

Figure 4.50: Vickers hardness for sample 3A.

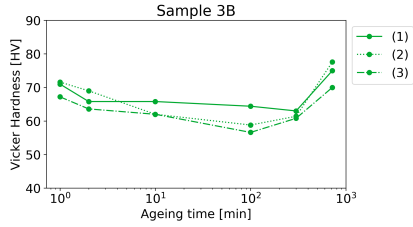

Figure 4.54: Vickers hardness for sample 3B.

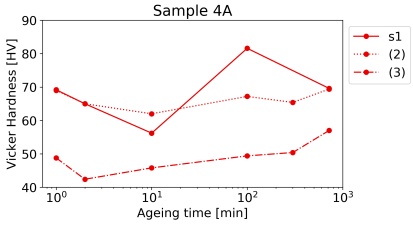

Figure 4.51: Vickers hardness for sample 4A.

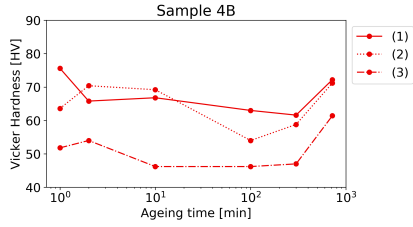

Figure 4.55: Vickers hardness for sample 4B.

4.6 Electrical Conductivity

Electrical conductivity was measured in the extrusion plane of all samples. All samples had been artificially aged for 5 hours, and was assumed to have reached peak hardness (T6). The room temperature was 25 °C during conductivity measurements. Each data point is the average of three measurements. Results can be seen in Figure 4.56. It becomes clear that Hom. B alloys have a higher electrical conductivity than their respective Hom. A alloys. Moreover, additional chromium or iron both seem to be detrimental to the electrical conductivity.

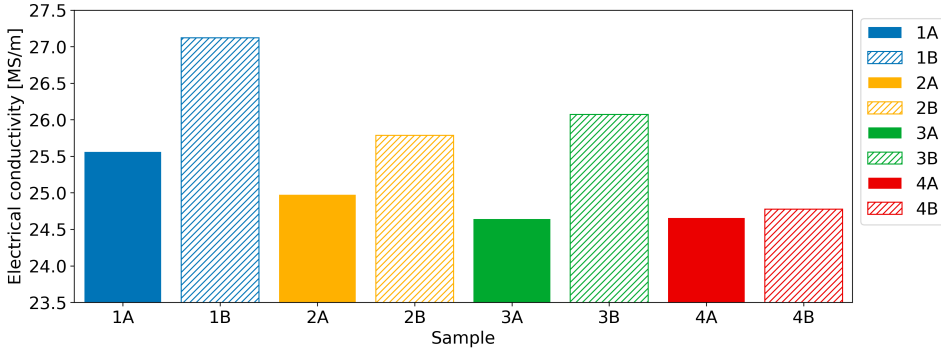

Figure 4.56: Measured electrical conductivity in all samples.

Chapter 5

Discussion

In this section, the results presented in Section 4 will be discussed. Results will be compared to the expected results given the theoretical background in Section 2, and observed deviation from the expected results must be justified.

The experimental work in this thesis was conducted with little to no previous experience in experimental metallography, optical microscopy and SEM, and with only brief guidance from engineers. As such, reservations are made against errors of this nature.

5.1 Importance

This thesis is an extension of the work conducted for the specialization project during the fall of 2018. Here, over 1,500 unique alloys were simulated over the course of one week. This represents an unparalleled level of productivity compared to the experimental approach, and the incorporation of machine learning allows each new alloy to be designed more intelligently than the previous one. Of great importance is also the ability to perform digital experiments at low cost and with negligible impact on the environment. The business minded advantage of having a tool such as PRO$^{3\text{TM}}$ when your competitors do not, is perhaps the greatest economical incentive for the investments into this project.

It has already been established that PRO$^{3\text{TM}}$ struggles with the effects of chromium, and that only empirical models are used to predict the impact of this alloying element. The results of this thesis will aid in the development and calibration of the software, especially regarding these weak points. The importance of aluminium as a replacement material for steel, which is more polluting, for high volume applications such as structural components in constructions has already been emphasised.

5.2 Alloy Design

The alloys chosen as a basis for the work in this thesis was based on the simulations performed during the fall of 2018. The alloys lie near the Pareto front for highest tensile

strength and highest extrusion ram speed and are similar in chemical composition as existing products. For this thesis, the effects of chromium and iron, as well as homogenization treatment have been investigated. A notable reservation to make is that the alloy design is based on the extrusion with a rectangular hollow die, while the experimental alloys were extruded with a flat rail profile. How this may affect the quality of the results are not well known.

One cause of great uncertainty is whether or not samples were extracted from the intended sections of the extruded profile. None of the results have yielded reassuring evidence that sections 1 and 2 stem from material extruded at different speeds. The expected difference between 20 mm/s and 26 mm/s or 26 mm/s and 30 mm/s is not well known. Following this, the effects of extrusion ram speed will not be emphasised in this chapter.

5.3 Microstructure

In this section, the microstructure of each sample will be discussed. This includes grain structure, dispersoids and tearing. The PRO^{3TM} simulations will also be discussed alongside their respective real-world counterpart.

5.3.1 Grain Structure

In this subsection, the grain structure, as seen in optical microscopy will be discussed. This includes the experimental conditions under which testing was conducted, results in comparison with PRO^{3TM} predictions, the effects of chemical composition, homogenization, extrusion speed in each alloy.

Experimental Conditions

The experimental conditions of the work with optical microscopy is deemed good. Sample 1A-(3) has an uneven and scratched surface, which stems from a hasty preparation by hand, compared to the other samples which were machine polished. Sample 1B-2 shows a bright white spot, which is believed to be white fibres which stem form a cotton swab. In this discussion, it has been assumed that the small cross-sections of the extruded profiles that has been investigated are representative for the whole extruded section. This is not necessarily a good assumption, especially in samples with large grains. As have been mentioned earlier, large grains are often the result of a abrupt growth in a fibrous structure, which may give a local variance in grain size. Some noticeable difference in contrast and general quality can be seen in different images. The images were taken over several sessions, where other students used the microscopes in between. The exact settings and light sensitivity is hard to replicate each time.

Comparison to PRO^{3TM}

For the homogenization A alloys, Alloy 1, 2 and 4 are predicted to be completely fibrous. However, on closer inspection, it is realized that all of these samples exceed the

solidus temperature during extrusion. At the highest extrusion speed, 26 mm/s, the metamodel predicts that alloys are mostly liquid after extrusion, which causes the model to collapse. The returned values are completely nonsensical in this temperature range. These results should be discarded entirely. The difference between simulated and experimental deformation temperature may be accounted for by the difference in number density of dispersoids. As can be seen in Figure 4.31, Alstruc returns a significantly higher number density compared to the measured values, which in turn would cause a much higher deformation resistance, and thus higher deformation temperature. An important note is that the metamodel was constructed with σ_p values ranging from 0.8 to 2.6, while the simulated alloys in PRO^{3TM} exhibit σ_p values from 5.0 to 8.5. This is well outside the range of the metamodel, and the metamodel could collapse completely in this range.

According to Alsoft predictions, all homogenization B alloys fully recrystallize for all extrusion ram speeds between 7 mm/s to 27 mm/s. As will be discussed later, predictions also show also that Hom. B alloys systematically have a lower number density of dispersoids compared to their associated Hom. A alloys. This in turn would make Hom. B alloys in simulations more prone to recrystallization, as is reflected in the PRO^{3TM} data set. However, neither the degree of recrystallization, nor the number density of dispersoids are reflected in the experimental results. As can be seen in the micrographs, both Alloys 2B and 4B, and to some extent 3B display fibrous microstructures. As can be seen by Figure 5.1, samples 2B and 4B have a *higher* number density compared to 2A and 4A respectively. The combination of a higher predicted deformation temperature compared to the real deformation temperature, as well as suggesting that 2B/4B alloys have lower density of dispersoids compared to 2A/4A could have caused PRO^{3TM} to wrongfully predict recrystallization in these alloys.

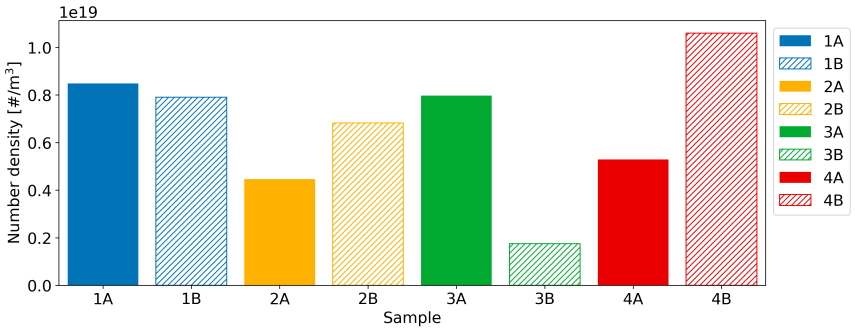

Figure 5.1: Measured dispersoid number density for all samples.

PRO^{3TM} predicts that the recrystallized grains decrease in size the closer they are to the surface of the extruded profile, as can be seen by Figure 5.2, which shows the Hom. B samples. By examining the micrographs, this seems qualitatively correct.

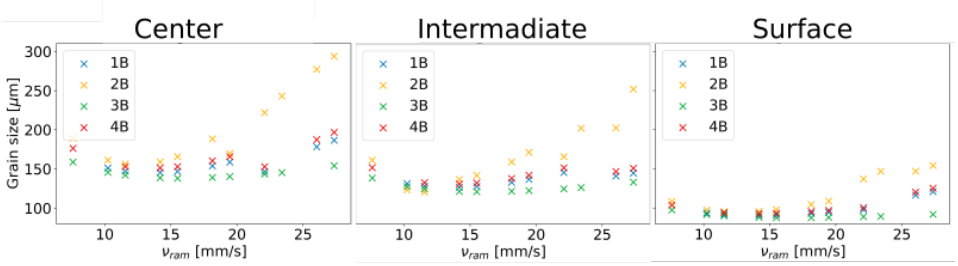

Figure 5.2: PRO^{3TM} predicted grain size for each position for Hom. B samples.

Effects of Homogenization

By comparing the microstructures of all samples (as seen in Figures 4.17 to 4.24), it can be said that generally, the Hom. B is less recrystallized than Hom. A. It would be expected that Hom. B alloys have fewer and larger dispersoids than their Hom. A equivalents, due to the coarsening and dissolution of dispersoids during longer homogenization treatments. This suggests that Hom. B would be more recrystallized than Hom. A, however this is not the observed case. The reasoning will be discussed in Section 5.3.2 about dispersoids.

Effects of Chromium and Iron

It is expected that chromium, as a dispersoid-forming element, affects the recrystallization process of the alloy. More chromium should in theory translate to less recrystallization. From the Figure 4.17 to 4.24, it is fair to say that Alloys 2 and 4 are less recrystallized than Alloys 1 and 3 respectively, for both homogenization types. This suggests that chromium does indeed form dispersoids which inhibit recrystallization. High chromium alloys, Alloy 2 and 4, also exhibit larger recrystallized grains than their low chromium counterparts, Alloy 1 and 3 respectively. This further suggests that the alloys that are intended to be resistant to recrystallization, will grow very large recrystallized grains when recrystallization is first initiated. Furthermore, it is expected that iron affects the density of dispersoids, as iron-bearing phases can soak up dispersoid-forming elements such as chromium and manganese from solid solution. By comparing Alloy 4 with Alloy 2 and Alloy 3 with Alloy 1, it is indicated that perhaps the opposite is true. This will also be discussed in Section 5.3.2.

Effects of Cooling After Extrusion

The evident effect of cooling rates after extrusion is that the water quenching generally yields less recrystallized material. The rapid cooling from deformation temperature to room temperatures prevents recrystallization, as the nucleation and growth of recrystal-

lized grains happens predominantly at higher temperatures. This is exemplified by Alloys 2A/B and 4A/B.

5.3.2 Dispersoids

In this subsection, the observations made in SEM regarding dispersoids will be discussed. This includes the experimental conditions under which testing was conducted, results in comparison with PRO^{3TM} predictions, the effects of homogenization, chemical composition, cooling rates after extrusion, and its impact on the recrystallization in each alloy.

Experimental Conditions

The dispersoids were measured using a scanning electron microscope, at x5000 magnitude using QBSE (quantitative back-scattered electron) signal. The resolution of the images are 22 nanometers per pixel. This means that the lowest particle that can be measured is approximately 2x2 or 3x3 pixels, which translates to 44 to 66 nm diameter particles, assuming the image quality is impeccable. This represents a very important uncertainty in regards to the accuracy of the measurements in SEM, as will be discussed in the comparison to PRO^{3TM}. The SEM voltage was set to 15 kV, which may cause the electrons to back-scatter against subsurface particles as well as the surface particles, which in turn causes particles to be seen which shouldn't have been. This causes an artificial increase in the observed number density of dispersoids. The samples were prepared without much underlying knowledge, and some fundamental errors could have occurred.

An independent measurement of the dispersoid density of samples 3B and 4B has been done at Hydro Sunndalsøra. A summary of the results can be found in Appendix B.3. The measurements yielded a significant difference compared to the results of this thesis. 3B was measured in Sunndalsøra to have approximately 2 times *more* dispersoids per square millimeter (#/mm^2) compared to the thesis' results, while 4B was measured in Sunndalsøra to have 1.7 times *less* dispersoids per square millimeter (#/mm^2). Some of the discrepancy can be accounted for with the difference in voltage. At Hydro Sunndalsøra, a voltage of 4.0 kV and a working distance of 7.7 mm, which would display less subsurface dispersoids. Furthermore, it's fair to assume that these samples have been better prepared, and the image processing have separated the particles from the matrix to a larger extent than what has been done in this thesis. The measurements from Hydro Sunndalsøra does however suggest that the dispersoid density in sample 3B surpasses that of 4B, which is completely contrary to what both the theoretical background and the grain structures may suggest.

For discussion purposes, it will be assumed that the measurements are representative in the remainder of this section.

Comparison to PRO^{3TM}

Alstruc calculates the mean radius of the dispersoids to be between 20 and 25 nm for all samples. As just discussed, the absolute minimum size that can be observed from SEM images is 22 nm radius particles (2x2 pixels), and these are measured with significant

uncertainty. If Alstruc is correct, more than half of all dispersoids are below the threshold for what can be observed. The propagation of this effect is that the measured number density of dispersoids is significantly smaller than the actual density. This can be clearly seen in Figure 4.31. This effect also propagates to the calculation of Zener drag, which will be discussed later.

Let's assume for a moment that for dispersoids in the range of 50 to 350 nm, Alstruc simulations compared to the measurements are similar. Furthermore, let's assume that the Alstruc calculations of small dispersoids are also reasonable, and that there are in fact bountiful amounts of dispersoids in the range of 0 to 50 nm which have not been measured experimentally. Let's justify these assumptions.

The comparison of volume fractions of dispersoids between PRO^{3TM} and measurements from Figure 4.32 is within feasible margins. It can be speculated that due to the low volume of each of the smallest dispersoids, it's can be assumed that these will not affect the volume fraction. In Figure 5.3, the volume weighted particle distribution of all samples have been plotted, and indeed the contribution of particles in the range of 50 to 75 nm is no more than 3 % of the total volume of dispersoids for every sample.

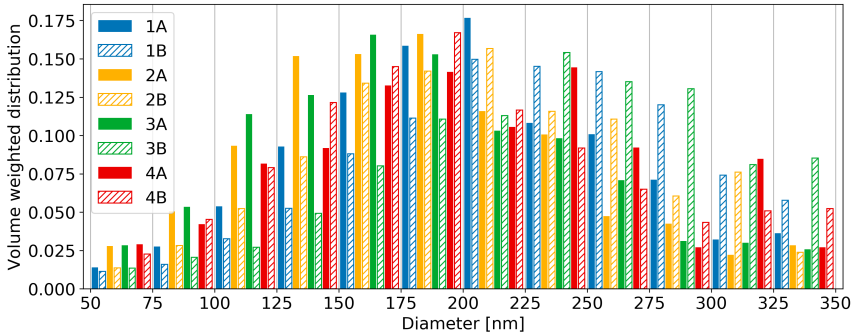

Figure 5.3: Volume weighted distribution of all alloys.

Extrapolating on this data, there are reasons to believe that the particles in the 0 to 50 nm range will contribute even less. If these dispersoids can be neglected mathematically in the volume fraction simulations, as they have been neglected in the experimental measuring of the volume fraction due to their small size, it must be true that the dispersoids in the range 50 to 350 nm is of similar number density and size distribution in both simulation and real world. Let's consider the second assumption in the following paragraph.

Zener drag

From Figure 4.34, there appears to be a large gap between Alstruc values and measured values. The Zener drag is proportional to the volume fraction of dispersoids, and inversely proportional with the mean radius of dispersoids. Due to the effect of the latter, there are reasons to believe that if smaller than 50 nm dispersoids does indeed exist, and could be measured (which in turn would have lowered the measured mean size of the dispersoids), the measured Zener drag would have been much closer to the simulated value.

As can be seen in Figures 5.4 and 5.5, if the mean size of measured dispersoids is reduced by a factor of 3 such that the PRO^{3TM} simulations and the measurements coincide better (which in practise means adding a large amount of sub 50 nm particles to the calculations), the comparison of Zener drag increases significantly in quality. Not only this, but the adjusted values for Zener drag seems more reasonable compared the raw Zener drag values, according to previous experience. This may suggest that if there are in fact a significant number of unmeasured, small dispersoids, the measured Zener drag is in a more reasonable range, and that simulations and calculations are much more accurate that the results initially suggests.

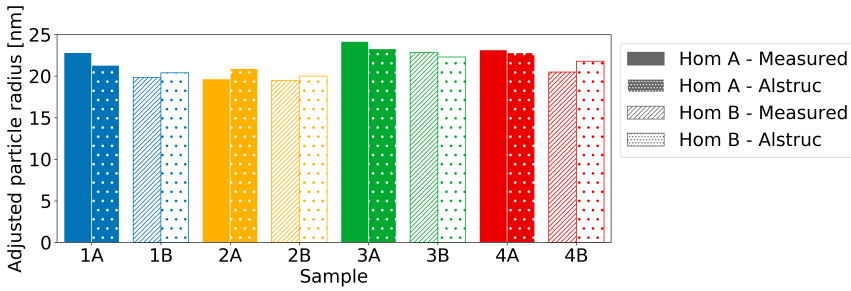

Figure 5.4: Adjusted mean particle size values.

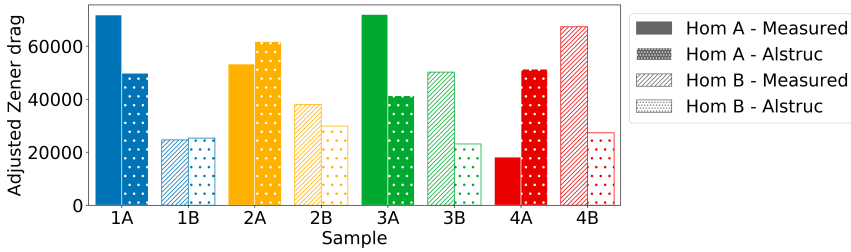

Figure 5.5: Adjusted Zener drag values.

Effects of Homogenization

Alstruc predicts that for all alloys (1 through 4), Hom. A will always yield a higher number density of dispersoids compared to Hom. B for alloys of identical chemical composition. This is expected due to the dissolution of small dispersoids and coarsening of larger dispersoids during long homogenization treatments, which Hom. B represents. When the homogenization time is short, there is only time for the dispersoids to nucleate, not grow, dissolve or fuse together. However, this has only been observed for low chromium alloys (Alloy 1 and 3). For high chromium alloys (Alloy 2 and 4), Hom. B yields a higher number density compared to Hom. A. This was illustrated in Figure 5.1. As to why this may be, is explained in the ”Effects of Chromium and Iron” subsection.

One observation which was expected, is the pronounced shift towards larger dispersoids in Hom. B alloys. This can be seen clearly in the area weighted plots in Figures 5.6 to 5.8 (larger figures are also found in Appendix B.1). The dotted line, which represents the particle size distribution of Hom. B alloys, is clearly shifted towards the right, compared to the solid line, which represents Hom. A alloys. The effect is not as pronounced in Alloy 4 (Figure 5.9. As stated previously, longer exposure to high temperatures will cause dispersoids to grow larger over time, while the smaller dispersoids may dissolve completely. In the short exposure time of Hom. A, dispersoids may nucleate, but not grow.

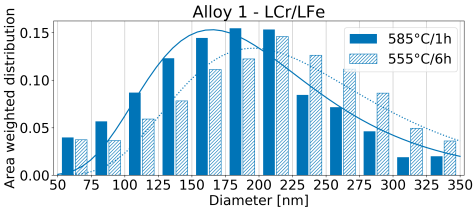

Figure 5.6: Alloy 1A/B dispersoid distribution.

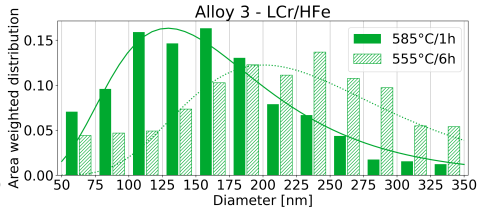

Figure 5.8: Alloy 3A/B dispersoid distribution.

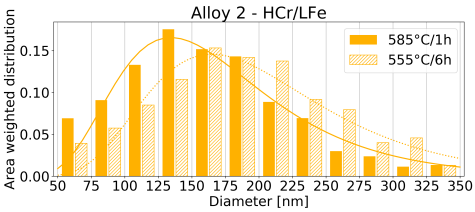

Figure 5.7: Alloy 2A/B dispersoid distribution.

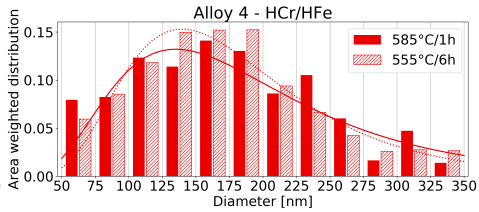

Figure 5.9: Alloy 4A/B dispersoid distribution.

Effects of Chromium and Iron

As has been discussed earlier, it would be expected that chromium increases the number density of dispersoids, while iron decreases the number density. By extension, it would be expected that the dispersoid density would decrease in the order given by Table 5.1, and that Hom. A would yield a higher number density than Hom. B, which was discussed in the previous paragraphs.

Table 5.1: The expected order of decreasing dispersoid density by alloy.

$$2 \quad > \quad 4 \quad > \quad 1 \quad > \quad 3$$

However, the measured order of decreasing dispersoid density does not resemble the expected order. The complex nature of dispersoids makes it hard to justify exactly why the measurements deviates from the expected results. Chromium dispersoids, such as α-Al(CrMn)Si, are known to nucleate at the interface of β-AlFeSi [36], which suggests that

more iron translates to more nucleation sites for the dispersoid particles. When homogenized for additional time, the β-AlFeSi eventually dissolves, while α-Al(CrFe)Si particles grow. This may explain why high chromium alloys (Alloy 2 and 4) respond better to Hom. B than Hom. A, compared to the low chromium alloys (Alloy 1 and 3), as can be seen in Figures 5.10 and 5.11.

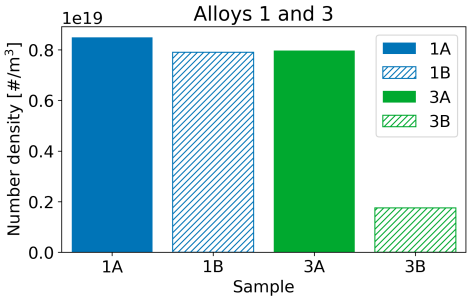

Figure 5.10: Measured number density in Alloys 1 and 3.

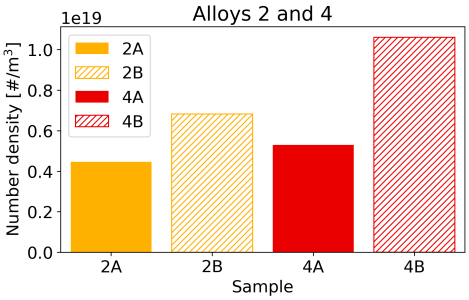

Figure 5.11: Measured number density in Alloys 2 and 4.

High chromium content allows many dispersoids to nucleate on iron-bearing phases, and the extended homogenization period allows them to grow, while dissolving any iron bearing phases which releases even more chromium and manganese into solid solution which can grow as dispersoids. In low chromium alloys, this phenomena does not appear to have an effect. The outcomes of Hom. B compared to Hom. A is more pronounced in in the high iron content samples (Alloys 3 and 4) compared to low iron content samples (Alloy 1 and 2). This further indicate the interaction between iron and chromium.

Effects of Cooling After Extrusion

It was assumed that the temperature of aluminium during extrusion would not affect the dispersoids in any significant way. This assumption is reasonable due to the short duration at which the alloys were at elevated temperatures. As a precautionary thought, the air cooled sections may have experienced some tiny alteration to its dispersoids, compared to the water quenched sections, due to the duration at which the materials was kept hot. This has not been taken into account during measurements and discussion. As previously mentioned, some of the samples examined in SEM may have been air cooled instead of water quenched.

Effects on Recrystallization

The dispersoids effect on recrystallization have been discussed at length in Section 2. The theory states that the number density is highly indicative of the recrystallization inhibition. However, both sample 1A, 1B and 3A have among the highest measured number densities of dispersoid particles, yet all are completely recrystallized. Furthermore, 2A, which has among the lowest densities are mostly fibrous, and 3B which has the lowest density, is not completely recrystallized. This may emphasise on the uncertainty of the

measurements more than anything. On the assumption that the dispersoids measurements are reasonable, the recrystallization may be attributed to the distribution of dispersoid particles. This was not measured, but an even distribution, with minimal inter-particle spacing is ideal for retarding recrystallization. Size of particles also matter. Two alloys can have the same volume fraction of dispersoids, but vastly different number density and sizes. Theoretically, a high volume fraction and very small mean particle size would result in the highest inhibition towards recrystallization. This in turn would pose other problems in regards to high deformation resistance and in turn deformation temperature which enables tearing. If anything, this shows that designing the best alloy is a subtle balance between many opposing factors.

5.3.3 Tearing

In this subsection, the observed tearing, or lack thereof, will be discussed. This includes the results in comparison with PRO^{3TM} predictions, the effects of extrusion speed and dispersoids.

Experimental Conditions

The surface of the extruded profiles were rugged and uneven. It was first thought that these imperfections were due to the high extrusion speed. However, after close examination of all samples, the imprints left in the profile must have come from a worn out extrusion die tool due to the consistency of the imprints across all profiles. During examination of the tearing in optical microscope, only the view plane was observed. This view plane represents a relatively small sample size, and further examination could be needed.

Comparison to PRO^{3TM}

As PRO^{3TM} suggest that the Mg_2Si particles are kept to a minimum for all alloys, tearing comes down to the comparison between deformation temperature and solidus temperature. PRO^{3TM} suggests that Alloys 1A, 2A, 4A and to some extent 3A experience tearing when extruded at the experimental speeds, 20-26-30 mm/s. As has already been discussed in the "Comparison to PRO^{3TM}" under "Grain Structure", the deformation temperature of Hom. A alloys is overestimated during simulations. As discussed, this could be due to the overestimation of dispersoids which in turn cause an overestimation of deformation resistance. As mentioned, the metamodel was not constructed with such high deformation resistance in mind.

Effects of Dispersoids

Alloys 4B and 3A have among the highest number density of dispersoids of all the samples as measured in SEM. These dispersoids contribute to the deformation resistance in the alloy, which in turn increases the deformation temperature and the probability of tearing. If PRO^{3TM} simulations are to be believed, there are no significant levels of Mg_2Si particles in any of the alloys, which otherwise would increase the risk of tearing significantly. When neglecting for Mg_2Si particles, the solidus temperature should be approximately the same

for all experimental samples, as indicated by Figure 4.35. As all samples were preheated to the same temperature, tearing comes down to the deformation resistance as shown in this paragraph, and the extrusion ram speed, which will be discussed in the next paragraph.

Effects of Extrusion Ram Speed

Alloys 4A and 4B were extruded at 26 to 30 mm/s, which is higher than any of the other alloys. The tearing observed in these alloys may entirely come down to the difference in extrusion ram speed. The high extrusion speed cause higher strain rate and deformation temperature, which is shown to lead to a higher probability of tearing, as can be seen in Figure 4.36 and Figures 4.38 to 4.45.

Effects of Cooling After Extrusion

Alloys 4A and 4B both exhibited clear signs of tearing in both sections (1) and (2). However, the same signs were not present in the air cooled section (3) of either sample. Similarly in other samples, signs of surface imperfections was observed early in the extruded profile, but became smoother over time. It could be speculated that this pattern arises due to the high extrusion force in the early stage of the press, which decreases over time as steady state extrusion is reached. This pattern can be seen in the extrusion logs, in Appendix F.

5.4 Hardness Tests

In this subsection, the artificial ageing and hardness tests will be discussed. This includes the experimental conditions under which testing was conducted, the effects of chemical composition, homogenization, extrusion speed and cooling after extrusion affects in the alloys. PRO^{3TM} does not return the expected hardness of the alloys, such that no comparison can be made in this subsection.

Experimental Conditions

The extruded samples had a very rough surface, and some of them were crooked. When hardness was measured the first parallel, the samples were flattened and grinded to an even surface. Comparisons in hardness were made between the rough and the even surface. The flat surface had more consistent measurements, but on average, the hardness was measured to be approximately the same. Due to how time demanding it would be to treat the surfaces all 144 samples, hardness was measured on an uneven surface. This is a significant source of uncertainty. Samples were left in room temperature for a varying amount of time between extrusion and artificial ageing, which could have allowed natural ageing to affect the ability to be hardened. Artificially aged samples were also left in room temperature for a varying amount of time before hardness was measured. These factors could explain why there seems to be such a low response to the artificial ageing. Perhaps also the temperature of 180 °C was too low for the ageing period. A salt bath as opposed to hot air oven may have been a better choice for ageing, as the samples would react to the high temperature quicker. The samples were placed on a brick at room temperature before

going into the oven. This brick may have absorbed much of the heat. Some samples may show signs of increasing hardness towards the 12 hour mark, however this may be speculative at best.

Effects of Chemical Composition and Homogenization

The results give no indication of the effects of different levels of chromium or iron, nor any effects of different homogenization treatment. The difference between low or high extrusion speed, if any, is not evident.

Effects of Cooling After Extrusion

Regarding the effects of cooling rate after extrusion, most alloys show that section (3) (air cooled) is significantly softer than the water quenched sections (1) and (2).

5.5 Electrical Conductivity

In this section, the measured electrical conductivity of the alloys will be discussed. This includes the experimental conditions, effect of chemical composition and homogenization on the alloys.

A brief comparison to the PRO^{3TM} predictions of electrical conductivity was made, however, the simulated results were deemed untrustworthy and discarded. This functionality of the software is currently being revamped.

Experimental conditions

The samples were kept at room temperature for several days before measuring the electrical conductivity. The room temperature was 25 °C, which is standard room temperature. The surfaces of the samples were somewhat uneven, which may be a source of uncertainty due to the probe. The samples were believed to have been peak aged (T6), however, the hardness tests were inconclusive, such that it cannot be stated with certainty.

Effects of Homogenization

The electrical conductivity in aluminium is dependent on defects and impurities in the matrix, which increases the electrical resistance. When precipitates are formed, alloying elements in supersaturated solid solution are ”soaked up”, and the proportion of elements in solid solution is lowered. This in turn causes the electrical conductivity to increase. This can be seen in Figure 4.56, where all Hom. B alloys have a higher conductivity than their Hom. A counterpart. From what has been already directly observed in regards to dispersoids, it is believed that a longer homogenization time has lead to more of these alloying elements to be removed from solid solution, and thus, Hom. B exhibit a higher electrical conductivity. This could have been confirmed by measuring electrical conductivity throughout the artificial ageing process, however due to the seemingly unsuccessful hardening process, this was dropped.

Effects of Chromium and Iron

Iron is considered a contaminant in aluminium. As can be seen in Figure 4.56 when comparing samples 1A to 3A and 1B to 3B, the electrical conductivity decreases with increasing iron content. The same conclusion is reached when comparing samples 2 and 4 respectively. When comparing for chromium, it appears that electrical conductivity decreases with increasing chromium levels. This conclusion is drawn from comparing sample 1A to 2A and 1B to 2B, and the same with samples 3 and 4 respectively. Chromium in solid solution could negatively impact the electrical conductivity, as elements in solid solution typically do.

5.6 Further Work

Many of the results from this thesis are uncertain. Poor experimental conditions combined with little experience may have caused unnecessary uncertainties or errors which. Below is a list of the suggested tasks which could help clarify the conclusions reached in this report.

- More precise measurements of the dispersoids in SEM.
- Examining the smallest dispersoids in TEM.
- The effects of homogenization can be explored further.
  Hom. C 585/6 and Hom. D: 555/1.
- Examining the extrusion die tool for imperfections. Replace with a clean die.
- Artificially ageing for longer time. Tensile tests and crush testing.
- Electrical conductivity testing for different ageing times.
- Calibrating PRO^{3TM} in accordance to the results on this thesis and associated work conducted at both Norsk Hydro and SINTEF.

Chapter 6

Conclusion

In this thesis, which builds on a specialization project from the fall of 2018, the 6082 series of aluminium alloys have been investigated with the use of a range of different computational models tied together into a proprietary software known as PRO^{3TM}. Experimental tests were conducted to control the validity of these predictions. The software simulates the through process of extruded aluminium, from casting and homogenization, to extrusion and artificial ageing. The objective of the simulation was to identify alloys with high yield strength which could be extruded at high speed while maintaining a fibrous microstructure and a low probability of tearing.

When the Pareto curve had been constructed with these goals in mind, four alloys were cast in two different parallels. Each parallel was homogenized differently. Hom. A represents homogenization at 585 °C for 1 hour, while Hom. B represents homogenization at 555 °C for 6 hours. Each bolt was extruded in a two-speed program. The front of the extruded profile was water quenched, and the back end of the profile was air cooled. This yielded a profile with three distinct section. The microstructure of the extruded material was examined in optical microscopy, and dispersoids were examined in SEM. The extruded metal was then artificially aged, and tested for hardness during the precipitation process. The electrical conductivity was measured in the samples which had been artificially aged for 5 hours.

A parameter study of the alloys was conducted in PRO^{3TM}, meaning that the experimental alloys were simulated in order to identify thresholds of recrystallization and tearing. These results have been compared to the experimental results.

In regards to the grain structure of the extruded material, the samples exhibited a wide range of structures, including completely fibrous, partly recrystallized, fully recrystallized with small grains and fully recrystallized with large grains. The thesis finds that the air cooled sections of the extruded profile are generally more recrystallized than the water quenched sections. This result is expected, as the quenching stops the recrystallization process. It was found that chromium can help prevent recrystallization, which is justified by the theoretical background as chromium is a dispersoid-forming element. Dispersoids prevent or retard recrystallization through Zener pinning. The thesis also finds that ho-

mogenization B (555 °C/5h) is less recrystallized than homogenization A (585 °C/1h). This was contrary to both expectations and simulations, as additional time during homogenization are expected to decrease the number density of dispersoids through coarsening of particles and dissolution of the smallest dispersoids. It is speculated that chromium dispersoids may nucleate at the interface of β-AlFeSi phases and during long homogenization times, these iron-bearing phases will eventually dissolve or transform, thus increasing the number density of dispersoids and inhibiting recrystallization to a larger extent in Hom. B alloys compared to Hom. A alloys. The effects of iron in this work is not well demonstrated. The expected results is that the iron would promote recrystallization as the iron-bearing phases absorb dispersoid-forming elements such as manganese and chromium. However, the some indication of the opposite effect may be evident, perhaps due to the increased density of nucleation sites for dispersoids, as previously stated.

In regards to dispersoids, the results are clouded with uncertainty, which comes from the difficulty of preparing samples and measuring chromium containing dispersoids. The dispersoids containing chromium have been said to be darker and more difficult to separate from the matrix. Furthermore, a high voltage and a relatively high working distance was used during investigations in SEM, which could have shown sub-surface dispersoids as well as the dispersoids in the surface. This was further substantiated by the measurements done at Hydro Sunndalsøra. For both samples, there was a factor of 2.5 to 3 in difference in number density. Furthermore, the measured dispersoids have a lower detection threshold of 50 nm particles, while Alstruc simulations have no such lower threshold. These measurements must be judged critically.

In regards to tearing, it was only observed in Alloy 4A and 4B for both 26 and 30 mm/s extrusion speed, while smaller indications of tearing was observed in 3A at 26 mm/s extrusion speed. Both alloys 4A and 4B were extruded at higher ram speeds than Alloys 1, 2 and 3. This is an important factor in regards to tearing, as higher extrusion speeds is shown to cause higher deformation temperatures. Furthermore, alloys 3A and 4B has among the highest number densities of dispersoids, and it is reason to believe that these also exhibited the highest deformation temperatures.

In regards to artificial ageing, no unambiguous result was found in regards to the precipitation hardening of the alloy. The reason as to why is not known.

In regards to the electrical conductivity, it was found that Hom. B alloys have a higher electrical conductivity than Hom. A alloys. This is because the precipitates which form and grow during homogenization absorb alloying elements from solid solution, which otherwise would be detrimental to the electrical conductivity of the alloy. Both high iron and high chromium alloys displayed a lower electrical conductivity than their low concentration counterpart. This is believed to be due to the higher concentration of elements in solid solution for high Fe/Cr alloys respectively.

Conclusively, this thesis suggests that the PRO$^{3\text{TM}}$ software has some weak points, especially in regards to the effect of chromium and the interaction with iron. Moreover, the simulations lie outside the metamodel validity range, on which many of the results are based. More and better measurements must be made such that the software can be calibrated accordingly.

Bibliography

[1] Nesse, A., (2018). *Computational Alloy Design of AA6xxx Extrusion*. Specialization project, Department of Materials Science and Engineering, NTNU.

[2] Azo Materials, (2005). *Aluminium Alloys - Aluminium 6082 Properties, Fabrication and Applications*.

[3] Marr, B (2016). *Why Everyone Must Get Ready For The 4th Industrial Revolution*. Forbes.

[4] Hermann, M., Pentek, T., Otto, B. (2016). *Design Principles for Industrie 4.0 Scenarios*, accessed Dec 17 2018.

[5] Wolter, M. I. (2015). *Industrie 4.0 und die Folgen für Arbeitsmarkt und Wirtschaft*. Doku.iab.de (in German), accessed Dec 17 2018.

[6] Illustration by Christoph Roser at AllAboutLean.com

[7] Scott, J. et al. (2018). *Advanced Computation and Data in Materials and Manufacturing: Core Knowledge Gaps and Opportunities*. The Minerals, Metals and Materials Society.

[8] Myrh, O. R., Østhus, R., Søreide, J., Furu, Trond (2016). *A Novel Methodology for Optimization of Properties, Cost and Sustainability of Aluminium Extrusions*. ET-16

[9] Caylar, P. L., Naik, K., Noterdaeme, O., (2016). *Digital in Industry: From buzzword to value creation*. McKinsey & Company.

[10] Jackson, D., (2017). *The Netflix Prize: How a $1 Million Contest Changed Binge-Watching Forever*. Thrillist Entertainment.

[11] Bishop, C. M. (2006), *Pattern Recognition and Machine Learning*. Springer

[12] Brown, E., (2016). *Who Needs the Internet of Things?*.

[13] Lee, J., Bagheri, B., Kao, H. A., (2015). *A cyber-physical systems architecture for industry 4.0-based manufacturing systems*. Manufacturing Letters.

[14] Daugherty, P., Negm, W., Banerjee, P., Alter, A. (2015). *Driving Unconventional Growth through the Industrial Internet of Things*.

[15] Parris, C. J. (2017). *Minds + Machines. Meet A Digital Twin*. GE Digital.

[16] *What is Digital Engineering.* Aurecon (2018).

[17] Baille, S. (2018). *Dropp smarthøyttalere til jul, dette blir de viktigste teknologitrendene i 2019*. E24-Podden, episode 169 (in Norwegian).

[18] Sawe, B. E. (2018) *The Most Abundant Elements In The Earth's Crust.* World Atlas.

[19] Grotheim, K., Kvande, H. (1993). *Introduction to Aluminium Electrolysis*. Aluminium-Verlag, Düsseldorf.

[20] Illustration by FACE, Interational Facade Community. *The Aluminium Unique Life Cycle Story*. https://internationalfacade.com/news/general/aluminium-unique-life-cycle-story/, accessed Dec 17 2018.

[21] Otarawanna, S., Dahle, A.K., (2011). *Fundamentals of Aluminium Metallurgy*.

[22] Mallic, P. K., (2012). *Advanced Materials of Automotive Engineering*.

[23] The Metal Casting. *Wrought Aluminium.*

[24] Davis, J. R., (1999). *Corrosion of Aluminum and Aluminum Alloys*

[25] Reiso, O. (2004). *Extrusion of AlMgSi Alloys*. Materials Forum.

[26] Solberg, J. K., (2013). *Teknologiske metaller og legeringer*. Institutt for materialteknolgi, NTNU.

[27] Avallone, E., Baumeister III, T., Sadegh, A., (1999). *Mark's Standard Handbook for Mechanical Engineers.* 8th Ed., McGraw Hill.

[28] Norsk Standard (1994). *Aluminium and aluminium alloys. Chemical composition and form of wrought products. Part 3: Chemical composition.*

[29] Reiso, O., (2014). *Forelesning i ekstrudering*. Norsk Hydro Sunndalsøra.

[30] Rinderer, B. (2011). *The Metallurgy of Homogenisation*. Materials Science Forum.

[31] Rosefort, M., Matthies, C., Buck, H., Koch, H. *Determination of α- and β-AlFeSi Phases in Wrounght Aluminium Alloys*. TRIMET

[32] Minoda, T., Hayakawa, H., Matsuda, S., Yoshida, H., (2000). *Extrusion Technology Conference Proceedings*

[33] Erik, O., Jones, F., Horton, H., Ryffel, H. (2000). *Machiner's Handbook*, (26th ed.), New York: Industrial Press.

[34] Furu, T., Marthinsen, K. (2018). Private communications.

[35] Zajac, S., Hutchinson, B., Johansson, A., Gullmann, L.O., (1994). *Microstructure Control and Extrudability of Al-Mg-Si Allows Microalloyed with Manganese*. Materials Science and Technology.

[36] Lodgaard, L., Ryum, N., (2000). *Precipitation of Dispersoids Containing Mn and/or Cr in Al-Mg-Si alloys*. Materials Science and Engineering.

[37] Hichem, F., Rebai, G., (2014). *Study of dispersoid particles in two Al-Mg-Si aluminium alloys and their effects on recrystallization*. Applied Physics A. Materials Science and Processing.

[38] Terahsima, S., Bhadeshia, H. K., (). *Grain Growth: Zener Pinning of Grain Boundaries by Oxide Particles*. University of Cambridge.

[39] Sarafoglou, P., Haidemenopoulos, G., (2014). *Phase Fraction Mapping in the as-cast microstructure of extrudable 6xxx aluminum alloys*.

[40] Sweet, E. D., Caraher, S.K., Danilova, N.V., Zhang, X., (2001). *Effects of Extrusion Parameters on Coarse Grain Surface Layer in 6xxx Series Extrusions*

[41] Saha, P. K., (2000). *Aluminium Extrusion Technology*. ASM International.

[42] Bru, M., (2014). *The Effect of n and Homogenization Procedure on Mechanical Properties and Grain Structure in Extruded AA6082*

[43] Polmear, I. J., (2006). *Light Alloys: From Traditional Alloys to Nanocrystals*. Elsevier.

[44] Grong, Ø., (2012). *Recent Advances in Solid-State Joining of Aluminium*. Welding Journal.

[45] Lohne, O., Dons, A. L., (1983). *Scan. J. Metallurgy*. Vol. 12, p. 34.

[46] Möller, H, (2011). *Optimisation of the heat treatment cycles of CSIR semi-solid metal processed Al-7Si-Mg alloys A356/7*.

[47] Nam, S. W., Lee, D. H., (2000). *The effect of Mn on the mechanical behavior of Al alloys*. Metals and Materials.

[48] Ashby, M. F., (1996). *Modelling of materials problems*. Department of Engineering, University of Cambridge.

[49] Miettinen, K. (1999). *Nonlinear Multiobjective Optimization*. Springer.

[50] *modeFRONTIER^{TM} documentation*. ESTECO SpA.

[51] Engler, O., Marthinsen, K., (2010). *Modelling softening and recrystallization textures*.

[52] Myhr, O. R., Grong, Ø., Schäfer, C., (2015). *An Extended Age-Hardening Model for Al-Mg-Si Alloys Incorporating the Room-Temperature Storage and Cold Deformation Process Stages*. Volume 46A, Metallurgical and Materials Transactions A

[53] Myhr, O. R., Furu, T., Emmerhoff, O. J., Skauvik, I., Engler, O., (2012) *Through Process Modelling of Grain Structure Evolution in 6xxx Series Aluminium Extrusions*.

[54] Dons, A. L., (2001). *The Alstruc homogenization model for industrial aluminum alloys*. Journal of Light Metals, Vol 1, issue 2.

[55] Altair HyperWorks. *HyperXtrude® documentation*.

[56] Myhr, O. R., Grong, Ø., Pedersen, K.O., (2010). *A Combined Precipitation, Yield Strength, and Work Hardening Model for Al-Mg-Si Alloys*. Metallurgical and Materials Transactions A

[57] Vatne, H. E., Furu, T., Orsund, R., Nes, E., (1996). *Modelling recrystallization after hot deformation of aluminium*. Acta Materialia, 44.

[58] Furu, T., Østhus, R., Telioui, N., Aagård, R., Bru, M., Myhr, O. R., (2016). *Modeling the Effect of Mn on Extrudability, Mechanical Properties and Grain Structure of AA6082 Alloys*. ET-16

[59] Østhus, R., (2018). Private communications.

[60] IBM. *IBM Watson Health*

[61] Ånes, H. W., (2019). *Particle Size Distribution from BSE Image*.

Appendix

Appendix A

PRO^{3TM} Microstructure

All samples have been modelled using the PRO^{3TM} software to predict properties. In Table A.1, all results have been tabulated. Each sample is divided into two variations, 1 and 2, which refer to low and high speed respectively with water quenching, identical to the description given in Table 4.2.

Table A.1: Computed recrystallization percentages and mean grain size [μm] from the PRO^{3TM} software.

			Position		
Sample			Center	Intermediate	Surface
1A	(1)	Rex	38%	33%	100%
		Drex	625	629	366
	(2)	Rex	0%	0%	12%
		Drex	-	-	18300
1B	(1)	Rex	100%	100%	100%
		Drex	159	137	94.7
	(2)	Rex	100%	100%	100%
		Drex	187	145	121
2A	(1)	Rex	0%	0%	21%
		Drex	-	-	2950
	(2)	Rex	liq.	liq.	liq.
		Drex	-	-	-
2B	(1)	Rex	100%	100%	100%
		Drex	170	172	109
	(2)	Rex	100%	100%	100%
		Drex	294	252	154
3A	(1)	Rex	100%	100%	100%
		Drex	350	231	183
	(2)	Rex	62%	92%	100%
		Drex	928	796	365
3B	(1)	Rex	100%	100%	100%
		Drex	140	123	88.0
	(2)	Rex	100%	100%	100%
		Drex	154	133	92.0
4A	(1)	Rex	0%	2%	50%
		Drex	-	-	6275
	(2)	Rex	N/A	N/A	N/A
		Drex	N/A	N/A	N/A
4B	(1)	Rex	100%	100%	100%
		Drex	187	147	120
	(2)	Rex	N/A	N/A	N/A
		Drex	N/A	N/A	N/A

Appendix B

Dispersoids

B.1 Particle Size Distribution Plots

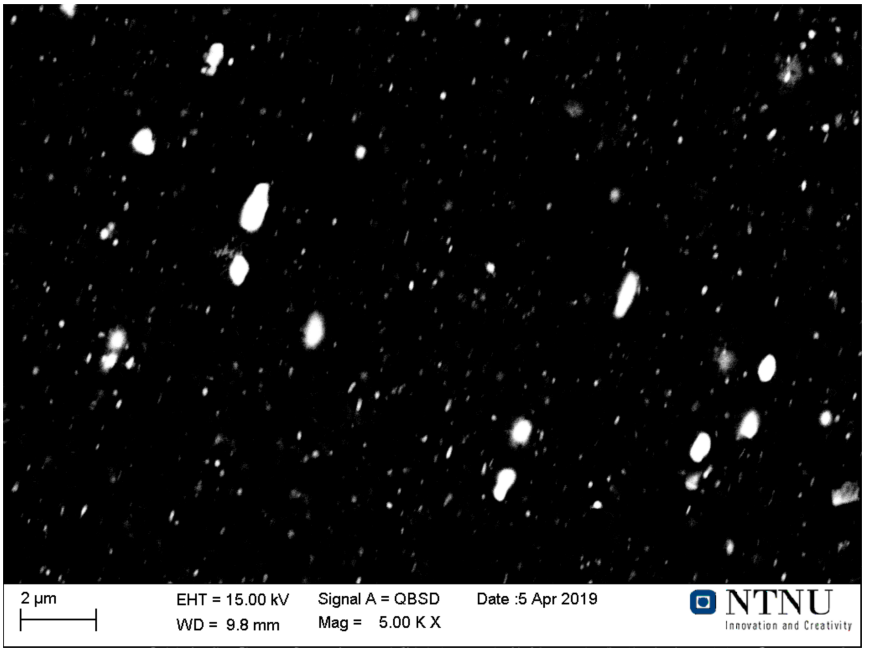

Figure B.1: Post-processed image of dispersoids from SEM.

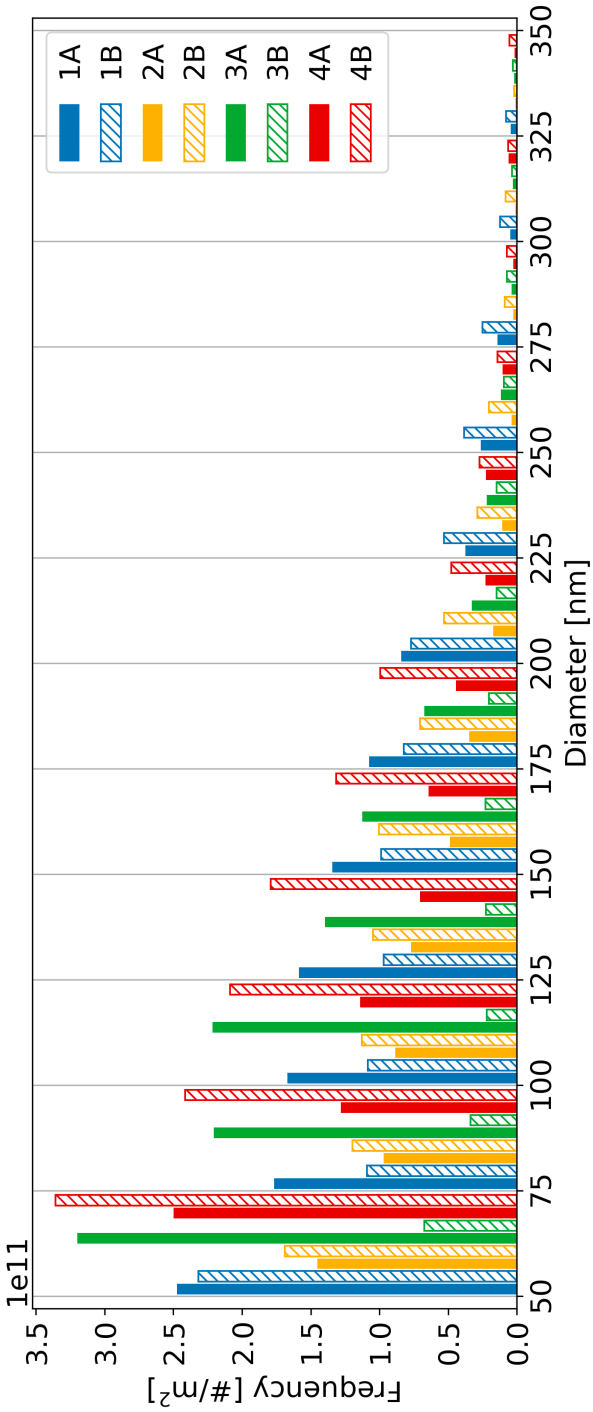

Figure B.2: Size distribution of dispersoids all samples weighted by frequency.

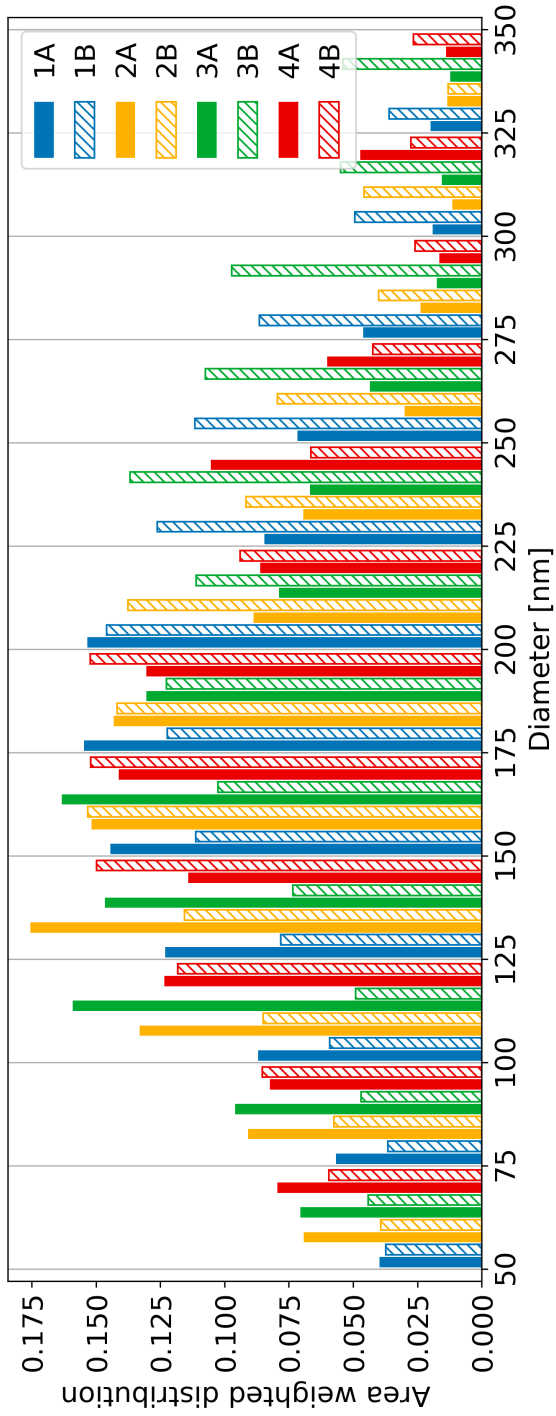

Figure B.3: Size distribution of dispersoids all samples weighted by area.

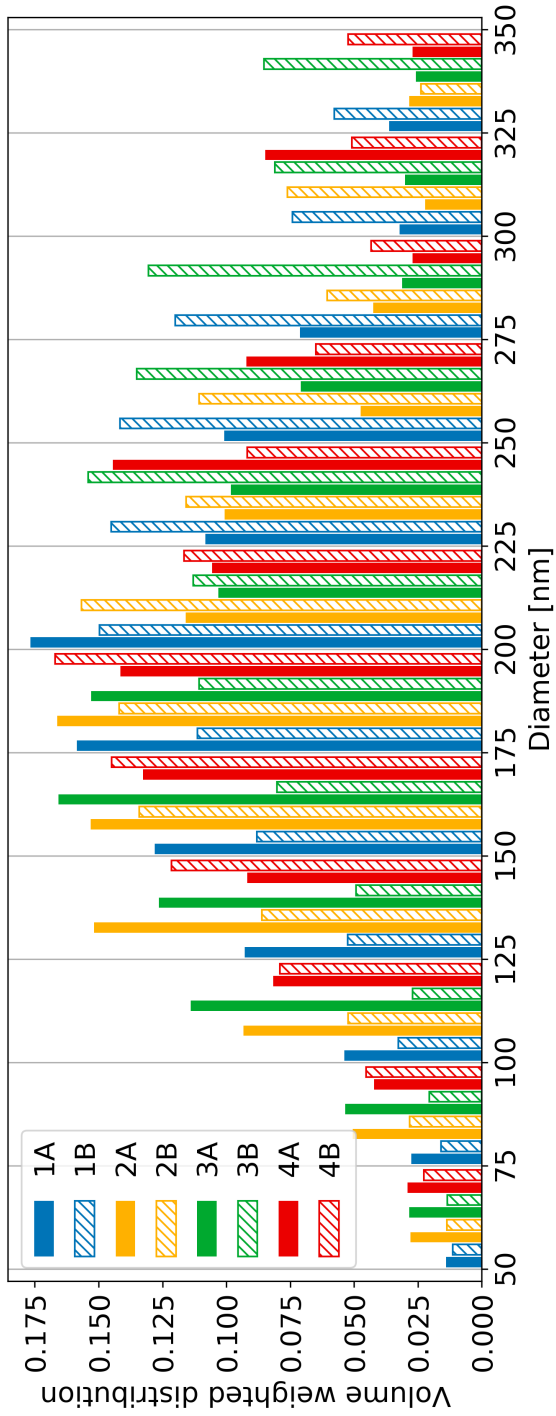

Figure B.4: Size distribution of dispersoids all samples weighted by volume.

Alloy 1

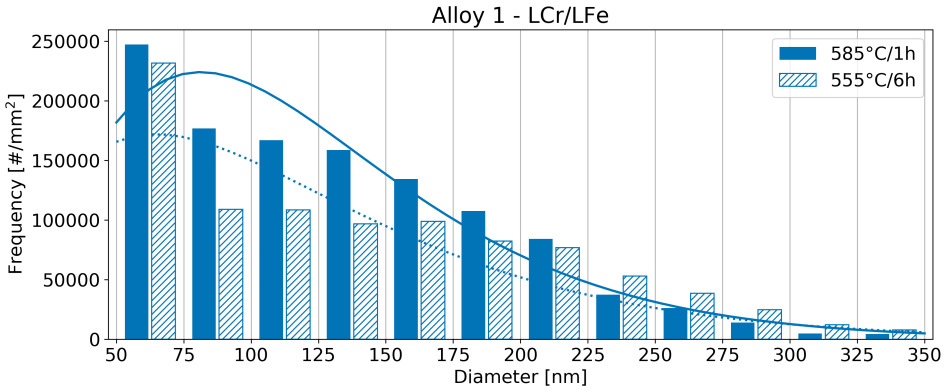

Figure B.5: Particle size distribution (absolute) and curve fitting for alloy 1.

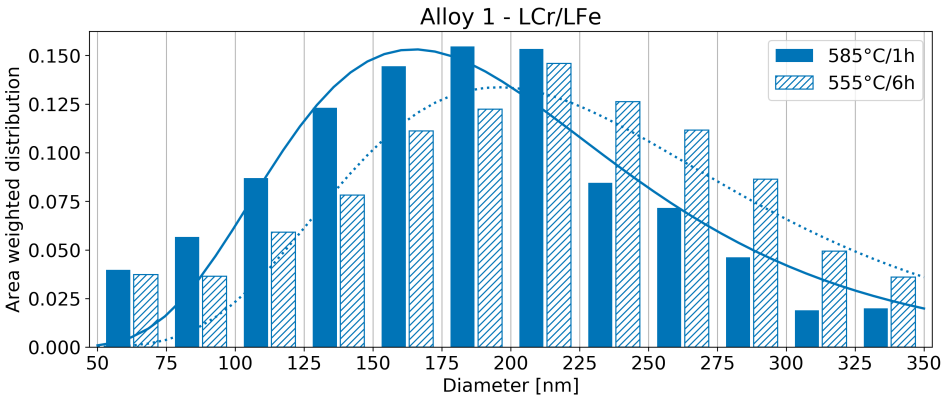

Figure B.6: Particle size distribution (normalized) and curve fitting for alloy 1, weighted by area.

Alloy 2

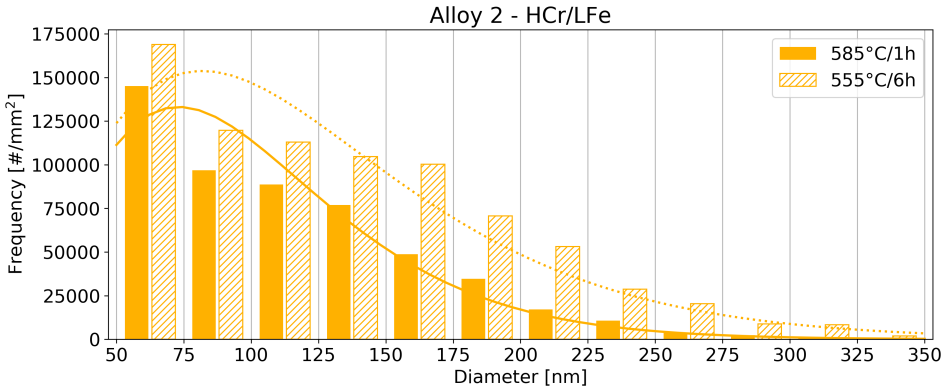

Figure B.7: Particle size distribution (absolute) and curve fitting for alloy 2.

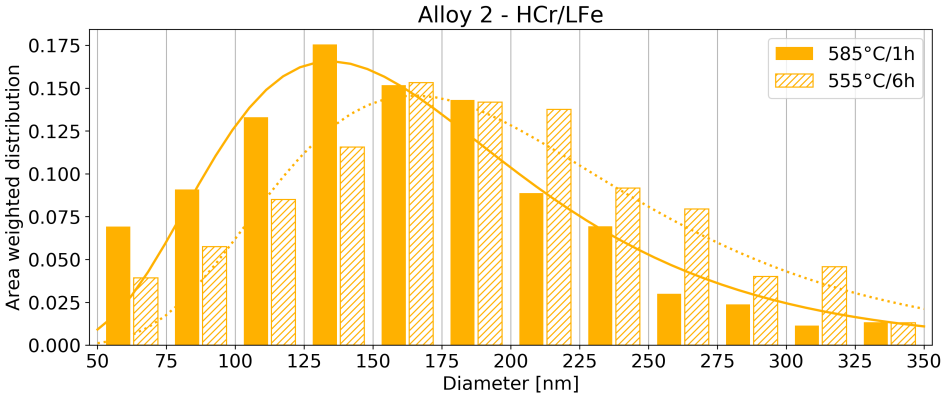

Figure B.8: Particle size distribution (normalized) and curve fitting for alloy 2, weighted by area.

Alloy 3

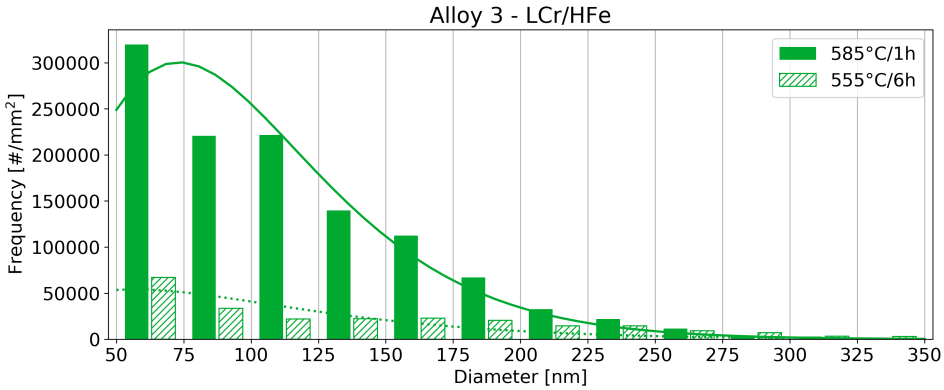

Figure B.9: Particle size distribution (absolute) and curve fitting for alloy 3.

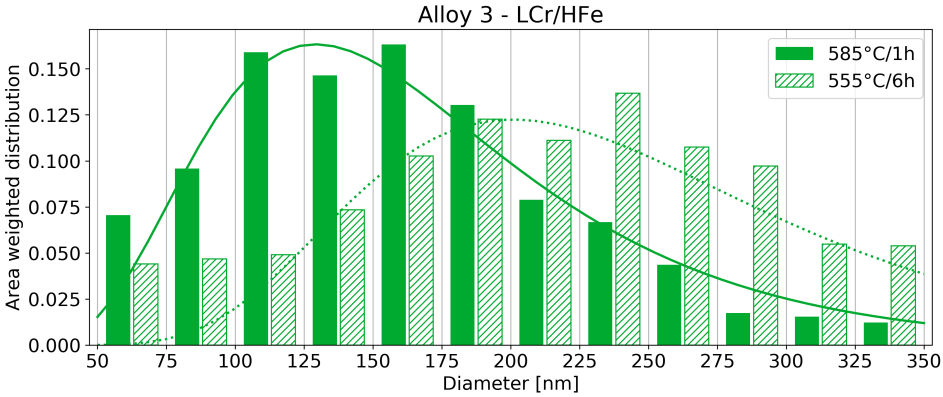

Figure B.10: Particle size distribution (normalized) and curve fitting for alloy 3, weighted by area.

Alloy 4

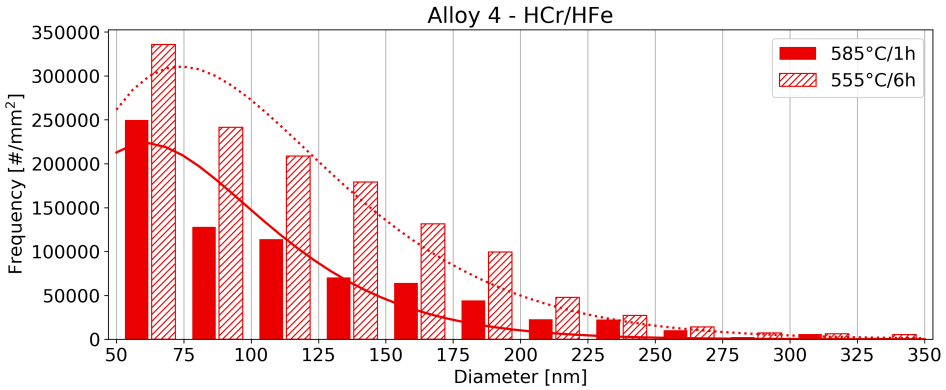

Figure B.11: Particle size distribution (absolute) and curve fitting for alloy 4.

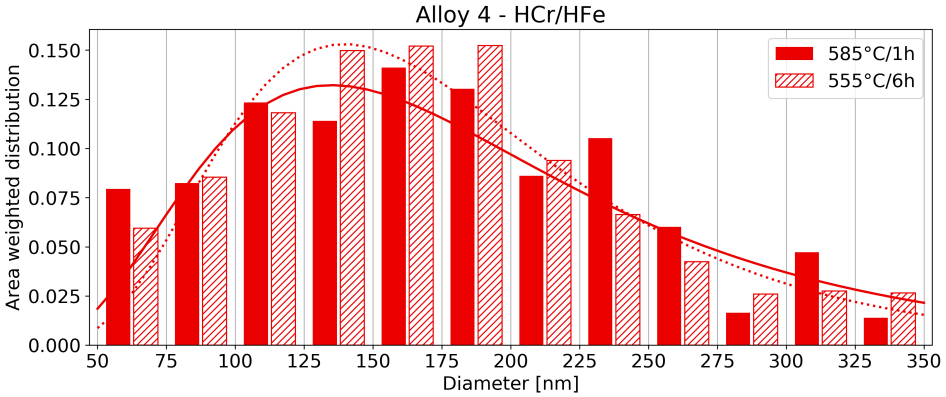

Figure B.12: Particle size distribution (normalized) and curve fitting for alloy 4, weighted by area.

B.2 Dispersoid Analysis

This software was developed by PhD candidate Håkon Wiik Ånes at NTNU, Department of Materials Science and Technology, Norway. The example image was acquired by Eirik Bugten Hamnes at NTNU. The full script is found on [GitHub]

Import and inspect data

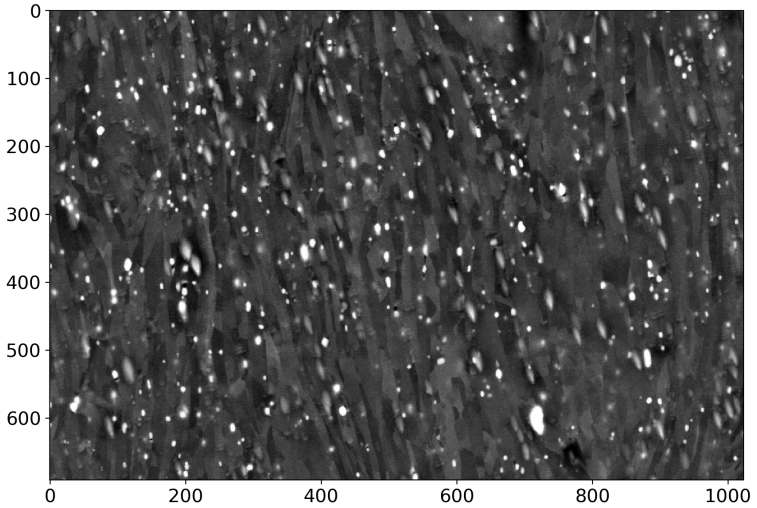

Figure B.13: Raw BSE image.

Convert image to grayscale.

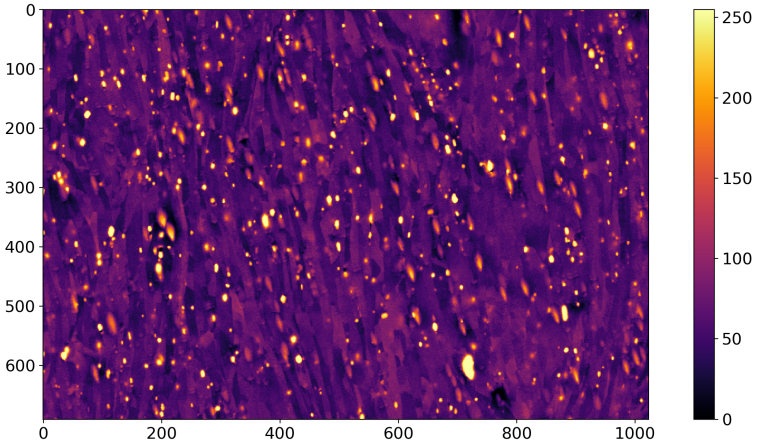

Figure B.14: Converted to grayscale and 8 bit.

2. Detect particles based upon image intensity using region-based segmentation
Create elevation map with particle edges highlighted.

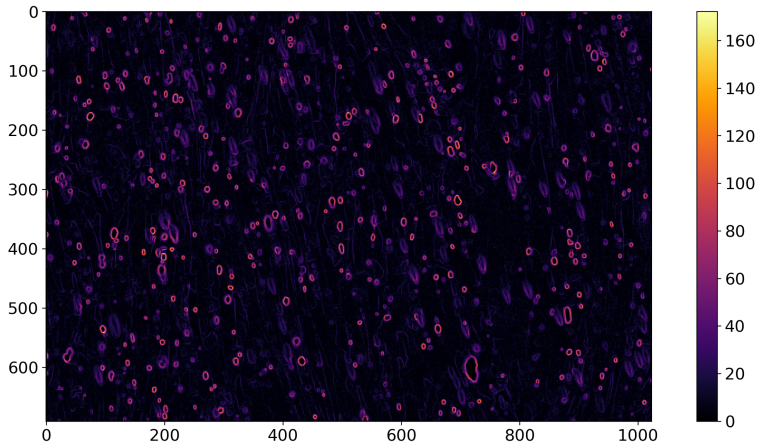

Figure B.15: Elevation map of BSE image.

Detecting particles from the background and creating markers for each particle.

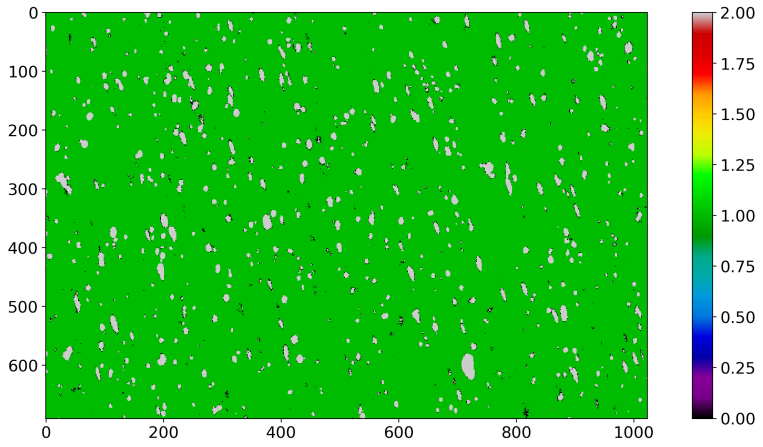

Figure B.16: Detect particles from background.

Create binary image with watershed transformation by flooding the elevation map starting from the markers.

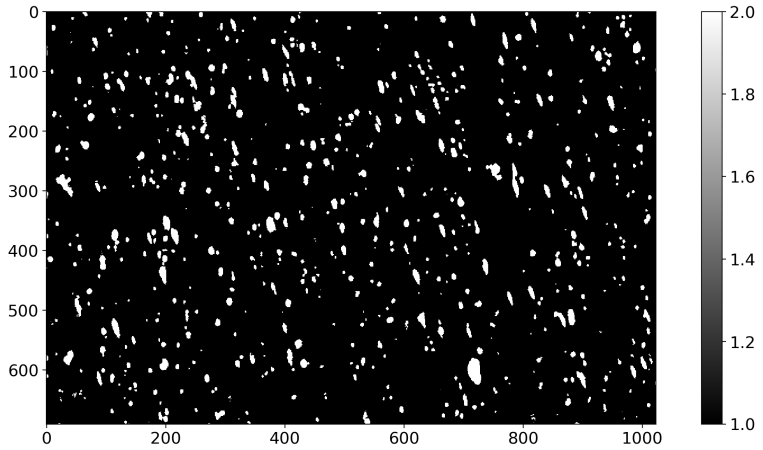

Figure B.17: Binary BSE image.

3. Segment labeled image into particles and analyse particle properties
Segment particles from binary image. Cross reference with original BSE image.

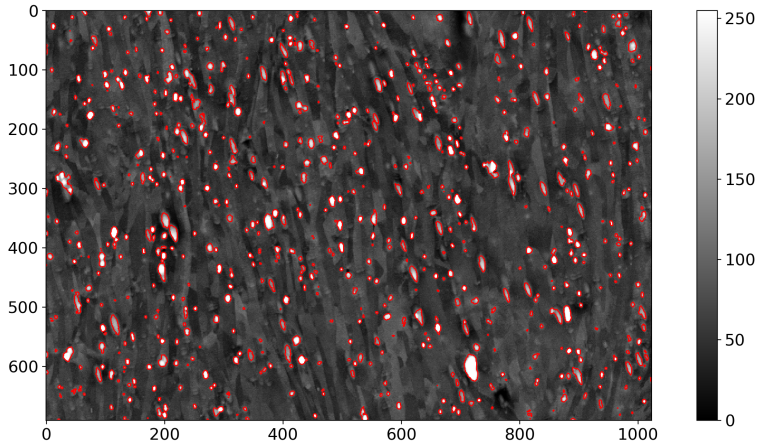

Figure B.18: Import segmented particles into BSE image.

Analyze particle properties. Remove too small or too large particles. Remove wrongly segmented particles based on eccentricity and roundness.

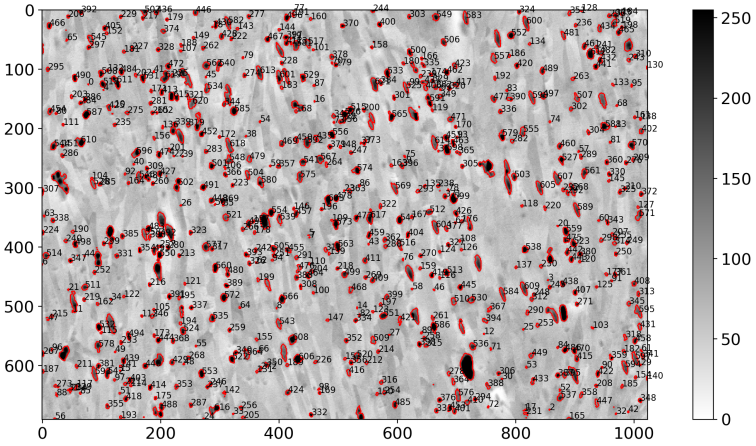

Figure B.19: Grayscale with segmented particles.

Plot particle size distribution, calculate the frequency and the number density, area covered by dispersoids and export data to file.

B.3 Measurements from Hydro

Independent measurements of the dispersoid density was performed by John Rasmus Leinum at Research and Technology Development department at Hydro Sunndalsøra. The comparisons between his results and the thesis results can be seen from Figures B.20 and B.21 respectively. Below are his comments on the experimental conditions.

> ”In general, there were small dispersoids in the samples, which made it difficult to set the threshold between subsurface dispersoids and the dispersoids in the surface. If the dispersoids contain chromium, they have a lower backscatter rate, and will appear darker. They are more difficult to separate from the matrix.”

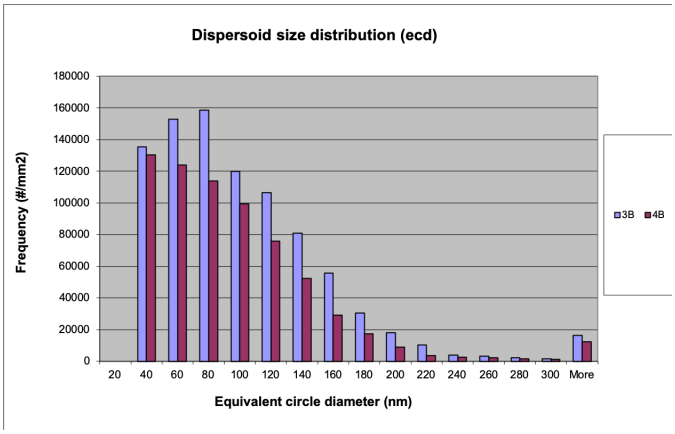

Figure B.20: Particle size distribution of sample 3B and 4B measured in the lab at Hydro Sunndalsøra.

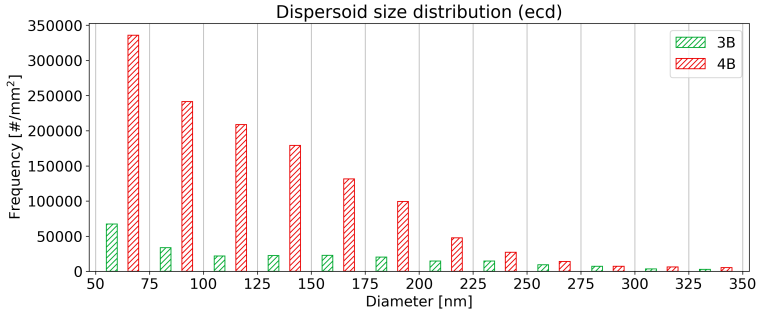

Figure B.21: Particle size distribution of sample 3B and 4B as a result of this thesis.

Appendix C

Python Scripts

The Python scripts used in this thesis can be found in a Google Drive folder. The Drive can be accessed by using the QR-code below, or by clicking the link. The scripts included are HyperXtrude® pre- and post-processing, modeFRONTIER™ post processor, and the dispersoid analysis script. The scripts used for plotting is also in this folder.

[Google Drive folder]

Appendix D

modeFRONTIER^{TM} Workflow

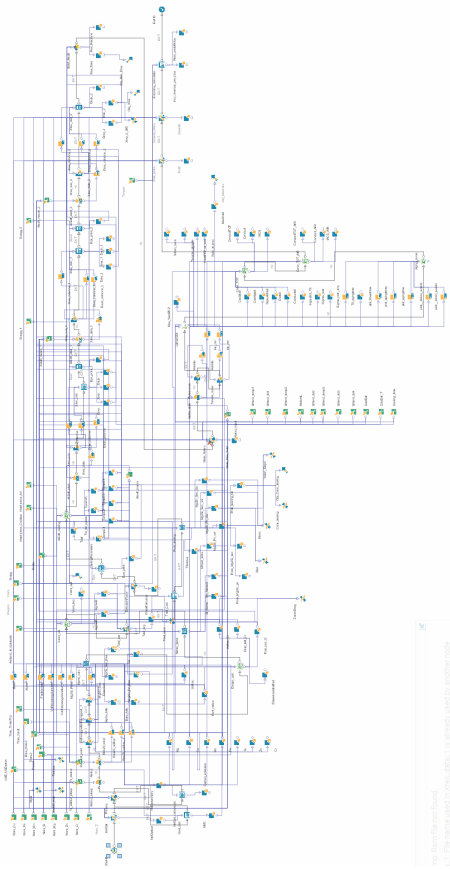

Figure D.1: The complete PRO^{3TM} workflow.

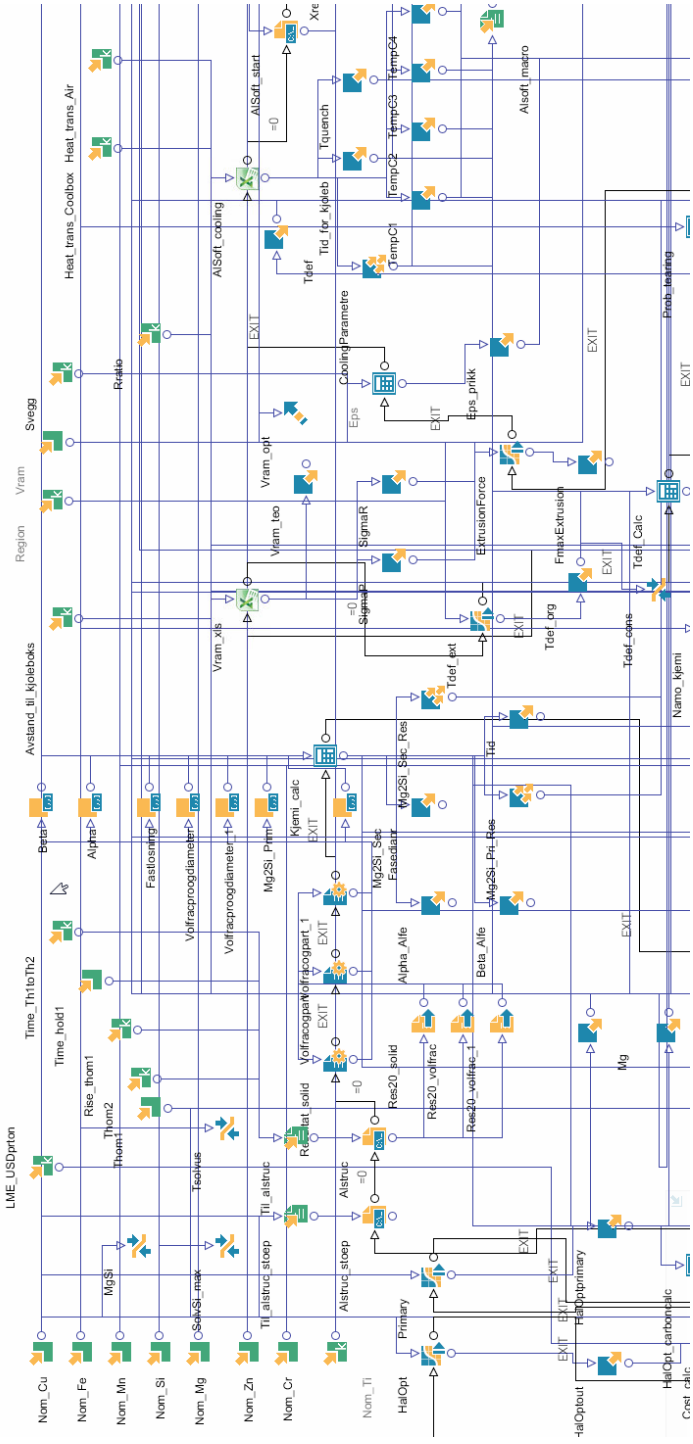

Figure D.2: The initial segment of the workflow, including all input parameters.

Appendix E

Design of Experiment

Table E.1: Boundary conditions for the different variables in the modelling. σ_P and σ_R were only considered inputs in the metamodel, not modeFRONTIER™.

Chemistry			**Homogenization**			**Extrusion**		
[wt%]	Min	Max		Min	Max		Min	Max
Si	0.7	1.3	Temp [°C]	480	580	Vram [mm/s]	4	16
Fe	0.0	0.5	Time [hrs]	1	10	σ_P [MPa]	0.8	2.6
Cu	0.0	0.1				σ_R [MPa]	16.6	17.9
Mn	0.4	1.0						
Mg	0.6	1.2						
Cr	0.0	0.25						
Zn	0	0.2						

Table E.2: DOE for the metamodel in HyperXtrude®.

ID	Red_forhold	σ_P	σ_R	Taper	T_{billet}	ν_{ram}
0	23,90	2,00	17,03	26,00	460,00	8,00
1	23,90	1,40	17,03	26,00	440,00	20,00
2	23,90	2,00	17,47	26,00	500,00	16,00
3	23,90	0,80	17,47	26,00	460,00	4,00
4	23,90	2,60	16,60	26,00	500,00	16,00
5	23,90	2,60	17,03	26,00	540,00	16,00
6	23,90	1,40	17,90	26,00	540,00	20,00
7	23,90	2,00	16,60	26,00	520,00	8,00
8	23,90	2,60	17,90	26,00	500,00	4,00
9	23,90	1,40	17,03	26,00	440,00	12,00
10	23,90	2,00	17,90	26,00	540,00	8,00
11	23,90	0,80	17,03	26,00	500,00	12,00
12	23,90	1,40	17,47	26,00	460,00	20,00
13	23,90	0,80	16,60	26,00	520,00	8,00
14	23,90	1,40	17,90	26,00	540,00	16,00
15	23,90	1,40	17,90	26,00	440,00	8,00
16	23,90	2,00	17,47	26,00	520,00	12,00
17	23,90	2,60	17,47	26,00	440,00	12,00
18	23,90	0,80	17,47	26,00	500,00	4,00
19	23,90	2,60	16,60	26,00	520,00	12,00
20	23,90	0,80	16,60	26,00	540,00	20,00
21	23,90	1,40	17,90	26,00	440,00	20,00
22	23,90	1,40	16,60	26,00	520,00	12,00
23	23,90	2,60	17,03	26,00	460,00	8,00
24	23,90	0,80	17,03	26,00	440,00	20,00
25	23,90	2,00	17,90	26,00	520,00	8,00
26	23,90	2,00	16,60	26,00	460,00	16,00
27	23,90	2,60	17,90	26,00	500,00	16,00
28	23,90	0,80	17,03	26,00	540,00	4,00
29	23,90	0,80	17,47	26,00	540,00	20,00
30	23,90	2,00	16,60	26,00	460,00	12,00

Appendix F

Extrusion Logs

Sample 1A

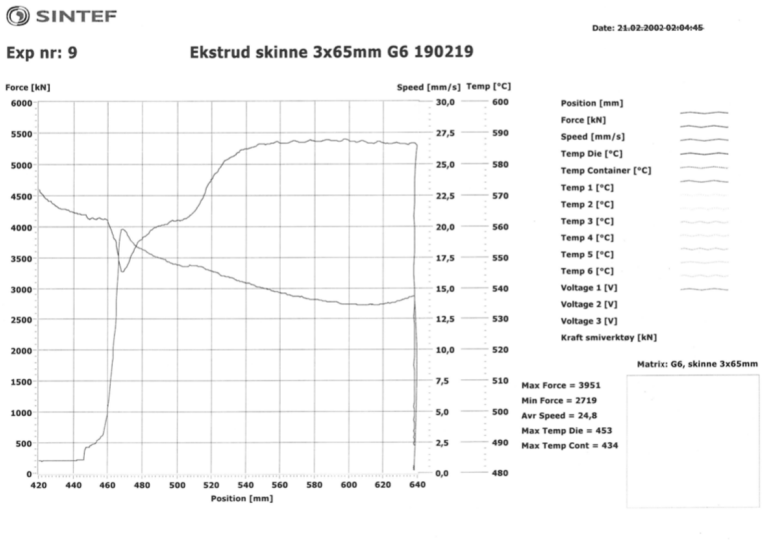

Figure F.1: Extrusion log for sample 1A.

Sample 1B

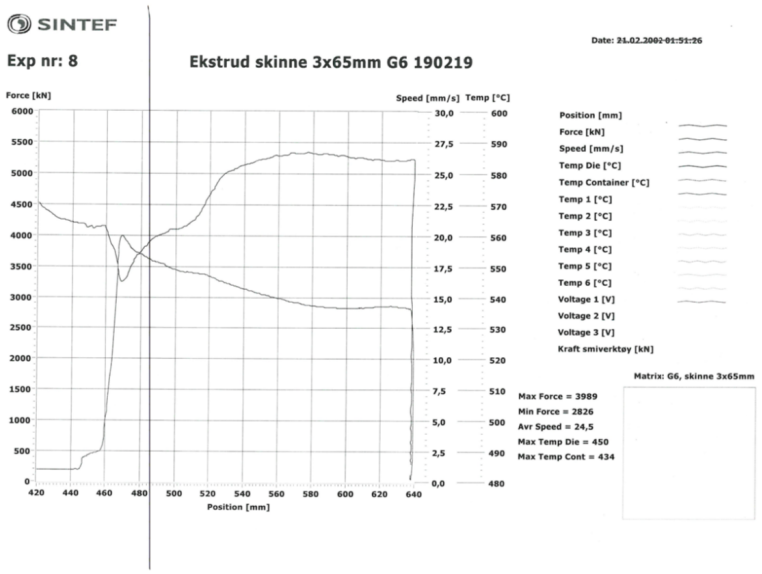

Figure F.2: Extrusion log for sample 1B.

Sample 2A

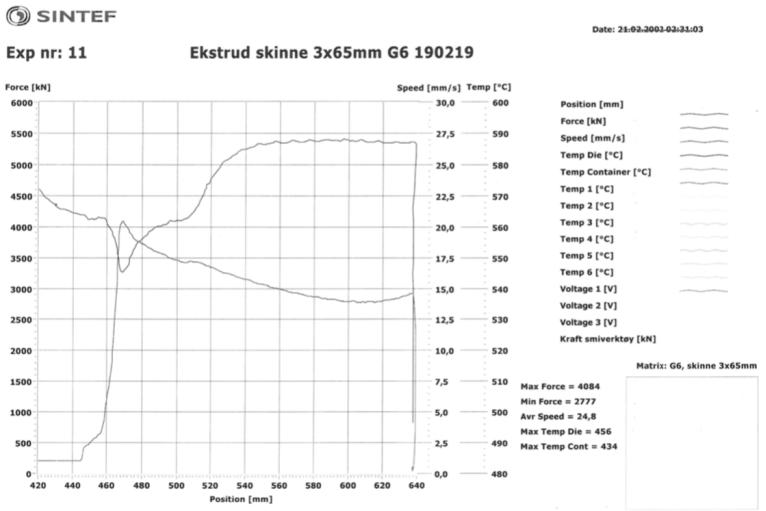

Figure F.3: Extrusion log for sample 2A.

Sample 2B

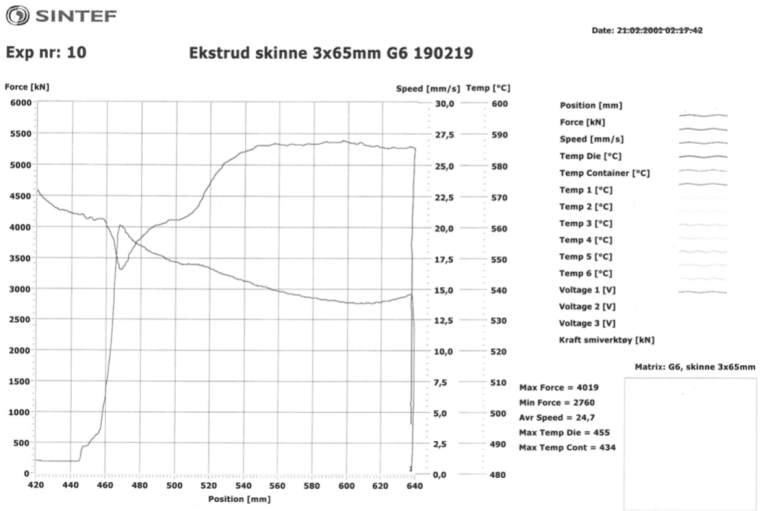

Figure F.4: Extrusion log for sample 2B.

Sample 3A

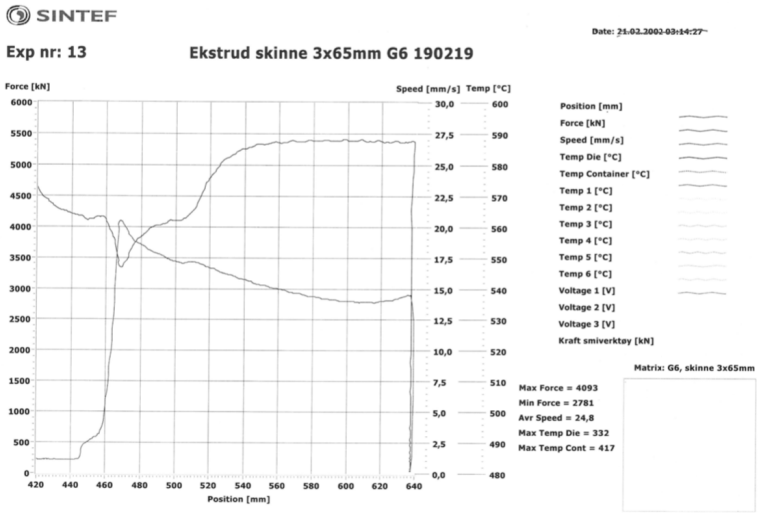

Figure F.5: Extrusion log for sample 3A.

Sample 3B

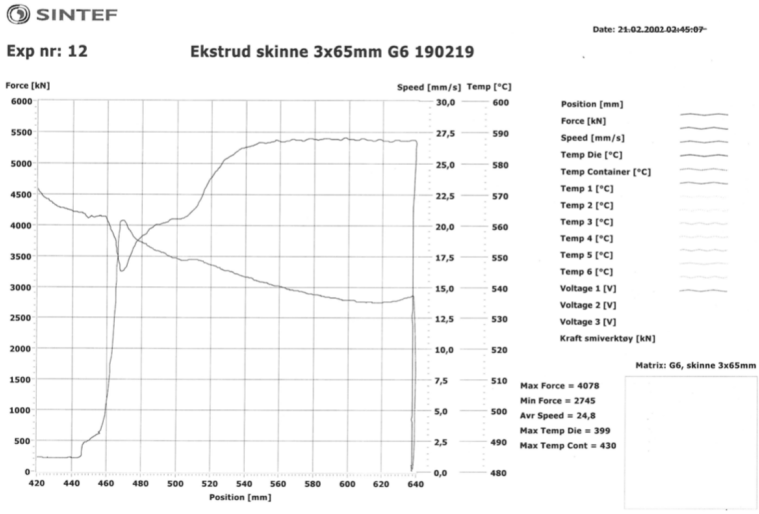

Figure F.6: Extrusion log for sample 3B.

Sample 4A

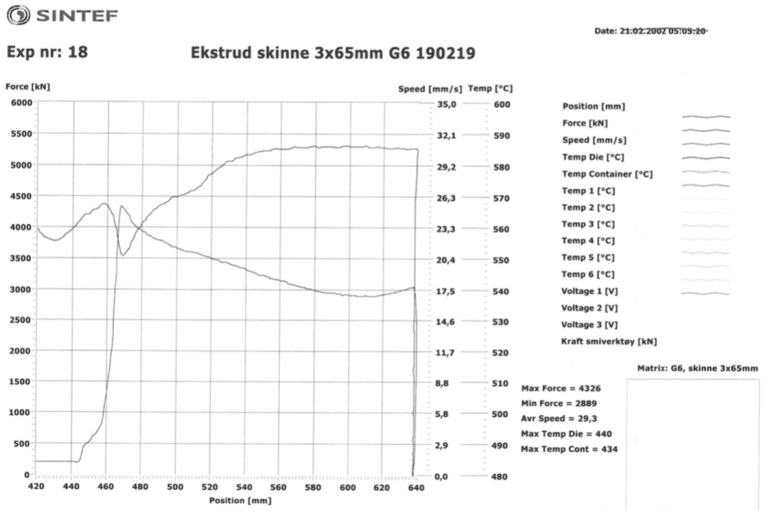

Figure F.7: Extrusion log for sample 4A.

Sample 4B

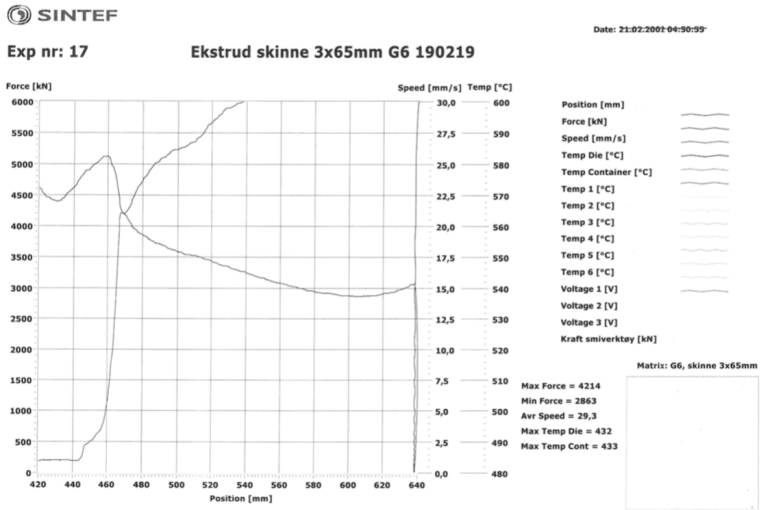

Figure F.8: Extrusion log for sample 4B.